

OPTIMIZATION OF POLYMER-BASED NANOCOMPOSITES FOR HIGH
ENERGY DENSITY APPLICATIONS

A Dissertation

by

AMIRA BARHOUMI EP MEDDED

Submitted to the Office of Graduate Studies of
Texas A&M University
in partial fulfillment of the requirements for the degree of
DOCTOR OF PHILOSOPHY

May 2012

Major Subject: Aerospace Engineering

Optimization of Polymer-based Nanocomposites for High Energy Density Applications

Copyright 2012 Amira Barhoumi Ep Meddeb

OPTIMIZATION OF POLYMER-BASED NANOCOMPOSITES FOR HIGH
ENERGY DENSITY APPLICATIONS

A Dissertation

by

AMIRA BARHOUMI EP MEDDEB

Submitted to the Office of Graduate Studies of
Texas A&M University
in partial fulfillment of the requirements for the degree of

DOCTOR OF PHILOSOPHY

Approved by:

Chair of Committee,	Zoubeida Ounaies
Committee Members,	Gregory Huff
	Dimitris C. Lagoudas
	Choongho Yu
Head of Department,	Dimitris C. Lagoudas

May 2012

Major Subject: Aerospace Engineering

ABSTRACT

Optimization of Polymer-based Nanocomposites for High Energy Density
Applications. (May 2012)

Amira Barhoumi Ep Meddeb, B.E., Tunisia Polytechnic School;

M.S., Tunisia Polytechnic School

Chair of Advisory Committee: Dr. Zoubeida Ounaies

Monolithic materials are not meeting the increasing demand for flexible, lightweight and compact high energy density dielectrics. This limitation in performance is due to the trade-off between dielectric constant and dielectric breakdown. Insulating polymers are of interest owing to their high inherent electrical resistance, low dielectric loss, flexibility, light weight, and low cost; however, capacitors produced with dielectric polymers are limited to an energy density of $\sim 1-2$ J/cc. Polymer nanocomposites, i.e., high dielectric particles embedded into a high dielectric breakdown polymer, are promising candidates to overcome the limitations of monolithic materials for energy storage applications. The main objective of this dissertation is to simultaneously increase the dielectric permittivity and dielectric breakdown without increasing the loss, resulting in a significant enhancement in the energy density over the unmodified polymer. The key is maintaining a low volume content to ensure a high inter-particle distance, effectively minimizing the effect of local field on the composite's dielectric breakdown. The first step is studying the particle size and aspect ratio effects on the dielectric

properties to ensure a judicious choice in order to obtain the highest enhancement. The best results, as a combination of dielectric constant, loss and dielectric breakdown, were with the particles with the highest aspect ratio. Further improvement in the dielectric behavior is observed when the nanoparticles surface is chemically tailored to tune transport properties. The particles treatment leads to better dispersion, planar distribution and stronger interaction with the polymer matrix. The planar distribution of the high aspect ratio particles is essential to limit the enhancement of local fields, where minimum local fields result in higher dielectric breakdown in the composite. The most significant improvement in the dielectric properties is achieved with chemically-treated nano TiO₂ with an aspect ratio of 14 at a low 4.6vol% loading, where the energy density increased by 500% compared to pure PVDF. At this loading, simultaneous enhancement in the dielectric constant and dielectric breakdown occurs while the dielectric loss remains in the same range as that of the pristine polymer.

DEDICATION

To the memory of my sister Hana Barhoumi.

ACKNOWLEDGEMENTS

I would like to thank my advisor Dr. Zoubeida Ounaies for her assistance and guidance throughout my research. And I would like to thank the Electroactive Materials Characterization Lab members for their help whenever needed. My thanks also go to the staff of the Center for Dielectric Studies for their assistance and nanoComposix for providing silver nanoparticles.

I am very grateful to my husband, my parents, my brothers and sisters for their unconditional support.

This work is funded by NSF-CMMI 1136510 and NSF-CMMI 0708096.

NOMENCLATURE

PVDF	Polyvinylidene fluoride
DMAc	N,N-Dimethylacetamide
DMF	N,N-Dimethylformamide
NS	Nano sphere
MS	Micro sphere
NR	Nano rod
NW	Nano wire
APS	3-aminopropyltriethoxysilane
AC	Alternating current
DC	Direct current
C	Capacitance
c	Particles volume fraction
D	Electrical displacement
E	Electric field
E_A	Activation energy
E_b	Dielectric breakdown
f	Frequency
k	Boltzman constant
N_j	Ellipsoidal particles depolarization factors

R	Particles radius
U	Electrical energy density
ϵ'	Dielectric constant
ϵ_0	Dielectric constant of vacuum
ϵ_1	Polymer matrix dielectric constant
ϵ_2	Particles dielectric constant
ϵ''	Dielectric loss
Tan(δ)	Loss tangent
α	Non-polar PVDF phase
β	Polar PVDF phase
	Shape factor when used for breakdown measurements
γ	Polar PVDF phase
ρ	Electrical resistivity

TABLE OF CONTENTS

	Page
ABSTRACT	iii
DEDICATION	v
ACKNOWLEDGEMENTS	vi
NOMENCLATURE.....	vii
TABLE OF CONTENTS	ix
LIST OF FIGURES.....	xi
LIST OF TABLES	xv
CHAPTER	
I INTRODUCTION AND PROBLEM STATEMENT	1
1. Motivation	1
2. Background and literature review	4
3. Problem statement	26
4. Contributions of this work.....	28
II EXPERIMENTAL METHODOLOGIES	30
1. Materials.....	30
2. Composites synthesis	31
3. Scanning electron microscopy	34
4. Transmission electron microscopy.....	35
5. Fourier transform infrared (FTIR) spectroscopy.....	35
6. X-Ray photoelectron spectroscopy (XPS)	37
7. Differential scanning calorimetry (DSC)	37
8. Polarized Raman spectroscopy.....	39
9. Tensile testing	41
10. Electrical characterization	42

CHAPTER	Page	
III	SIZE AND ASPECT RATIO EFFECTS ON DIELECTRIC PROPERTIES	50
	1. Composites morphology characterization	50
	2. Low-field dielectric properties	53
	3. High-field dielectric properties	58
IV	PARTICLES CONTENT, FUNCTIONALIZATION AND ORIENTATION EFFECTS ON DIELECTRIC PROPERTIES	63
	1. Particles and composites characterization	63
	2. Mechanical properties	70
	3. Low-field dielectric properties	73
	4. High-field dielectric properties	78
	5. Internal charges behavior	83
	6. Breakdown mechanisms	87
V	THREE-PHASE COMPOSITE STUDY	90
	1. Dispersion study	90
	2. Composites phase using FTIR	92
	3. Degree of crystallinity properties using DSC	93
	4. Electrical properties study	94
VI	CONCLUSIONS AND SUGGESTIONS FOR FUTURE WORK	103
	REFERENCES	108
	APPENDIX A	120
	APPENDIX B	122
	VITA	126

LIST OF FIGURES

	Page
Figure I-1. Current-voltage diagram of a dielectric with loss [40].....	5
Figure I-2. Frequency dependence of the dielectric constant.....	8
Figure I-3. Schematic representation of the relationship between the breakdown field E_b , the time to breakdown t , and the sample thickness d [44].....	11
Figure I-4. Dielectric breakdown vs dielectric constant, coefficient is 0.81 [1].....	13
Figure I-5. Functionalization effect on the dielectric breakdown of BaTiO ₃ -PVDF composites [7]	15
Figure I-6. Physical property continuity between the particles and the polymer matrix.....	16
Figure I-7. Schematic of size effect on interfacial volume.....	17
Figure I-8. Interphase volume percent in a 1vol% composite, where the interphase thickness is assumed to be 5nm.....	18
Figure I-9. Multi-core model for nanoparticle-polymer interfaces [58]	19
Figure I-10. Dielectric constant for TiO ₂ -epoxy composites with nanoparticles (50nm) compared to microparticles (0.5 μ m) [15].....	20
Figure I-11. Dielectric constant for TiO ₂ -epoxy composites with nanoparticles (23nm) compared to microparticles (0.5 μ m) [60].....	20
Figure I-12. Normalized calculated effective permittivity $((\epsilon_{eff} - \epsilon_1)/(\epsilon_2 - \epsilon_1))$ for polypropylene composite dielectrics with TiO ₂ spherical (solid line) and ellipsoidal particles (dashed line) [22].....	22
Figure I-13. Resistivity and breakdown increase with addition of 15nm Ag particles to epoxy [33]	25
Figure II-1. Etching and Functionalization of TiO ₂ particles.....	33
Figure II-2. Example of DSC curve for TiO ₂ -PVDF composite.....	38

	Page
Figure II-3. Schematic of Raman spectroscopy technique [82]	40
Figure II-4. Method for determining system compliance, $C_s=2.8 \cdot 10^{-5}$	42
Figure II-5. Schematic of TSC experiment: temperature and electric field profiles as a function of time.....	45
Figure II-6. Schematic of the second technique used for dielectric breakdown measurements.	47
Figure II-7. Representation of D-E loops and the corresponding recoverable and lost energies.....	49
Figure III-1. Fracture SEM of non-treated TiO ₂ -PVDF composites with 4.6vol% (a)NS, scale 5 μ m (b) MS, scale 5 μ m (c) NR, scale 500nm (d) NW, scale 4 μ m.....	50
Figure III-2. ATR FTIR spectra of (a) pure PVDF and 4.6vol% TiO ₂ -PVDF with (b)NS (c) NR (d) MS and (d) NW dried at room temperature.....	52
Figure III-3. (a) Dielectric constant of pure PVDF and 4.6vol% TiO ₂ -PVDF composites (b) excludes 4.6vol% NR-PVDF for clarity.....	54
Figure III-4. Dielectric loss of pure PVDF and 4.6vol% TiO ₂ -PVDF composites...	55
Figure III-5. Size and aspect ratio effects on TiO ₂ -PVDF dielectric constant.....	58
Figure III-6. Weibull plot for the different composites compared to the pure PVDF.....	59
Figure III-7. Schematic of electric field distortion with the presence of aligned vs randomly dispersed NW.....	60
Figure III-8. D-E loops of 4.6vol% TiO ₂ -PVDF at 50MV/m 100Hz.....	61
Figure III-9. Energy density of 4.6vol% TiO ₂ -PVDF from D-E loops as a function of electric field	62
Figure III-10. Energy efficiency of 4.6vol% TiO ₂ -PVDF from D-E loops as a function of electric field.....	62
Figure IV-1. XPS measurements of as-received and APS-treated nano wires.....	64

	Page
Figure IV-2. Effect of functionalization on TiO ₂ NWs dispersion and interaction with PVDF (2.3vol% NW-PVDF) (a) Non-treated (b) Functionalized.....	66
Figure IV-3. Cross-section SEM of (a) 4.6vol% F(NW)-PVDF and (b) 9.2vol% F(NW)-PVDF.....	66
Figure IV-4. Schematic of the particles distribution in the composite the cross-sections when the fracture is in 0° Vs 90° directions.....	67
Figure IV-5. Normalized Raman spectroscopy of cross-sections of (a) 2.3vol% (b) 4.6 and (c) 9.2vol% F(NW)-PVDF.....	68
Figure IV-6. ATR FTIR spectra of (a) pure PVDF, (b) 2.3vol% (c) 4.6vol% and (d) 9.2vol% TiO ₂ -PVDF with functionalized nano wires. The red arrows indicate γ peaks.	69
Figure IV-7. Young's modulus as a function of TiO ₂ nano wires content.....	72
Figure IV-8. (a) Dielectric constant and (b) loss tangent of pure PVDF and 2.3 vol% treated and non-treated TiO ₂ NW -PVDF composites.....	73
Figure IV-9. Comparison of the dielectric constant of 2.3vol% F(NW)-PVDF composite to Bruggeman models for aligned wires (Parallel and perpendicular to the particles alignment)	75
Figure IV-10. Dielectric constant of pure PVDF and 2.3, 4.6 and 9.2vol% treated TiO ₂ NW -PVDF composites.....	76
Figure IV-11. Dielectric loss of pure PVDF and 2.3, 4.6 and 9.2vol% treated TiO ₂ NW-PVDF composites.....	77
Figure IV-12. Electrical conductivity of pure PVDF and 2.3, 4.6 and 9.2vol% treated TiO ₂ NW -PVDF composites.....	77
Figure IV-13. Dielectric breakdown and electrical conductivity at 20Hz as a function of particles content.....	79
Figure IV-14. Schematic of nano wires distribution in (a) 2.3, (b) 4.6 and (c) 9.2vol%.....	81
Figure IV-15. Energy density of F(NW) TiO ₂ -PVDF from D-E loops as a function of electric field	81

	Page
Figure IV-16. Energy efficiency of F(NW) TiO ₂ -PVDF from D-E loops as a function of electric field.....	82
Figure IV-17. TSC measurements (a) for all the temperatures range (b) Around T _g and (c) at higher temperatures.....	85
Figure IV-18. Thickness dependence of breakdown electric field.....	89
Figure IV-19. SEM of a hole caused by breakdown on a (a) pure PVDF sample and (b) 4.6vol% F(NW)-PVDF sample.....	89
Figure V-1. SEM images of 3wt% F(NW)-0.5wt% Ag-PVDF with (a) Ag ex-situ and (b) Ag in-situ.....	90
Figure V-2. EDS of 3wt% F(NW)-0.5wt% Ag-PVDF (in-situ) shown in Figure V-1 (b)	91
Figure V-3. TEM images of 3wt% F(NW)-0.5wt% Ag-PVDF (a) and (b) Ag in-situ; (c) and (d) Ag ex-situ.....	92
Figure V-4. FTIR spectra of F(NW)-Ag-PVDF composites compared to the pure PVDF.....	93
Figure V-5. Dielectric constant of two- and three-phase Ag-F(NW)-PVDF composites compared to the pure PVDF.....	94
Figure V-6. Dielectric loss of two- and three-phase Ag-F(NW)-PVDF composites compared to the pure PVDF.....	95
Figure V-7. Dielectric constant of 3wt% F(NW)-PVDF and the corresponding maximum Ag radius required for Coulomb blockade effect to occur...	96
Figure V-8. Current as a function of electric field for the pure PVDF and composites with Ag nanoparticles and TiO ₂ nano wires measured at room temperature.....	98
Figure V-9. Current as a function of electric field for the pure PVDF and composites with Ag nanoparticles and TiO ₂ nano wires measured at -100C.....	98
Figure VI-1. Flexible NW-PVDF composite.....	105

LIST OF TABLES

	Page
Table I-1. List of dielectric constant of common polymers used for capacitors [41].....	8
Table I-2. List of dielectric constant of common ceramics used for capacitors [41].....	9
Table I-3. List of dielectric breakdown of common polymers used for capacitors [41].....	10
Table II-1. Summary of TiO ₂ particles dimensions.....	31
Table II-2. Characteristic peaks for PVDF phases α , β and γ [70-74].....	36
Table III-1. Degree of crystallinity of TiO ₂ -PVDF composites.....	53
Table III-2. DC Breakdown measurements for PVDF and 4.6vol% TiO ₂ -PVDF composites	59
Table IV-1. Analysis of XPS data; atomic percentage on the TiO ₂ surface.....	65
Table IV-2. Degree of crystallinity of F(NW)-PVDF composites.....	70
Table IV-3. DC Breakdown measurements for PVDF and NW TiO ₂ -PVDF composites.....	78
Table IV-4. Activation energy calculated from dielectric spectroscopy.....	84
Table V-1. Degree of crystallinity of the 2- and three-phase composites compared to PVDF.....	94
Table V-2. Resistivity measurements at 25 and -100°C.....	97
Table V-3. Dielectric properties of three-phase composites compared to the pure PVDF and two-phase composite.....	99
Table V-4. Activation energy calculated from dielectric spectroscopy.....	101

CHAPTER I

INTRODUCTION AND PROBLEM STATEMENT

1. Motivation

Power requirements for mobile electronic devices, hybrid electric vehicles and military applications are increasing along with a need for lightweight, compact, high energy density capacitors. At the same time, monolithic materials are reaching a plateau in terms of energy storage capabilities due to the trade-off between dielectric constant, dielectric loss and voltage breakdown [1]. For example, ceramics have high dielectric constant but high dielectric loss and low dielectric breakdown; on the other hand, polymers have high dielectric breakdown and low loss but a low dielectric constant. Polymer nanocomposites have the potential to overcome these limitations through a synergistic coupling of high dielectric constant nanoparticles in high dielectric breakdown polymer matrices.

Many variables affect the composites effective properties such as the inherent properties of polymer matrix and particles, the particle size, particle content and the interaction between the particles and the polymer. As the particle size decreases, the interfacial surface area to volume ratio increases. And as it reaches below 100nm, the

This dissertation follows the style of IEEE Transactions on Dielectrics and Electrical Insulation.

effect of the interface on the composite's properties becomes significant. As a matter of fact, 5nm spherical particles have 200 times the surface area of 1 μ m particles. Furthermore, the particle aspect ratio affects the particle distribution in the composite, and hence, it impacts the resulting local field. A stronger interaction between the particles and the polymer matrix results in a better dispersion of the particles, less nanovoids around the particles and more restriction of the polymer chains movement, which consequently impacts the effective properties.

Numerous research studies have shown that the addition of high dielectric ceramic particles to a polymer matrix leads to an enhancement in the dielectric properties, ranging from measurable but small to significant [2-27]. However these studies lack a deeper examination of how the dielectric properties can be optimized by tailoring the aforementioned variables. In this work, we propose to tailor the particles size, aspect ratio, content and interaction with the polymer matrix in order to improve the composite's properties by simultaneously increasing the dielectric constant and dielectric breakdown without increasing the loss. We also propose to study the effect of adding metallic nanoparticles, to the two-phase composite, on the dielectric and electrical properties.

It has been reported in the literature that adding a very low content metallic nanoparticles to a polymer, below percolation threshold, led to an increase in dielectric breakdown and electrical resistivity [28-33]. This phenomenon is attributed to a quantum mechanics effect called Coulomb blockade effect or quantum confinement. At the nanoscale, some materials properties change; namely the electrical and electronic

properties of metallic particles such as silver and gold [34-38]. These metallic particles become insulating at a certain size in a specific medium. This phenomenon happens when the energy required to transfer an electron through a metallic particle is higher than the thermal energy available in the system.

The energy required for the electron transfer to a spherical particle of radius R is written as:

$$E = \frac{e^2}{8\pi \cdot \epsilon_0 \cdot \epsilon \cdot R} \quad (\text{I-1})$$

The thermal energy is: $E_T = k_b T$

where

e	Electron charge
ϵ_0	Vacuum permittivity
ϵ	Medium dielectric constant
R	Particle radius
k_b	Boltzmann constant
T	Temperature (K)

This quantum confinement phenomena happens when $E > E_T$, therefore the maximum radius of the particles below that the Coulomb blockade effect happens is:

$$R < R_{max} = \frac{e^2}{8\pi \cdot \epsilon_0 \cdot \epsilon \cdot k_B T} = \frac{8.34 \cdot 10^{-6}}{\epsilon T} \quad (\text{I-2})$$

Trapping more charges in the composite would lead to higher dielectric breakdown since the creation of a conductive path would require more energy.

Therefore, to the two-phase composite giving the highest dielectric constant and breakdown, Ag nanoparticles were added to take advantage of the Coulomb blockade effect and further increase the breakdown and hence the energy density.

2. Background and literature review

(a) *Dielectric properties*

(i) *Low-electric field properties*

Dielectric materials are insulators that can be used to store electrical energy through charge separation by an external electric field [39]. When the electric field is applied, the material responds by redistributing its charges to some extent. This phenomenon is called polarization of the material. Equation I-3 gives the capacitance of a parallel plate capacitor, having a dielectric between the plates.

$$C = \epsilon C_0 \quad (\text{I-3})$$

where C_0 is the vacuum capacitance and ϵ is the capacitor's material permittivity that is related to the polarization P by (I-4).

$$\epsilon = 1 + \frac{P}{\epsilon_0 E} \quad (\text{I-4})$$

with ϵ_0 is the vacuum permittivity ($8.854 \cdot 10^{-12}$ F/m) and E is the applied electric field.

The complex permittivity of a material can be written as:

$$\epsilon^* = \epsilon' - j\epsilon'' \quad (\text{I-5})$$

where ϵ' and ϵ'' are the real and imaginary parts of the permittivity, respectively, and $j = \sqrt{-1}$. ϵ' represents the materials ability to store charge and it is related to the materials capacitance while ϵ'' represents the dielectric loss, the energy dissipated by the material under an applied electric field. ϵ' and ϵ'' may be visualized by the Figure I-1.

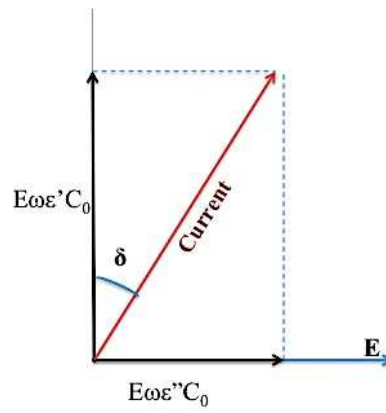


Figure I-1. Current-voltage diagram of a dielectric with loss [40]

In an ideal condenser, of geometric capacitance C_0 , with instantaneous polarization, the charging current $E\omega\epsilon' C_0$ is 90° out of phase with the alternating potential. In a real material, a loss current $E\omega\epsilon'' C_0$, in-phase with the potential, is present. The angle δ is the loss angle. The tangent of δ is the loss tangent:

$$\tan(\delta) = \frac{\text{Loss current}}{\text{Charging current}} = \frac{\epsilon''}{\epsilon'} \quad (\text{I-6})$$

The relative permittivity of a material, also called dielectric constant, ϵ_r is related to the real part of permittivity by:

$$\varepsilon' = \varepsilon_0 \cdot \varepsilon_r \quad (\text{I-7})$$

ε'' is calculated by (I-8):

$$\varepsilon'' = \varepsilon' \cdot \tan(\delta) \quad (\text{I-8})$$

The parameters, ε' , ε'' and $\tan(\delta)$ are frequency dependent. A polymer composite dielectric response is governed mainly by four polarization mechanisms:

Electronic polarization: An electric field will cause a slight displacement of the electron cloud of any atom in the polymer molecule with respect to its nucleus. However the displacement is small because the applied field is usually weak compared to the intra-atomic field at the electron by the nucleus. Typically, the time required for electronic polarization is around 10^{-15} second and the contribution to the dielectric constant is about 2.

Atomic polarization: Under an electric field, atomic nuclei's arrangement is distorted in the polymer molecules. And because nuclei are heavier than electrons, atomic polarization does not happen at higher frequencies ($>10^{13}$ Hz) and its contribution to the system's polarization is smaller than electronic polarization. In the case of polymer, atomic polarization is only one tenth of the electronic polarization.

Dipolar polarization: Also called "orientation polarization". If the polymer has a permanent dipole, the dipole tends to align itself with the applied electric field. The inherent dipoles require molecular motion to respond to the applied electric field; therefore dipolar polarization highly depends on molecule-molecule interaction in the

polymer. Orientation polarization can have a significant contribution in the material's polarization; however it is slow. It requires 10^{-9} second.

Interfacial polarization: Maxwell pointed out that in heterogeneous dielectrics accumulation of virtual charge at the interface between two media of different electrical properties results in a polarization [40]. Electronic, atomic and dipolar polarizations are all due to charges that are locally bound in atoms and molecules. However in addition to the bound charges, charge carriers exist in the material and can migrate through for some distance in the dielectric. If the carriers movement is constrained either by being trapped in the material or at an interface, space charge and a macroscopic field distortion happen.

Such a distortion appears as an increase in the material's capacitance, and therefore its dielectric constant. Interfacial polarization may be detected in a polymer composite even in the absence of polarization of polar particles, or even if the particles are nonpolar. In any composite with materials of different electrical properties, interfacial polarization is expected. It mainly influences the low frequencies dielectric properties ($10^{-5} - 10^2$ Hz).

Table I-1 and Table I-2 list common polymers and ceramics' dielectric constants.

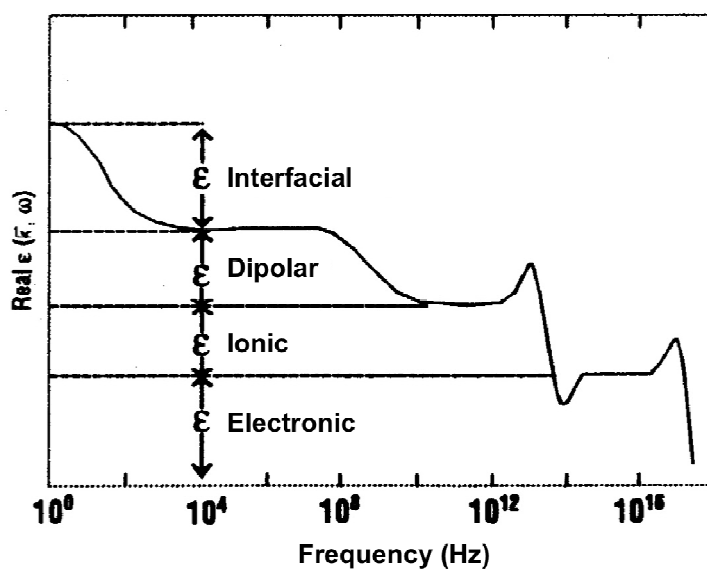


Figure I-2. Frequency dependence of the dielectric constant*

Table I-1. List of dielectric constant of common polymers used for capacitors [41]

Polymer	Dielectric permittivity
Nonfluorinated aromatic polyimides	3.2-3.6
Fluorinated polyimide	2.6-2.8
Poly(phenyl quinoxaline)	2.8
Poly(arylene ether oxazole)	2.6-2.8
Poly(arylene ether)	2.9
Polyquinoline	2.8
Silsesquioxane	2.8-3.0
Poly(norborene)	2.4
Perfluorocyclobutane polyether	2.4
Fluorinated poly(arylene ether)	2.7
Polynaphthalene	2.2
Poly(tetrafluoroethylene)	1.9
Polystyrene	2.6
Poly(vinylidene fluoride-co-hexafluoropropylene)	~12
Poly(ether ketone ketone)	~3.5

* <http://electrochem.cwru.edu/encycl/art-d01-dielectrics.htm>
 Picture altered for more clarity

Table I-2. List of dielectric constant of common ceramics used for capacitors [41]

Composition	Dielectric permittivity
BaTiO ₃	1,700
PMN-PT (65/35)	3,640
PbNb ₂ O ₆	225
PLZT (7/60/40)	2,590
SiO ₂	3.9
Al ₂ O ₃	9
Ta ₂ O ₅	22
TiO ₂	80
SrTiO ₃	2,000
ZrO ₂	25
HfO ₂	25
HfSiO ₄	11
La ₂ O ₃	30
Y ₂ O ₃	15
α -LaAlO ₃	30
CaCu ₃ Ti ₄ O ₁₂	~60,000
La _{1.8} Sr _{0.2} NiO ₄	~100,000

(ii) *High-electric field properties*

Dielectric breakdown is the irreversible failure of a dielectric material by transition from insulating to conductive state when subjected to a high electric field. Each material has a range of electric fields at which the catastrophic failure happens. This range depends on the material, the defects density in the sample, duration of exposure to the electric field and the conditions of the measurement. Table I-3 shows some examples of common polymers' dielectric breakdown.

Table I-3. List of dielectric breakdown of common polymers used for capacitors [41]

Polymer	Dielectric Strength (V/μm)
Polyethylene (LD)	200
Polyethylene (HD)	200
Polyethylene (XL)	220
Polypropylene (Biaxially oriented)	200
Polystyrene	200
Polytetrafluoroethylene	88-176
Poly(vinylidene fluoride)	10.2
Polycarbonate	252
Polyester	300
Polyimide	280
Epoxy resin	25-45

Dielectric breakdown is a statistical phenomenon. It can be intrinsic or extrinsic, initiated by defect in the material or the surrounding environment.[42, 43] In order to improve a system's performance, it is important to understand what causes its breakdown. Dielectric breakdown in polymeric systems is not well understood [41, 44]. Dielectric breakdown phenomenon can be summarized as follows:

- The breakdown has a statistical characteristics and it follows a Weibull distribution [44-47].
- The intrinsic breakdown, representing the “true” strength of the material, has no thickness dependence [44, 48, 49]. It lies in a very narrow band for different materials, and it can be achieved with the thinnest samples and with the shortest duration of applied electric fields as shown in Figure I-3.
- The final result of breakdown is always the formation of a plasma channel.

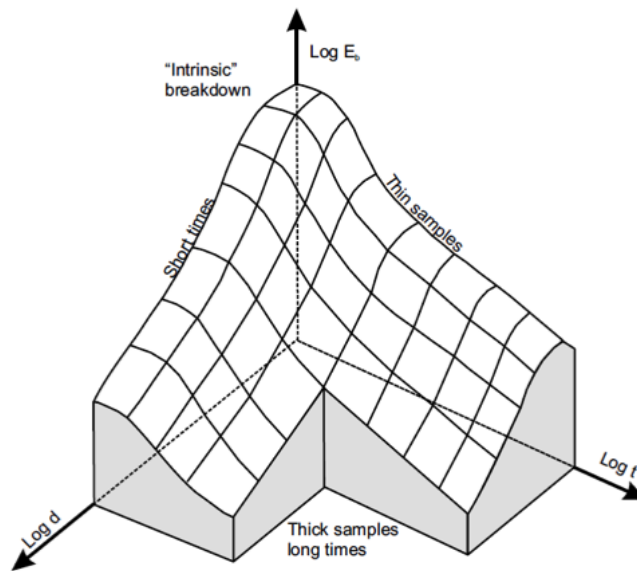


Figure I-3. Schematic representation of the relationship between the breakdown field E_b , the time to breakdown t , and the sample thickness d [44]

- The presence of defects, such as free volume and additives, inside the material shortens the time for failure to happen [50].
- Mechanical stress can induce the dielectric breakdown; this is mainly due to the electrostatic forces that pull the electrodes to each others when the electric field is applied (Electromechanical breakdown) [44].
- The increase in the electrical conductivity and temperature within the sample play cause/effect roles in accelerating the dielectric breakdown: an injection of electrons into the polymer causes it to heat by Joule effect, which then gives more energy to more electrons to travel through the sample, therefore increasing the electrical conductivity. These processes are called electronic and thermal breakdowns. Electronic breakdown is usually indicated by very small sparks and ticking during

the electric field ramp; it may take up to 10 seconds before catastrophic failure happens. Up to a certain electric field, the sample is able to dissipate the excess power from electrons movement into heat. Then when a critical electrical field is reached, thermal runaway takes place saturating the dissipated power causing the temperature to increase without control creating a hole in the sample in most times.

- In polymers, the breakdown is most likely thermally and electronically driven [51]. In reference [52] it is claimed that the electrons tunneling would cause the ionization of the polymer macromolecules initializing the dielectric breakdown at an ultimate (theoretical) breakdown field of 10^9V/m , if no defects are considered to be present. In reference [53] it is stated that in polymers discharge may cause a drastic increase in temperature that the polymer may melt creating a cavity in the material.
- The dielectric breakdown happens usually as a result of competition and/or cooperation between different mechanisms: Electronic, thermal, electromechanical and partial discharge.

(b) Nanodielectrics

Monolithic materials are limited with their inherent properties to satisfy the demands for higher energy storage capacitors. This is due to the trade-off between dielectric constant and dielectric breakdown. For example, polymers have high dielectric breakdown, but most of them have a dielectric constant lower than 10. On the other hand, ceramics have dielectric constants, in the range of thousands sometimes, but also they have very low dielectric breakdown. A universal relationship between dielectric

constant and dielectric breakdown, $E_b \propto (\epsilon')^{-1/2}$, is proposed in reference [1] based on experimental measurements as shown in Figure I-4.

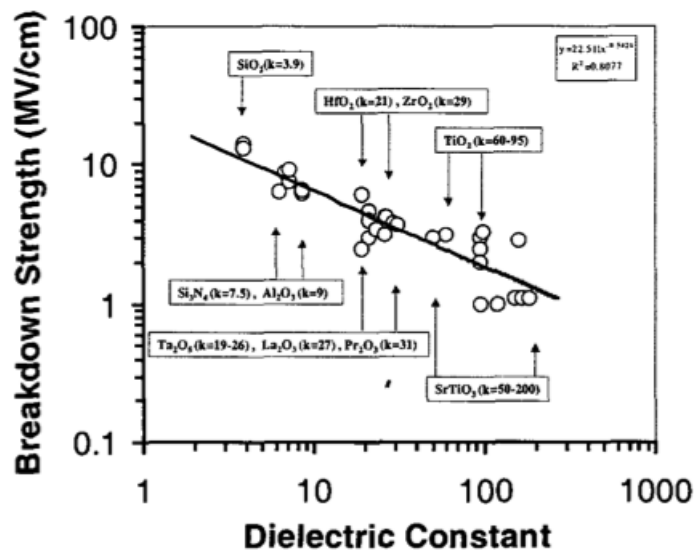


Figure I-4. Dielectric breakdown vs dielectric constant, coefficient is 0.81 [1]

The term “NanoDielectrics” was proposed in 2001 [54] as “a multi-component dielectric possessing nanostructures, the presence of which lead to changes in one or several of its dielectric properties”. This notion includes nanostructured ceramics and tailored polymer nanocomposites [54]. Polymer nanocomposites are polymers in which particles with at least one dimension in less than 100nm are homogeneously dispersed. In contrast to conventional microcomposites, nanocomposites require lower particles loading to show a significant improvement in effective properties due to the tremendous interfacial surface area between the nanoparticles and the polymer matrix [55]. Polymer nanocomposites represent promising candidates to overcome the limitation faced by

monolithic materials and conventional microcomposites in terms of energy density due to the enhanced electrical properties [55-57].

Enhancing the dielectric properties of polymers by the addition of nanoparticles has been extensively studied [2-20, 54-57]. A wide selection of particles have been used for this purpose such as barium titanate (BaTiO_3) [3-9], titanium dioxide (TiO_2) [10-13], zinc oxide (ZnO), aluminum oxide (Al_2O_3) [14-16] and zirconium dioxide (ZrO_2) [17]. Roy et al stated that the addition of silica nano spherical particles to the polymer matrix reduces the carriers mobility; hence increases the breakdown electric field [2]. The treatment of the silica nanoparticles further increased the dielectric breakdown. The most significant improvement in breakdown (65%) was with a polar coupling agent, however with that coupling agent the dielectric properties did not increase. Dou et al investigated addition of BaTiO_3 (100nm diameter) to PVDF, and saw a decrease in the dielectric breakdown of about 35% in the case of untreated spherical BaTiO_3 particles [7]. They attributed the decrease to the low dielectric breakdown of BaTiO_3 . In the same reference, the treatment of the spherical particles is shown to increase the composite's dielectric breakdown by around 125% up to 7 volume percent loading of the particles; at higher contents, the composite's dielectric breakdown decreases (Figure I-5).

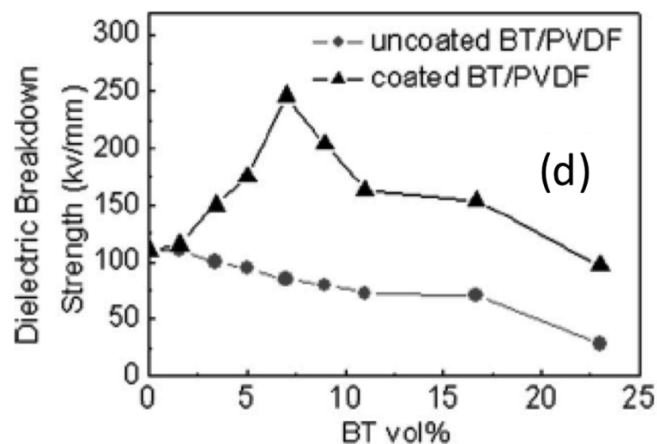


Figure I-5. Functionalization effect on the dielectric breakdown of BaTiO₃-PVDF composites [7]

In reference [9], BaTiO₃ particles (75nm diameter) are added to epoxy at 60vol% loading. The effect of the functionalization solvent was studied in order to achieve the highest dielectric constant which was slightly higher than 50 at 1kHz. This result was achieved when the particles were functionalized in xylene; the BaTiO₃ particles were found to have a better compatibility with the epoxy matrix when treated in xylene solvent. When compared to the pure epoxy, $\epsilon' \approx 3$ at 1kHz, the BaTiO₃-epoxy composite in reference [9] achieved a much higher dielectric constant, however the particles content is very high which may compromise the epoxy's dielectric loss and breakdown as well as mechanical properties. Yang and Kofinas [11] report that well-dispersed TiO₂ spherical nanoparticles were synthesized utilizing a block copolymer as a template and resulted in an increase in the copolymer's dielectric constant as well as a decrease in the loss. Chu et al. measured an increase of 45% in energy density is achieved with 1.6 vol% ZrO₂ spherical nanoparticles in a PVDF terpolymer matrix [17]. In reference [17], the

terpolymer matrix is chosen because of its high dielectric constant, however it also has a very high dielectric loss.

(c) *Particles size and aspect ratio effects*

The interfacial surface area between the particles and the polymer matrix becomes more dominant as the particles size decreases [21]. When a nanocomposite contains 5wt% nanoparticles having a diameter of 40nm, the resulting total surface area is around $3.5\text{km}^2/\text{m}^3$. Between the particles and the matrix, there is a layer that has different properties than both components; one can say it ensures continuity in the system if we assume a good interaction between the particles and the matrix. Depending on the strength of the interaction, the thickness of the layer varies. For any measured physical property, there should be no abrupt discontinuity when going from the particle to the polymer at least in the nano to mesoscale. Figure I-6 is a schematic of a given physical property's continuity from the particle to the polymer matrix.

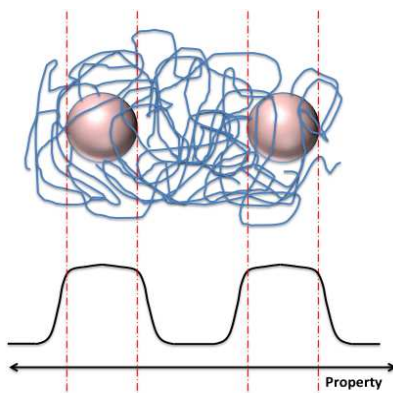


Figure I-6. Physical property continuity between the particles and the polymer matrix.

The interaction zone becomes more significant as the particles size decreases as depicted in Figure I-7.

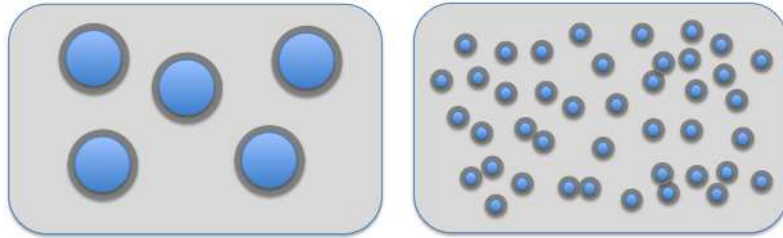


Figure I-7. Schematic of size effect on interfacial volume.

If we take, as an example, a 1vol% composite with spherical particles and if one considers the interphase has a thickness of 5nm, the volume percent of the interphase increases dramatically as the particles size diameter decreases from 1 micron to 5nm as shown in Figure I-8. The interphase volume percent, v_I , for particles with a radius R at a loading volume percent v_P is calculated using (I-9) where t is the interphase thickness.

$$v_I = v_P \frac{(R+t)^3 - R^3}{R^3} \quad (I-9)$$

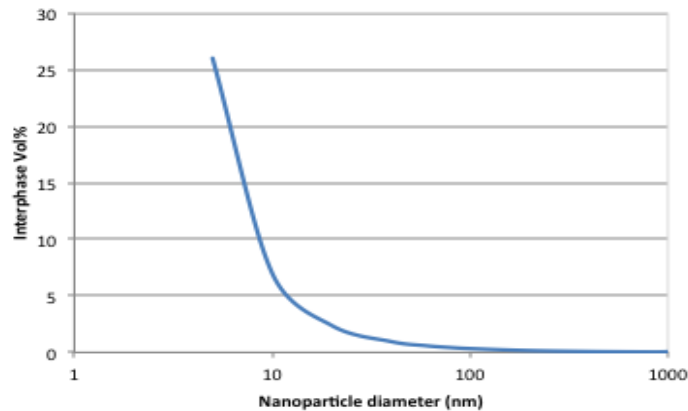


Figure I-8. Interphase volume percent in a 1vol% composite, where the interphase thickness is assumed to be 5nm.

Generally the interphase thickness is estimated to range from 10 to 30nm as suggested by Tanaka in the multi-core model [58]. In the multi-core model, as displayed in Figure I-9, the interphase is described as being made up of three layers:

(1) Bonded layer: This layer corresponds to the polymer chains tightly bonded to the particles when the particles are chemically treated. It has a thickness around 1nm.

(2) Bound layer: This layer is an interfacial region composed of a layer of polymer chains interacting with the first layer and the particles. It usually has a thickness of 2 to 9nm depending on the polymer-particle interaction strength.

(3) Loose layer: More flexible polymer chains interacting with the second layer (bounded layer). This third layer generally has different chain mobility and conformation. It might have more free volume when compared to the first and second layers. The third layer has a thickness in the range of tens of nanometers.

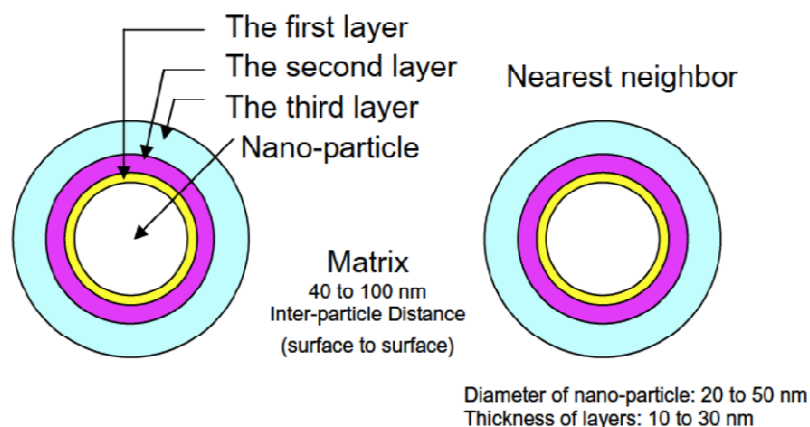


Figure I-9. Multi-core model for nanoparticle-polymer interfaces [58]

In addition to the three layers, the difference and contrast in electrical properties between the particles and the matrix creates charges distribution around the particles. A layer analogous to the stern diffuse layer is superimposed on the three aforementioned layers. Depending on the sign of the particle surface charges, positive or negative, the mobile carriers present in the polymer, if any, distribute themselves in the interface in a counter-charge manner. This charge-driven layer has a significant effect on the dielectric and electric properties of polymer nanocomposites [58-60]. These interfacial layers alter the polymer chains conformation, mobility and physical properties of the region surrounding the particles. And the larger the interfacial surface area is, the more effect the interfacial region properties have on the composite's effective properties.

The particles size effect on the effective dielectric properties has been investigated in [15, 60, 61] where micron sized spherical TiO_2 particles resulted in more

enhancement in the dielectric permittivity compared to nanoscaled particles as shown in Figures I-10 and I-11.

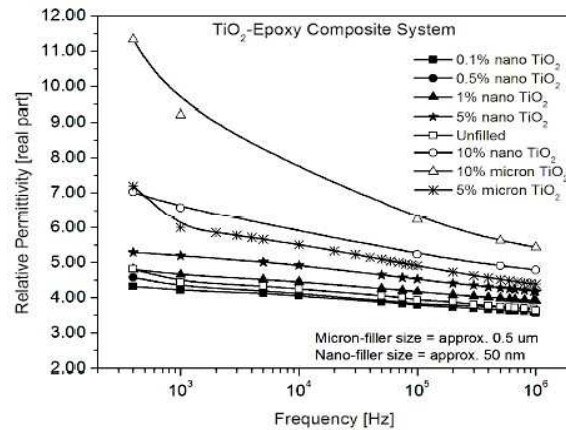


Figure I-10. Dielectric constant for TiO₂-epoxy composites with nanoparticles (50nm) compared to microparticles (0.5µm) [15]

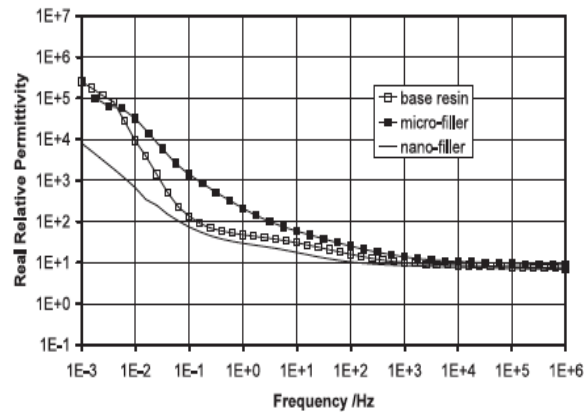


Figure I-11. Dielectric constant for TiO₂-epoxy composites with nanoparticles (23nm) compared to microparticles (0.5µm) [60]

In these studies, the limited enhancement in the dielectric properties by the addition of nanoparticles is justified by the higher interfacial polarization in the microcomposites. Furthermore, pulsed electro-acoustic (EPA) measurements showed that the nanocomposite has lower charge levels compared to the microcomposite [60]. Moreover, the nanoparticles can restrict the motion of the end-chains of the polymer and hence reduce their ability to follow the applied AC electric field. The addition of nanoparticles resulted in less electric field distortions and therefore higher dielectric breakdown compared to the microcomposites.

The effect of particles aspect ratio was studied in reference [22] where it was stated that higher aspect ratio particles have higher local fields along their longitudinal axis resulting in higher effective dielectric constant and lower dielectric breakdown. Guo et al. showed that for the same volume fraction, rod-shaped TiO₂-polypropylene nanocomposites have significantly higher dielectric constant than the sphere-shaped TiO₂-polypropylene nanocomposites. This shape effect is related to the higher polarization resulted when using rod-shaped particles according to the Maxwell-Garnet models and it was demonstrated theoretically by comparing the models for spherical versus ellipsoidal particles as shown in Figure I-12. Equations (I-10) and (I-11) present the models used in Figure I-12 for spherical and ellipsoidal particles, respectively. Where ϵ_1 and ϵ_2 are the polymer and particles dielectric constants, respectively, c is the volume fraction and N_j are the depolarization factors:

$$\epsilon_{eff} = \epsilon_1 \left[\frac{\epsilon_2 + 2\epsilon_1 + 2c(\epsilon_2 - \epsilon_1)}{\epsilon_2 + 2\epsilon_1 - c(\epsilon_2 - \epsilon_1)} \right] \quad (I-10)$$

$$\epsilon_{eff} = \epsilon_1 + \frac{c}{3} (\epsilon_2 - \epsilon_1) \sum_{j=x,y,z} \frac{\epsilon_{eff}}{\epsilon_{eff} + N_j(\epsilon_2 - \epsilon_{eff})} \quad (I-11)$$

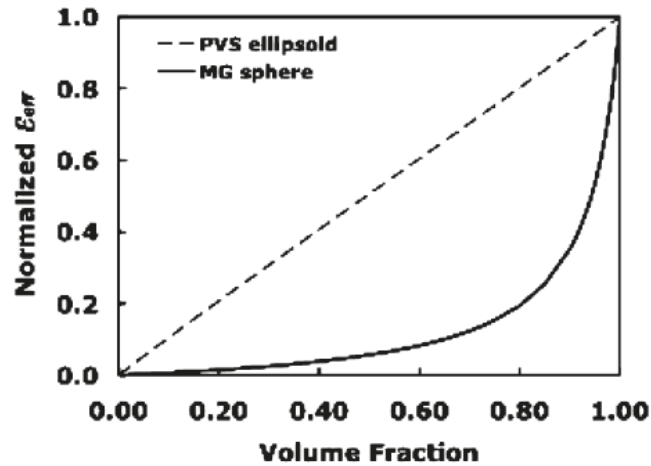


Figure I-12. Normalized calculated effective permittivity $((\epsilon_{eff} - \epsilon_1)/(\epsilon_2 - \epsilon_1))$ for polypropylene composite dielectrics with TiO_2 spherical (solid line) and ellipsoidal particles (dashed line) [22]

On the other hand, the composite with rod-shaped TiO_2 nanoparticles exhibited lower dielectric breakdown compared to the corresponding composites with spherical particles. And this was associated with enhanced localized electric field around the high aspect ratio particles [22]. Wang et al studied the energy storage capabilities of composites made of TiO_2 nano rods and PVDF copolymers [12]. Wang et al measured an 45% increase in the energy storage with the addition of 10vol% TiO_2 nano rods to the P(VDF-TrFE-CTFE) matrix reaching an energy storage of 6.9J/cc. This result is significant because the resulting energy density is much higher than what is commercially available, namely $\sim 2\text{J/cc}$ for biaxially oriented polypropylene. The composite's loss was in the same range as the polymer matrix that is relatively high (around 0.08). Sodano et al. [23] studied the effect of adding PZT nano wires and nano

rods to a PVDF matrix. It was stated in reference [23] that the higher aspect ratio nano wires resulted in better effective properties as compared to the nano rods in terms of dielectric constant and energy. At 50vol% content, the energy storage showed a 30% increase compared to the pure PVDF. However when compared to the pure PVDF, the nano wires PZT-PVDF breakdown decreased with the particles addition. In reference [24], it is stated that the particles dielectric constant is the key to higher energy density composite compared to their aspect ratio. This conclusion was made after comparing the effect of adding either high aspect ratio organically modified montmorillonite (oMMT) to epoxy or high dielectric constant BaTiO₃ spherical particles; they assessed the impact of both fillers on the effective dielectric properties, namely dielectric constant, dielectric breakdown and energy density. They measured an increase in the effective energy density by adding the BaTiO₃ particles; while the energy density did not show any change with the addition of the oMMTs. It is worth noting that there are too many differences in these two systems; particles inherent properties, aspect ratio, distribution (possible percolation for the oMMT particles), making this comparison not suitable to make a simple conclusion about the particles inherent properties' importance in driving the higher energy density of resulting composites.

Different studies show various levels of improvements in dielectric constant and energy density with different particles, shapes and sizes. It is mostly agreed upon that high aspect ratio particles are promising choice for high dielectric constant composites. Furthermore, It seems nanoparticles-modified polymer should exhibit more important improvement due to expected size effect and potential to tune interface to control and

optimize. A dramatic enhancement at low content, which exceeds any behavior predicted by rule of mixture, is expected. Indeed, in traditional composites, the effective properties are a function of particle content and particle inherent properties; in nanocomposites, a number of other variables affect the final properties such as particle size, dispersion, distribution and interfacial interaction with the polymer.

(d) Three-phase composite: Coulomb blockade effect

The higher a material's resistivity is, the better insulating properties it has. In reference [28], it is claimed that the addition of Ag nanoparticles (15nm diameter) to 20wt% BaTiO₃-PVDF increases the composite's resistivity and breakdown from 1400MΩ.m to 2700MΩ.m and from 190MV/m to 290MV/m, respectively, at 0.05wt% loading. Higher than this content, both properties decrease. This is justified by the Coulomb blockade effect, meaning that the Ag nanoparticles are playing the role of insulating islands blocking electrons transport by requiring higher energy than what is available in the system. Lu *et al.* studied the effect of in-situ synthesis of Ag nanoparticles in Carbon black (CB)-epoxy composite on the dielectric properties [29]. They stated that the addition of Ag nanoparticles with an average size of 7nm resulted in a decrease in the dielectric loss and claimed that this is caused by the Coulomb blockade effect. However the two-phase CB-epoxy composite, the dielectric constant at 10kHz is in the range of 1500, which means that for the blockade effect to happen at room temperature, the Ag particles size has to be in the angstrom range. Man *et al.* showed a five-fold increase in the resistivity of epoxy by the addition of 10nm Ag particles and claimed that the Ag nanoparticles are restraining electrons transport at high electric

fields [30]. The same group studied the electrical properties of Ag/PMA/EVA and showed an increase in resistivity and dielectric breakdown with the addition of Ag nanoparticles and related this behavior to Coulomb blockade effect [31]. They also showed a higher enhancement of the composite's resistivity when the Ag size is 10nm compared to 20nm. In reference [32], the addition of Ag nanoparticles of a diameter between 20 and 30nm to PVA matrix results in an increase in the system's resistivity. This increase is more significant at cryogenic temperature because the available thermal energy in the system decreases with the temperature. The same group studied the effect of adding PVP-coated 15nm Ag particles to epoxy matrix. An increase in the resistivity and dielectric breakdown was measured as shown in Figure I-13 [33].

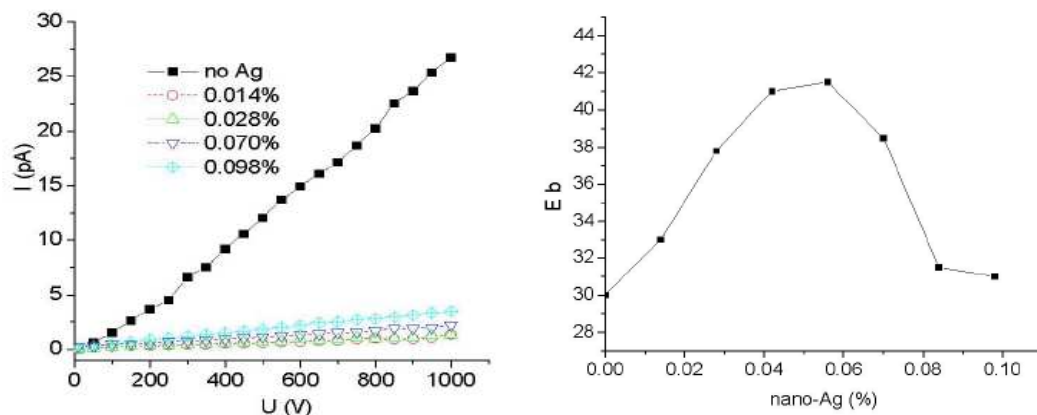


Figure I-13. Resistivity and breakdown increase with addition of 15nm Ag particles to epoxy [33]

3. Problem statement

Conventional microcomposites are not meeting demands for flexible and lightweight high energy density dielectrics. Limitations in performance are based on their dependence only on the inherent properties of the polymer matrix and the added particles; the effective properties follow the rule of mixture. However nanocomposites promise more enhancements due to the high interfacial area between the nanoparticles and the matrix. A stronger interaction between the particles and the polymer, through particles functionalization, further increases the resulting improvements. Furthermore, other variables play a significant role in improving the effective properties of the nanocomposites. Tailoring the particles size, aspect ratio, content, interaction with the polymer matrix, their distribution in the composite and the polymer matrix phase leads to the optimization of the composite's effective properties and simultaneously increase the dielectric constant and the breakdown without significantly increasing the dielectric loss. This is done in this work through the following steps;

➤ **Study of particles size and aspect ratio effects on the dielectric properties, dielectric breakdown and hence the energy density of the composites:**

In this step, TiO₂ particles of different sizes and shapes - nano spheres, micro spheres, nano rods and nano wires - are added to PVDF polymer matrix. TiO₂ particles are chosen for this study because they are commercially available in different shapes and forms and they have a relatively high dielectric constant, between 70 and 100, that does not depend on the particles size, unlike ferroelectric particles. Polyvinylidene fluoride (PVDF) is a very attractive thermoplastic polymer [4, 7, 28, 62-66]; it has the highest

dielectric constant among commercially available homopolymers. The composites effective properties; dielectric properties and dielectric breakdown, are measured and compared in order to access the effect of the particles size and aspect ratio.

➤ **Optimization of the effective properties by varying the particles content, interaction with polymer matrix and orientation in the composite:**

In this step, the particles that lead to the best effective dielectric constant and dielectric breakdown along with maintaining a low dielectric loss are selected to further improve the effective properties. The particles are chemically treated to strengthen the interaction with the polymer matrix. The functionalized particles content is varied in order to obtain an optimum content for the highest improvement. Furthermore, the particles distribution is qualified and related to the composites dielectric properties.

➤ **Study of internal charge behavior and dielectric breakdown mechanisms:**

In this step, the composites internal charge behavior is investigated for a better understanding of the dielectric and electrical properties of the composites. Thermally stimulated currents measurements are carried out on the composites with functionalized particles. Furthermore, activation energies for the different systems are calculated using dielectric spectroscopy relaxations. For a better performance for any system, it is important to understand the failure mechanisms; therefore breakdown mechanisms are investigated.

➤ **Three-phase composites study:**

To further investigate role of interface in controlling transport of electrons, metallic ‘trapping sites’ are considered. A very low content of Ag nanoparticles, namely

0.05wt%, is added to the two-phase composite in order to investigate the effect of the metallic particles on the system's dielectric and electrical properties. The nanocomposite's dielectric properties and dielectric breakdown are measured. The nanocomposite's electrical resistivity is measured at room temperature and at -100°C.

4. Contributions of this work

The particles inherent properties are not the only factor that affects the composite's effective properties. In this work, the effect of the particles size and shape on the low and high-field dielectric properties of a polymer-based nanocomposite is probed in order to select the particles that give the highest improvement when compared to the pure polymer which was not fully studied before.

Chemically treating the particles in order to improve the composite's effective properties has been reported in the literature as previously mentioned in the literature review section. However, optimizing a selected composite in terms of particles content, interaction with the matrix and distribution was not previously reported. The resulting improvement is 500% in the energy density without a significant increase in the dielectric loss with a low particles content of 4.6vol%, which did not sacrifice the polymer's flexibility and lightweight. The improvement in energy density seen in the literature ranges from 30% at 50vol% particles loading [23] to 45% at 1.6vol% particles loading [17].

The addition of Ag nanoparticles led to an increase ranging from 30 to 40% in the electrical resistivity at both room temperature and at -100C. Furthermore, an increase

in the dielectric breakdown, hence energy density, is measured with a low content of 0.05wt% Ag nanoparticles.

CHAPTER II

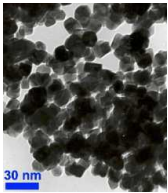
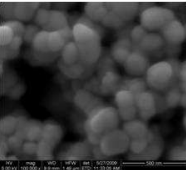
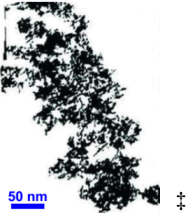
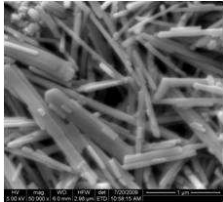
EXPERIMENTAL METHODOLOGIES

1. Materials

Polyvinylidene Fluoride (PVDF) Kynar 301 is purchased from Arkema Inc. TiO₂ rutile nano rods (NR) (10x40nm) and nano wires (NW) (130nmx1.68μm) are products of Nanostructured & Amorphous Materials, Inc and Ishihara Corporation (USA), respectively. TiO₂ anatase nano spheres (NS) (15nm diameter) and micro spheres (MS) (0.5μm diameter) are purchased from Nanostructured & Amorphous Materials, Inc and Sigma Aldrich, respectively. Rutile TiO₂ particles have a relatively high dielectric constant around 100 and anatase TiO₂ particles have a dielectric constant around 70. Table II-1 shows a summary of the TiO₂ particles dimensions with some micrographs of the particles we took and others we got from the vendor. The solvents used in the composites are *N,N*-Dimethylacetamide (DMAc) and *N,N*-Dimethylformamide (DMF) which were purchased from Sigma-Aldrich. For particles functionalization, 3aminopropyltriethoxysilane (APS), Methanesulfonic acid, toluene and isopropanol alcohol were purchased from Sigma-Aldrich.

The chemicals used for the synthesis of Ag particles in-situ are 3aminopropyltriethoxysilane (APS), and silver nitrate (AgNO₃) were purchased from Sigma-Aldrich. PVP-coated Ag particles, with a 6nm diameter, were provided by NanoComposix.

Table II-1. Summary of TiO₂ particles dimensions

Particles	Dimensions	Aspect ratio	
Nano Spheres	15 nm	1	
Micro Spheres	0.5 μm	1	
Nano Rods	10x40 nm	4	
Nano Wires	130nm x 1.6μm	14	

2. Composites synthesis

(a) TiO₂-PVDF composites synthesis

For Chapter III, 10wt%, corresponding to 4.6vol% TiO₂-PVDF, composites with the different particles (NS, MS, NR and NW) were prepared. The non-treated TiO₂ particles were dried at 195°C for 12 hours under vacuum prior to mixing in order to

[†] <http://www.nanoamor.com/inc/pdetail?v=1&pid=391>

[‡] <http://www.nanoamor.com/inc/pdetail?v=1&pid=392>

remove the moisture. Three techniques were used in the preparation of the composites: high shear mechanical mixing with ultrasonication followed by magnetic stirring. The first two techniques are used to pre-disperse the particles in the solvent. After 6 hours of mixing, the particles were added to the dissolved PVDF solution and magnetically stirred. Degassing is an important step before casting the solution on glass plates to remove air bubbles which affect the films porosity and hence their dielectric properties. For the composites with non-treated TiO_2 , after degassing the solution, it is and dried at room temperature. After 2 or 3 days of drying in the desiccator, the films were dried under vacuum for 3 hours at 60°C , the free-standing films are characterized. The films thickness is between 27 and $40\mu\text{m}$.

(b) TiO_2 -PVDF composites synthesis with functionalized particles

For Chapter IV, three contents, 5, 10 and 20wt%, were prepared, corresponding to 2.3, 4.6 and 9.2vol% TiO_2 -PVDF composites. The functionalization of TiO_2 particles is carried out using 3-aminopropyltriethoxysilane (APS) in two steps: etching and functionalization as shown in Figure II-1. The etching consists of magnetically stirring TiO_2 particles in a 10 vol% mixture of Methanesulfonic acid and distilled water at 110°C under reflux for 4 hours. Then the particles are thoroughly washed using distilled water and filtered, then dried under vacuum at 120°C for 24 hours. The dried particles are grinded and mechanically mixed in Toluene and APS for 6 hours. The particles are then washed and filtered thoroughly using isopropanol alcohol and then dried under vacuum at 120°C for 12 hours. APS is a polar compound that offers a good compatibility between TiO_2 particles and PVDF through hydrogen bonding. For the particles

dispersion, the same three techniques as the ones used in Chapter II.2. (a) ; high shear mechanical mixing, ultrasonication and magnetic stirring. After degassing the solution, it is cast using the doctor blade and dried under vacuum at 130°C for 1hour then slowly cooled down to room temperature. After drying under vacuum for 3 hours at 60°C, the free-standing films are characterized. The films thickness is between 18 and 60µm.

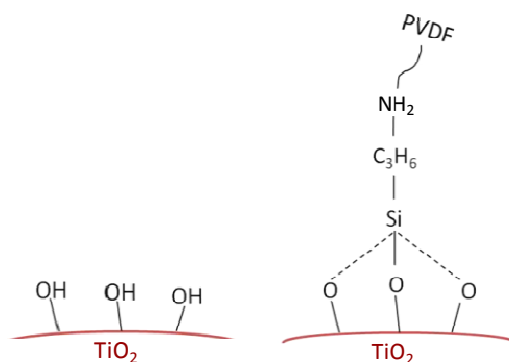


Figure II-1. Etching and Functionalization of TiO₂ particles

(c) *Three-phase composites synthesis*

In the three-phase composites chapter, Chapter V, wt% would be used instead of vol% for more clarity. 3wt% NW-0.05wt% Ag-PVDF composites were synthesized, which is equivalent to 1.4vol% NW-0.0086vol% Ag-PVDF. The NWs used in this section are treated following the same procedure in Chapter II.2. (b) . Two techniques are used to incorporate the Ag nanoparticles in the TiO₂-PVDF composites: ex-situ and in-situ.

For the ex-situ composites, PVP-coated Ag nanoparticles are pre-dispersed in DMF under high-sonication at 450W power for 40 minutes. After that, the Ag-DMF solution is added to a dissolved PVDF solution (in DMF) and magnetically stirred for 8 hours at 400rpm. During this period of time, treated TiO₂ NWs are pre-dispersed in DMF with mechanical stirring (600rpm) and bath sonication. Then NWs-DMF solution is added to Ag-PVDF and magnetically stirred overnight at 400rpm.

For the in-situ synthesized Ag particles, silver nitrate and the coupling agent (APS) were added to the PVDF polymer and solvent (DMF) and magnetically stirred for 40 hours at 400rpm. After 32 hours from the start of the process, pre-dispersing the NW particles in the solvent is started to last for 8 hours under mechanical stirring and bath-sonication. After that, (NWs+DMF) solution is added to the polymer solution where the Ag nanoparticles are then formed and well dispersed.

Once the solution is ready, it is degassed, then cast on a glass plate using a doctor-blade and put in a humidity-controlled environment (desiccator) for 2-3 days until dry. Then it is dried at 60°C under vacuum for 3 hours.

3. Scanning electron microscopy

The dispersion of TiO₂ particles in the films was investigated by imaging their cross-sections using Quanta 600 field emission scanning electron microscope (FESEM) (for Chapters III and IV), Hitachi S-3500 (For Chapter IV) and NanoSEM 630 (For Chapter V). The latter is equipped with Energy-dispersive X-ray spectroscopy (EDS) technique, which is used for elemental analysis. In order to image cross-sections of the different films, samples were fractured in liquid nitrogen due to polymer's ductility. The

crack is initiated by a sharp razor blade. The sample is then fixed on a Ted pella[®] special fixture using a double-sided carbon tape. Contamination are critical to be avoided when doing microscopy, therefore before samples preparation, SEM fixtures are cleaned with acetone. Prior to imaging, the cross-sections were coated with a conductive layer (3-8nm thickness) to avoid charging due to the electron-beam in the SEM. FEI Quanta 600 has a resolution that ranges from 1.2 to 3nm and it was used under 10kV. Hitachi 3500N has a resolution of 3.5nm and was used under 20kV. And NanoSEM 630 has a resolution ranging from 1 to 3nm and was used under 10kV.

4. Transmission electron microscopy

The dispersion in the three-phase composites is qualified using Philips420 transmission electron microscope (TEM). Philips420 has a 0.34nm resolution. The acceleration voltage was varied between 100 and 120kV depending on the samples charging. In order to acquire high resolution imaging using TEM, samples thickness has to be less than 100nm. Samples were superglued to an epoxy block, so that they can be held in an ultramicrotome. Then thin sections, around 90nm, were collected onto 200 hex mesh copper grids at cryogenic temperature (-120°C). Cryogenic temperature is required for low T_g polymers in order to obtain a brittle surface to be sectioned.

5. Fourier transform infrared (FTIR) spectroscopy

PVDF is polymorphic; it has three possible phases: a non-polar phase, α , or a polar phase, β or γ . Different phases have different dielectric properties [66-69], for example α -phase has the highest dielectric constant while β -phase exhibits piezoelectric

and pyroelectric characteristics. FTIR identifies which phase is dominant in the pure polymer and the composites with and without particles whether used as received or functionalized. Attenuated Total Reflectance ATR-FTIR measurements identify the dominant phase in PVDF with and without particles. Results presented in Chapter III were done using a Nicolet 380 FTIR spectrometer. Measurements presented in Chapters IV and V were carried out using a Bruker IFS 66/S FT-IR Spectrometer. For each sample, a couple of measurements are run to ensure the uniformity and repeatability of the measurements. FTIR does not require specific sample geometry. The most important preparation step is to make sure the sample's surface is not contaminated and cleaning it while wearing gloves right before the measurement. The most distinguishable peaks for the most common phases of PVDF, α , β and γ , are summarized in Table II-2.

Table II-2. Characteristic peaks for PVDF phases α , β and γ [70-74]

Wavenumber (cm-1)	PVDF Phase
532	α -phase
614	α -phase
764	α -phase
796	α -phase
812	γ -phase
833	γ -phase
840	β -phase
1233	γ -phase
1276	β -phase

6. X-Ray photoelectron spectroscopy (XPS)

X-ray photoelectron spectroscopy (XPS) is a quantitative spectroscopic technique useful in identifying the elemental composition, chemical state and electronic state of the elements that exist on the surface of the material. XPS spectra are obtained by irradiating the sample's surface with low-energy (~ 1.5 keV) X-rays, in order to provoke the photoelectric effect. The energy spectrum of the emitted photoelectrons is determined by a high-resolution electron spectrometer. The binding energy of the electron in the atom, BE , is equal to the x-ray energy, $h\nu$, less the electron kinetic energy, KE , and the spectrometer work function, ϕ :

$$BE = h\nu - KE - \phi \quad (\text{II-1})$$

The number of electrons detected is proportional to the concentration in the sample and every binding energy peaks are characteristic to each element [75]. Kratos Ultra XPS was used to study the surface chemistry of the TiO_2 particles as-received and chemically treated. Kratos Ultra XPS has a depth of 5nm and a surface sensitivity that ranges from 1 to 10nm.

7. Differential scanning calorimetry (DSC)

DSC is an effective thermal analysis tool to characterize the physical properties of a polymer such as degree of crystallinity, crystallization and melting temperatures, in the case of a semicrystalline polymer, and glass transition temperature [76, 77]. While varying the temperature at a constant rate, DSC measures the difference in heat flow between the sample and a reference at the same temperature. The reference in our case is

an empty aluminum pan similar to the pan where the sample is enclosed. The samples weight ranges between 4 to 6mg. And since the DSC is at a constant pressure, the change in heat flow corresponds to the enthalpy changes. Figure II-2 shows an example of a DCS curve showing the crystallization and melting temperatures and the fusion enthalpy from which the degree of crystallinity is derived. Usually two cycles of heating and cooling are carried out. The first cycle is run in order to remove any thermal history the sample might have.

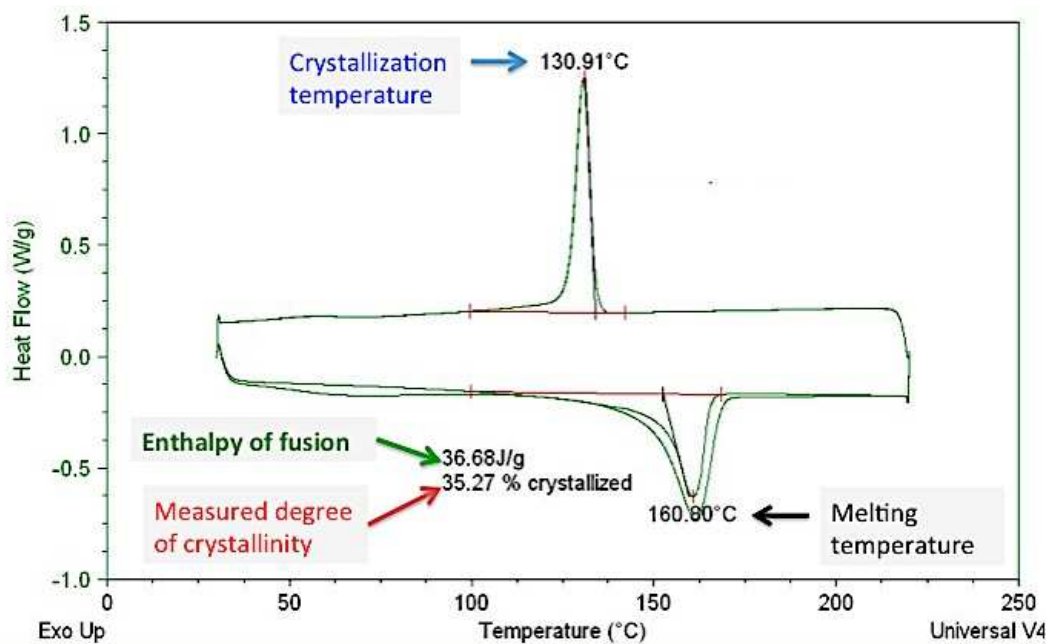


Figure II-2. Example of DSC curve for TiO₂-PVDF composite

The degree of crystallinity, X_c , is calculated using the enthalpy of fusion at the melting point, $\Delta H_m(T_m)$, using (II-2).

$$X_c = \frac{\Delta H_m(T_m)}{\Delta H_m^0(T_m^0)} \times 100\% \quad (\text{II-2})$$

where $\Delta H_m^0(T_m^0)$ is the enthalpy of fusion of the totally crystalline polymer measured at the equilibrium melting point, T_m^0 [78]. In the case of PVDF, ΔH_m^0 is set to 104.4 J/g, which is in the range of what is mentioned in the literature [79, 80]. The obtained degree of crystallinity from DSC is corrected with respect to the weight fraction of the polymer (w_{Poly}) in the composite following (II-3) [81]

$$X_{c_Corrected} = X_c/w_{Poly} \quad (\text{II-3})$$

To investigate the effect of the particles on the degree of crystallinity of PVDF, DSC measurements were carried out on three samples of each composite using a Q20 TA instruments DSC. Heating and cooling cycles were carried out from 30°C to 220°C with a rate of 10°C/min. Melting and crystallization temperature are determined from the heat flow curves obtained from the first heating and cooling, respectively. After heating the sample beyond the melting point and slowly cooling it, PVDF changes from γ to α phase, therefore the degree of crystallinity was calculated from the first heating in order to get the proper PVDF phase crystallinity.

8. Polarized Raman spectroscopy

Raman spectroscopy is utilized to detect molecular vibrations in materials. When the light beam comes in contact with a material, its constituent photons may be absorbed, scattered or transmitted. If the energy of an incident photon excites a molecule, its energy would be promoted by the material and measured as the loss

between the incident light and the light collected by the detector. This absorbed light's energy corresponds to a specific molecular vibration that characterized the tested material. Figure II-3 displays a schematic of Raman spectroscopy technique.

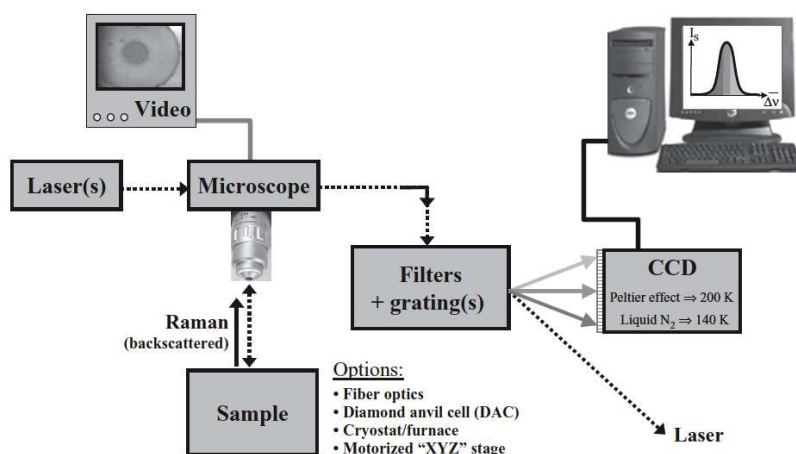


Figure II-3. Schematic of Raman spectroscopy technique [82]

Raman scattering is the inelastic scattering of photons by some excitation of a material. Usually the excitation implied by Raman scattering is a vibrational mode of the atoms of the tested material [83]. Based on the type and energy of vibration, various information can be obtained such as chemical structure, crystallinity, intermolecular interactions and domain orientation in polycrystalline materials. TiO_2 nanoparticles in particular show strong interactions with Raman laser; the different TiO_2 crystal structures, anatase, rutile or brookite, have distinct Raman fingerprints [84-86]. In this study WITec polarized Raman was used to investigate the high aspect ratio particles orientation in the composites. A laser with a 422nm wavelength was used. For each

composite, two cross-sections were obtained by fracturing a sample parallel and perpendicular to the solution casting direction. More details about the cross-sections can be found in Chapter IV1. (b) . For each sample, 5 spots were characterized and then the intensity of the scattered light was averaged. The measurements were normalized with respect to one peak that has an angle-independent intensity.

9. Tensile testing

Mechanical properties were characterized using an Instron 5866 machine using a 10kN-loading cell. The strain rate was set to 1mm/min. Dog-boned shape samples were cut using a template die and a press. Three samples were tested for the characterized composites and the average of the Young's modulus was calculated. A model composite was used to correct for the machine's compliance following the procedure presented in reference [87]. For the system's compliance correction, samples with five different lengths were cut using a sharp razor (three samples for each length). For the different samples, the load was measured as a function of displacement and plotted as shown in Figure II-4.

For each load step, F , the actual measured displacement, ΔL , accounts for the machine's compliance, C_s , as:

$$\Delta L = \Delta l + C_s F \quad (\text{II-4})$$

The real strain has to be corrected for using (II-5).

$$\varepsilon_{Tensile} = \frac{\Delta L - C_s F}{L_0} \quad (\text{II-5})$$

And the linear section of the load is plotted as a function of the real strain and the Young's modulus is calculated as the graph's slope.

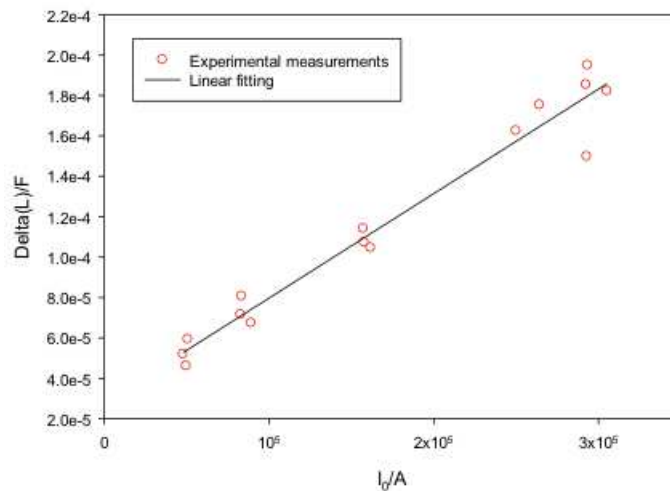


Figure II-4. Method for determining system compliance, $C_s=2.8 \cdot 10^{-5}$

10. Electrical characterization

(a) *Low-electric field measurements*

(i) *Dielectric spectroscopy*

Two techniques were used for dielectric spectroscopy measurements. The measurements shown in Chapter III were obtained using a Novocontrol Alpha-A high performance frequency analyzer at Texas A&M University. This analyzer measures the dielectric and electrical properties over a wide range of frequencies from 10 mHz to 20MHz. The measurements were carried out at room temperature. Prior to making the measurements, 1-cm diameter silver circular electrodes, 100nm thickness, were

deposited on both sides of each sample using an OC Edwards Auto 306 Metal Evaporator.

For Chapter IV and Chapter V, the dielectric spectroscopy was carried out using an Agilent LCR and an oven monitored via a home-built software in the Dielectric Studies Center, Pennsylvania State University. This technique allows measurements over the frequency range of 20Hz-10MHz and temperatures ranging from -140°C to 250°C. The output data for this technique are real part of the capacitance, loss tangent and real part of conductance as a function of frequency. The dielectric constant, ϵ , is calculated using (II-6), where C' is the capacitance real part, t and A are the sample's thickness and electroded area, respectively. And the electrical conductivity, σ , is calculated using (II-7), where G' is the conductance real part.

$$\epsilon = \frac{t \times C'}{A \times \epsilon_0} \quad (\text{II-6})$$

$$\sigma = \frac{t \times G'}{A} \quad (\text{II-7})$$

Prior to making the measurements, 1-cm diameter silver circular electrodes, 100nm thickness, were deposited on both sides of each sample using a Kurt Lesker Lab18 evaporator.

In both cases, for each composite, three samples were tested and the average was calculated for each of the properties.

(ii) *Electrical resistivity measurements*

Resistivity measurements were run at room temperature and at -100°C for the three-phase composites using a pA-meter/voltage source (Hewlett-Packard HP 4140B) associated with a Kepco bipolar operational power supply/amplifier. A function generator HP 3478 controls the oven. All the equipment is computer-monitored via software built in the Dielectric Center at Pennsylvania State University. The voltage is ramped to 500V with a step of 50V and the output current, I, is measured by the pA meter.

The electric field-current measurements are linearly fitted in order to obtain the slope. The sample's resistivity was calculated following (II-8), where D is the electrode diameter, which is equal 1cm.

$$\rho = \frac{\pi \cdot D^2}{4 \cdot slope} \quad (II-8)$$

(b) High-electric field measurements

(i) *Thermally stimulated currents (TSC)*

Thermally stimulated currents technique is a powerful tool to investigate the dielectric relaxations in a polymeric system generated by different polarizations occurring in the system [88, 89]. It was first introduced by Bucci and Fieschi in 1964 [90]. The principle of TSC is to orient the dipoles present in the material by applying an electric field at a high temperature, and then freeze the dipoles by decreasing the temperature under the constant electric field. Subsequent heating of the sample with no electric field

causes the oriented dipoles to relax releasing an electrical current, which is measured as a function of temperature.

The sample is heated to a poling temperature T_p , in our case $T_p=90^\circ\text{C}$, for 30 minutes. An electric field E_p , $E_p=30\text{MV/m}$, is applied to pole the sample for 20 minutes. With the electric field held at E_p , the temperature is decreased to T_0 , $T_0=-100^\circ\text{C}$, in order to freeze the dipoles present in the sample. After 20 minutes, the electric field is switched off and the sample is short-circuited for an arbitrary time of 10 minutes to remove the frictional and stray charges present [91]. The temperature is subsequently ramped to a temperature $T_m > T_p$, in our experiment $T_m=170^\circ\text{C}$. The procedure is summarized in Figure II-5.

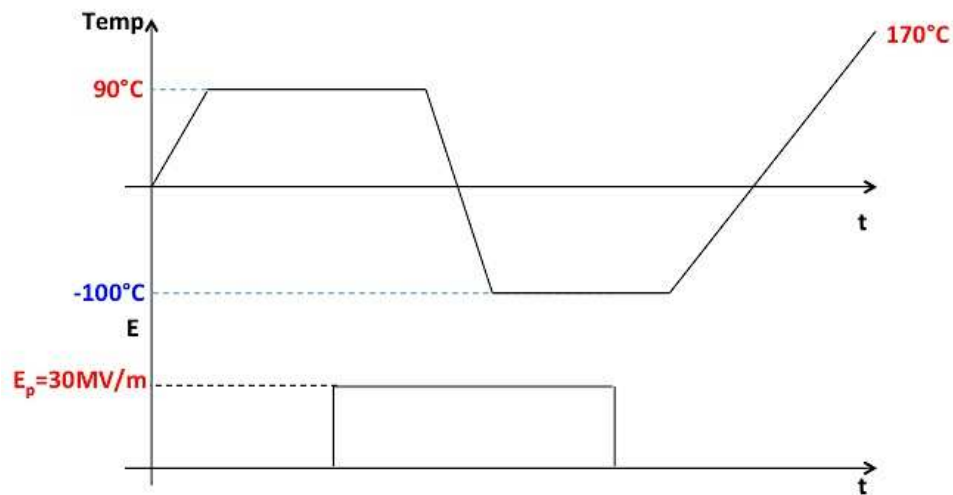


Figure II-5. Schematic of TSC experiment: temperature and electric field profiles as a function of time

(ii) *DC breakdown*

Two techniques for dielectric breakdown measurements were used. The measurements in Chapter III, the measurements were carried out at Lynntech (College Station, Texas) using a DC QuadTech hipot tester. The sample was immersed in a Fluorinert FC-77 high dielectric strength fluid to reduce the air effect on the breakdown measurements. The bottom electrode in this technique is a polished metal electrode. The top electrode is a 1 cm diameter steel cylinder, which is around 75mm long; the top electrode's weight ensures a full contact with the sample. For a smooth contact, to avoid edge breakdown, the top electrode edge that would be in contact with the sample is curved.

The DC breakdown measurements in Chapter IV and Chapter V were carried out at the Center for Dielectric Studies (CDS), PSU. In the second technique, the sample was put on top of a conducting metal electrode. The top electrode is a commercial one-side electroded polypropylene 4 μ m film renewed after each measurement. When the electric field is applied, electrostatic forces pull the top electrode to the sample reducing the surrounding air effect on the dielectric breakdown. This method minimizes the critical stresses that might be created if the electrode is deposited on the sample's surface [92]. A plastic spacer that has a 1cm diameter hole separates the sample from top electrode to make sure the contact between the electrode and the sample is a 1cm diameter disk. Figure II-6 shows a schematic of the fixture used for the second technique dielectric breakdown measurements. A Trek Model 30/20 high voltage amplifier system is used to control the output voltage and monitor the current via a Labview program.

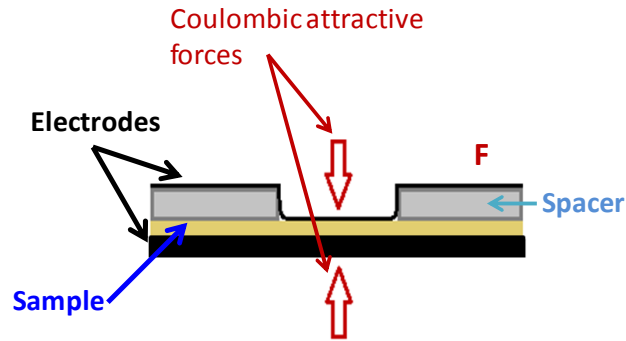


Figure II-6. Schematic of the second technique used for dielectric breakdown measurements. For each composite, at least 12 measurements are taken with a 500V/s ramp.

Weibull model is the statistical analysis tool generally used for electric or mechanical failure study. It is represented (II-9):

$$P(E) = 1 - \exp\left\{-\left(\frac{E}{E_b}\right)^\beta\right\} \quad (\text{II-9})$$

where P is the cumulative probability function of a variable E and β is the shape factor, which corresponds to the measurements scattering parameter. The parameter E_b is the scale parameter which is the value of E at which $P(E)=0.6321$ (that is $1-1/e$ where e is the exponential constant) and it is considered the failure point, dielectric breakdown in our study. The shape factor, β , is a measure of the range of variability of E ; the larger β is, the narrower the range of E is. The shape factor is analogous to the inverse of the standard deviation of the normal distribution. For this study, the scale parameter, E_b , and the shape factor, β , were calculated using Matlab function “wblfit”.

The maximum energy density, of a material of dielectric constant ϵ , is calculated using (II-10).

$$U = \frac{\epsilon\epsilon_0}{2} E_b^2 \quad (\text{II-10})$$

(iii) *AC breakdown*

Electrical displacement is measured under different applied AC electric fields at 100Hz for the different composites. The Trek model 30/20 high voltage amplifier system is used to control the applied electric field at a 500V/s ramp via a Labview program. Before applying the electric field, the sample is mounted in a two-pin fixture and immersed in a high dielectric strength insulating liquid, Galden HT200. The maximum recoverable energy is computed based on the integral in (II-11):

$$U = \int E \cdot dD \quad (\text{II-11})$$

This integral represents the area between the D-E loop and the ordinate as indicated in Figure II-7. The lost energy, U_L , is computed by integrating the area inside the loop, it is associated with the sample's dielectric loss. The system's efficiency is calculated as:

$$\eta = 1 - \frac{U}{U+U_L} \quad (\text{II-12})$$

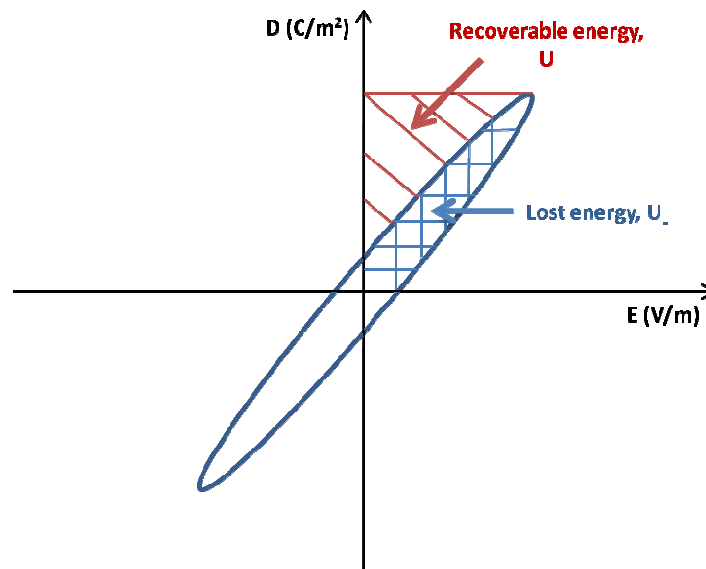


Figure II-7. Representation of D-E loops and the corresponding recoverable and lost energies

CHAPTER III

SIZE AND ASPECT RATIO EFFECTS ON DIELECTRIC PROPERTIES

1. Composites morphology characterization***(a) Particles dispersion***

Representative cross-section micrographs, imaged using Quanta 600 FESEM, of 4.6vol% TiO₂-PVDF composites with the different particles (NS, MS, NR and NW) are shown in Figure III-1. Figure III-1 shows a uniform dispersion of agglomerated as-received particles in all the composites.

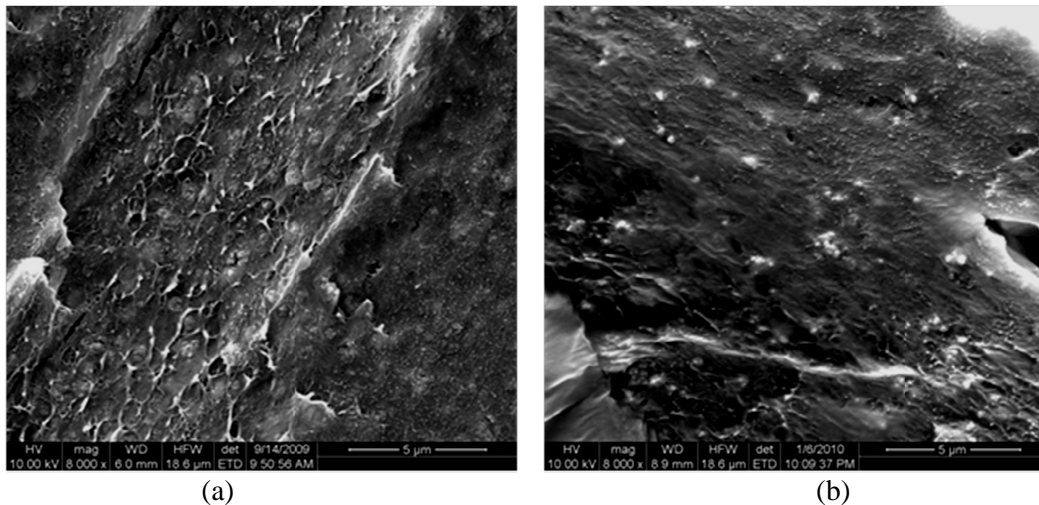


Figure III-1. Fracture SEM of non-treated TiO₂-PVDF composites with 4.6vol% (a) NS, scale 5 μm (b) MS, scale 5 μm (c) NR, scale 500nm (d) NW, scale 4 μm.

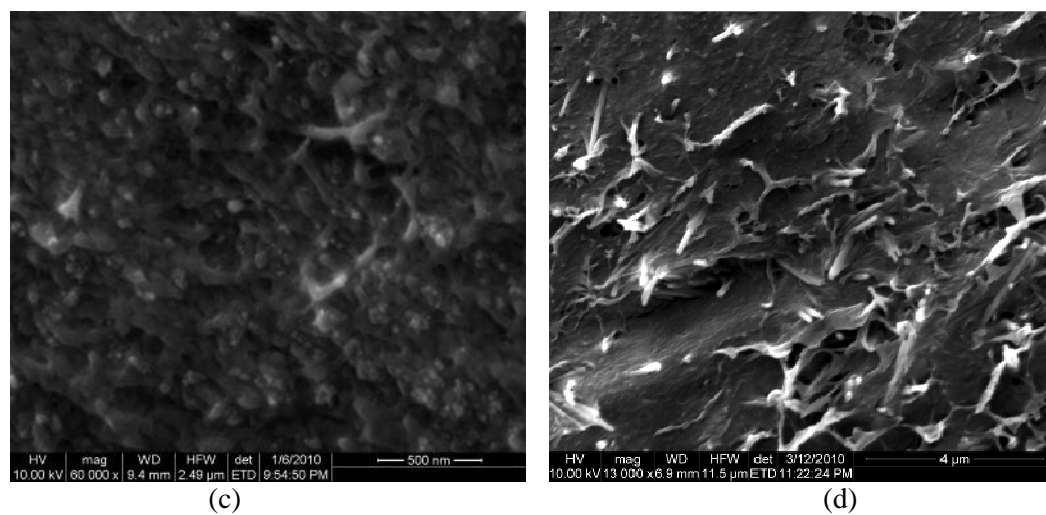


Figure II-3. Continued

(b) Fourier transform infrared (FTIR) spectroscopy

Figure III-2 shows FTIR spectra of pure PVDF and composites with TiO₂ NS, MS, NR and NW dried at room temperature. They show a dominance of the γ -phase, which is a polar phase; with the peaks at 812, 833 and 1233 cm⁻¹ being characteristic γ peaks as shown in Table II-2. These FTIR spectra show that any changes in the composites properties are not due to a phase change.

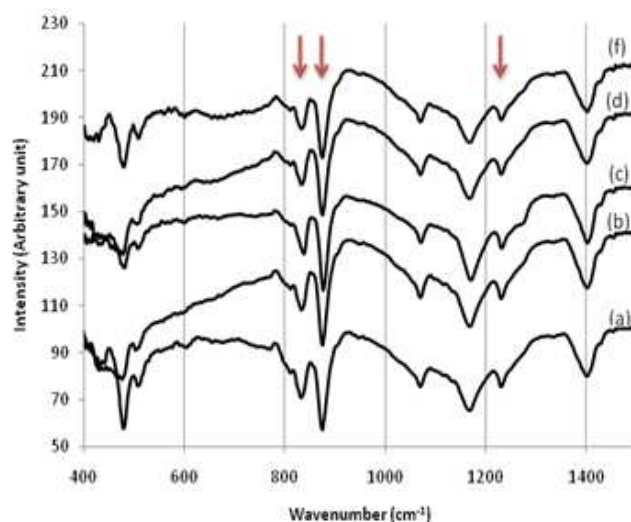


Figure III-2. ATR FTIR spectra of (a) pure PVDF and 4.6vol% TiO₂-PVDF with (b) NS (c) NR (d) MS and (d) NW dried at room temperature.

(c) Differential scanning calorimetry (DSC)

Table III-1 lists the degree of crystallinity of the different composites. The values shown in Table 1 are the average of three measurements with a standard deviation less than 3, which is in the range of the equipment's error. The degree of crystallinity of the TiO₂-PVDF composite with nano spheres (NS) is similar to the pure polymer. However in the other composites, there is an increase in the degree of crystallinity. With the addition of the inorganic particles, there might be a competition between nucleation sites creation and crystallization inhibition [93]. The particles may act like nucleation sites and tend to increase the crystallinity degree. At the same time, the particles can restrain the polymer chains movement particularly when their curvature is comparable to the polymer radius of gyration, inhibiting the crystallization process [94]. However there is

still no general conclusion on how the added particles would affect the degree of crystallinity of the polymer matrix [95].

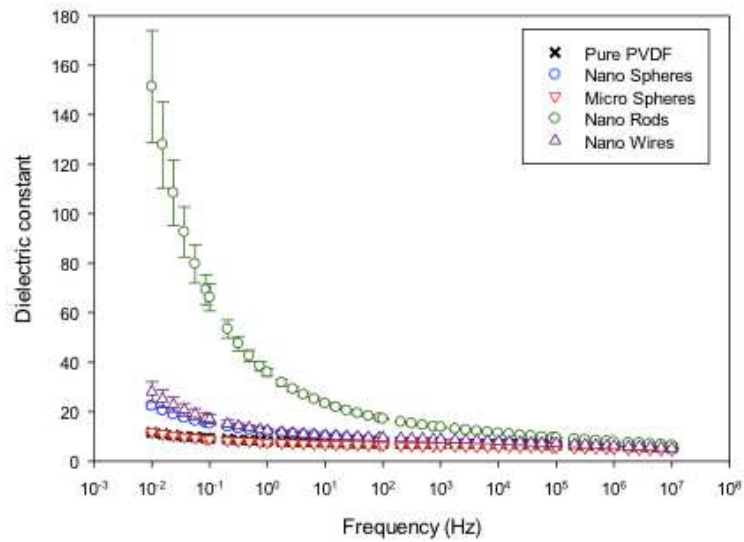
Table III-1. Degree of crystallinity of TiO₂-PVDF composites

	% Crystallinity
Pure PVDF	47±1.02
4.6vol% NS	47±1.13
4.6vol% NR	51±0.33
4.6vol% MS	54±2.90
4.6vol% NW	53±1.90

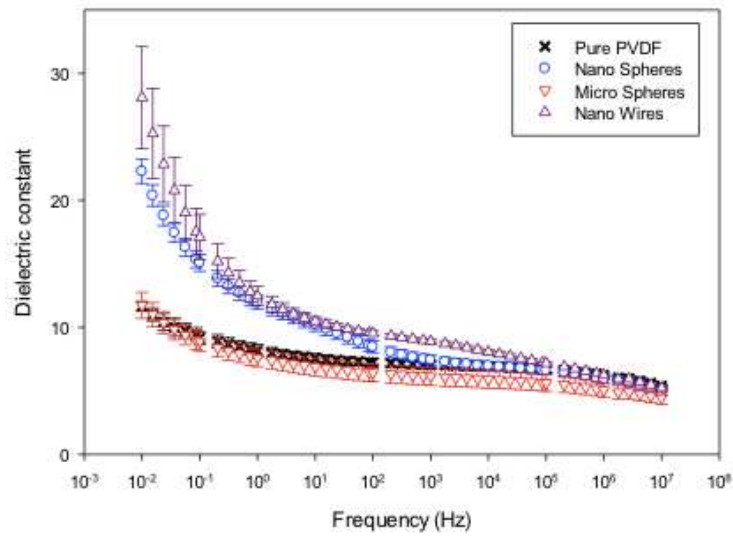
2. Low-field dielectric properties

Dielectric constant is influenced by polarization which is composed of atomic, electronic, dipolar and interfacial polarizations. As the applied AC electric field frequency increases, dipoles fail to follow the electric field, leading to a decrease in the dielectric material's polarization hence its dielectric constant decreases. For the polymer, as the frequency increases, it becomes harder for the C-F dipole to orient with the AC field. Moreover, the TiO₂ dielectric constant decreases with the increase in frequency leading to an overall decrease in the effective dielectric constant of the composites. [96] Figure III-3 compares the dielectric constant of the different 4.6vol% TiO₂-PVDF composites to the pure PVDF dielectric constant as a function of frequency. And Figure

III-4 compares the dielectric loss of the 4.6vol% TiO₂-PVDF composites to the pure polymer.



(a)



(b)

Figure III-3. (a) Dielectric constant of pure PVDF and 4.6vol% TiO₂-PVDF composites (b) excludes 4.6vol% NR-PVDF for clarity

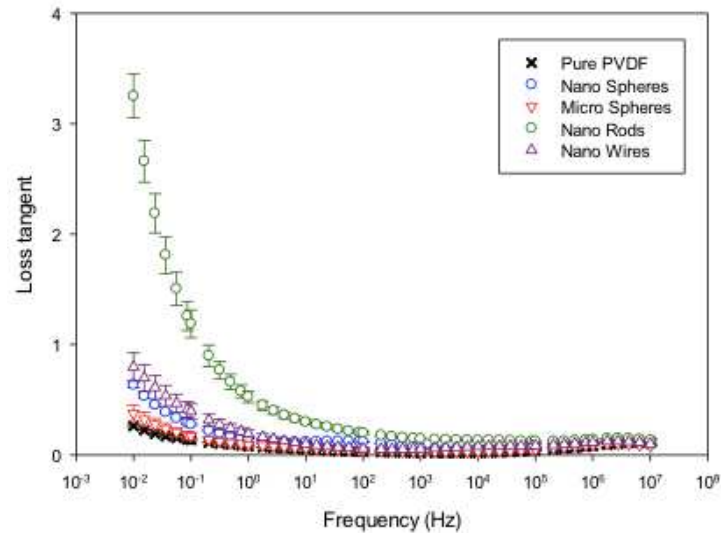


Figure III-4. Dielectric loss of pure PVDF and 4.6vol% TiO₂-PVDF composites

The nanocomposite made with the nano rods shows the highest dielectric constant and dielectric loss at low frequencies. The nano rods have the smallest diameter among all the particles and 4 times the aspect ratio of the spheres and the second highest surface area after the nano spheres. This indicates that the particles interfacial surface area and aspect ratio both play an important role in defining the dielectric behavior of the composite. The expansive interfacial surface area leads to a high interfacial polarization. On the other hand, the high aspect ratio enhances the local fields leading to an increase in the dielectric constant as well as the dielectric loss. In the case of nano spheres, although they have a higher interfacial surface area than the nano rods, their isotropic shape leads to lower enhancement in the local fields. At frequencies above 10kHz, all the composites' dielectric constants become close to the pure PVDF constant or even lower. This might be caused by the particles anchoring the polymer's chains and

inhibiting their movement at high frequencies. The dielectric loss follows the same trend as the dielectric constant; the composite with nano rods has the highest loss at low frequencies. This behavior confirms that the interfacial polarization is the dominant mechanism in the NR-PVDF composite at low frequencies [97].

Figure III-5 summarizes the size and aspect ratio effects on the dielectric constant of TiO₂-PVDF composites showing the highest improvement achieved with the NRs, then followed by NWs. In Figure III-5, the dielectric constants experimentally measured at 1Hz are compared to values (ϵ_{Eff}) calculated by Maxwell-Garnet model given by the following (III-1):

$$\epsilon_{\text{Eff}} = \epsilon_1 + \epsilon_1 \frac{\frac{c}{3} \sum_{j=x,y,z} \frac{\epsilon_2 - \epsilon_1}{\epsilon_1 + N_j(\epsilon_2 - \epsilon_1)}}{1 - \frac{c}{3} \sum_{j=x,y,z} \frac{N_j(\epsilon_2 - \epsilon_1)}{\epsilon_1 + N_j(\epsilon_2 - \epsilon_1)}} \quad (\text{III-1})$$

where ϵ_1 and ϵ_2 are the dielectric constants of the polymer matrix and the particles, respectively. c is the volume fraction of the particles, 0.046 in this case. To solve this equation, the pure polymer's dielectric constant at 1Hz is taken from the experimental measurements ($\epsilon_1=8.15$). For the nano and micro spheres, $\epsilon_2=70$ and for the nano rods and nano wires, the dielectric constant is $\epsilon_2=110$. The N_j factors are the depolarization factors. For spherical particles, $N_j=1/3$. For prolate spheroids (with $a_z > a_x = a_y$, a_x , a_y and a_z are semi-axes of an ellipsoid in the three orthogonal directions), N_x , N_y and N_z are given by (III-2) and (III-3).

$$N_z = \frac{1-e^2}{2e^3} \left(\text{Ln} \left(\frac{1+e}{1-e} \right) - 2e \right) \quad (\text{III-2})$$

$$N_x = N_y = \frac{1}{2}(1 - N_z) \quad (\text{III-3})$$

where the eccentricity is $e = \sqrt{1 - \frac{a_x^2}{a_z^2}}$

The highest difference between the experimental measurements and the model is for the case of nano rods composite. This is because the model do not account for the interfacial polarization. In reference [16], alumina nanoparticles (10-15nm diameter) added to a polyimide matrix resulted in an effective dielectric constant of 15 at 20vol% loading. The measured value exceeds the dielectric constant of both components in the composite. This was explained by interfacial polarization in the nanocomposite. The interphase effect was highlighted in reference [16] by using Vo-Shi model, [98], where an interphase around the nanoparticles is included in the model as a third phase with different properties than the particles and the matrix. However, in order to use this model, one should be able to estimate the interphase thickness and its properties. It is critical to account for the interphase effect in the effective medium models when the particles are in the nanoscale, hence the interfacial effects can no longer be negligible.

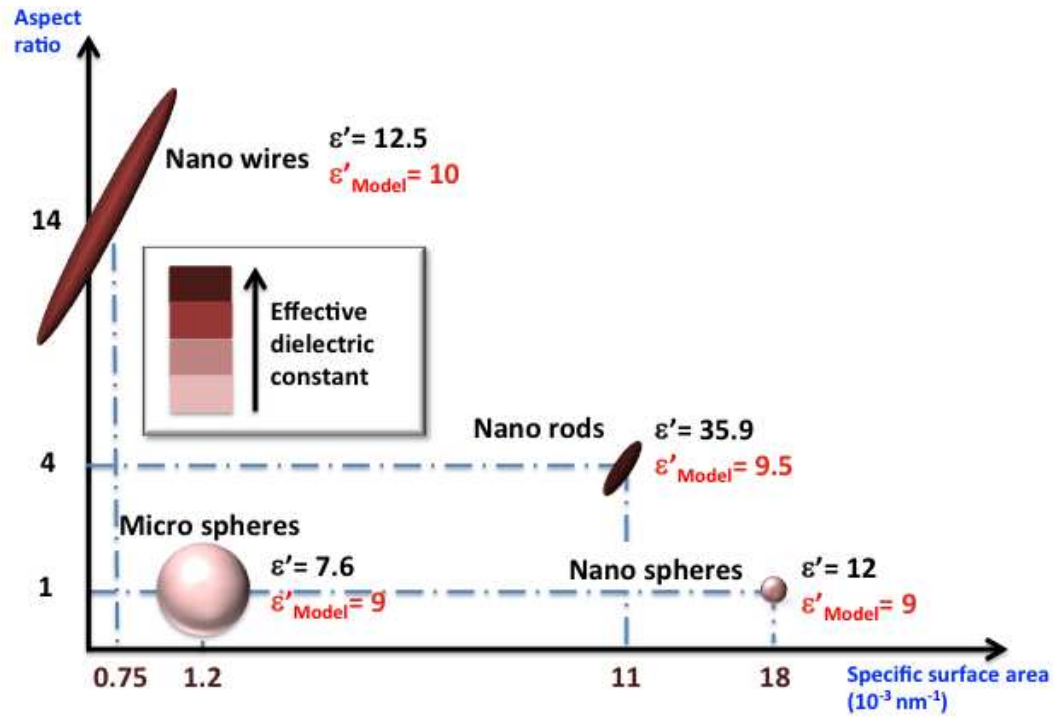


Figure III-5. Size and aspect ratio effects on TiO_2 -PVDF dielectric constant

3. High-field dielectric properties

Table III-2 summarizes the dielectric constant, DC breakdown electric field and electrical energy density of pure PVDF, and 4.6vol% TiO_2 -PVDF composites with the different particles. Under DC condition, energy density is calculated using (II-10). Figure III-6 shows the Weibull plot of the failure probability for all the composites compared to the pure PVDF. All the composites have a higher slope than the pure, showing a narrowed distribution and good homogeneity in the composites. All these composites have a dominance of the γ -phase. Among the different composites, the highest energy densities obtained are with the nano rod and nano wire TiO_2 particles.

This is because these two composites have higher dielectric constants than the composites with spherical particles.

Table III-2. DC Breakdown measurements for PVDF and 4.6vol% TiO₂-PVDF composites

Sample	Thickness (μm)	ϵ' @1kHz	$\tan(\delta)$ @1kHz	E_b (MV/m)	β	U (J/cc)
Pure PVDF	27±3	7	0.018	247	6.5	1.88
4.6vol% NS	27±3	7.4	0.066	177	11	1.03
4.6vol% MS	30±3	6.1	0.029	193	17	1.01
4.6vol% NR	29±3	13.7	0.145	159	26	1.53
4.6vol% NW	40±3	8.9	0.028	198	21	1.54

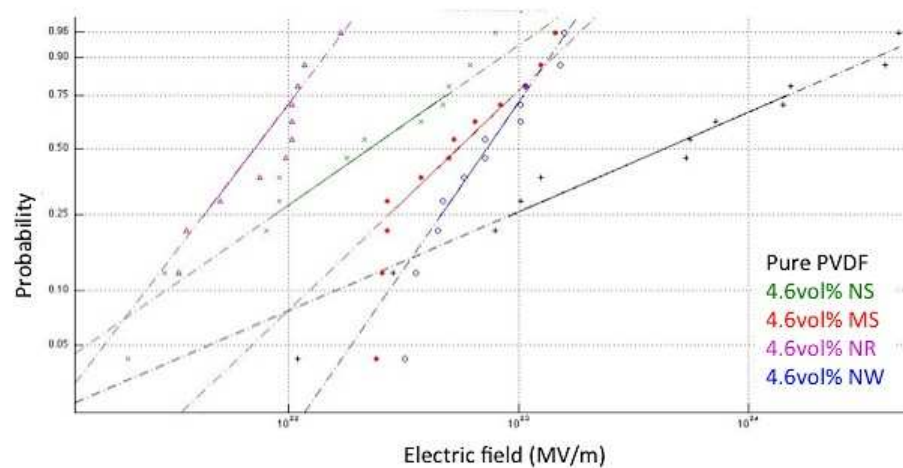


Figure III-6. Weibull plot for the different composites compared to the pure PVDF

There is a decrease in dielectric breakdown in all 4.6vol% TiO₂-PVDF composites; this might be due to the inherent lower dielectric breakdown of TiO₂ particles or defects created by the addition of the particles. However there is less

decrease in the breakdown in the composite with nano wires although these particles have a higher aspect ratio compared to nano rods and the spherical particles. In reference [22], it is stated that particles with higher aspect ratio induce higher local fields along their longitudinal axis when it is parallel to the applied electric field. With their long longitudinal axis ($1.6\mu\text{m}$) and high aspect ratio of 14, the nano wires prefer to have a planar 2D distribution due to the solution casting technique. The planar distribution reduces the local fields that are now along the nano wires transversal axis as shown in Figure III-7.

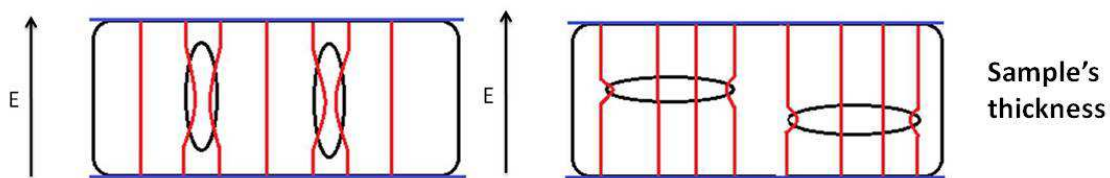


Figure III-7. Schematic of electric field distortion with the presence of aligned vs randomly dispersed NW

Under AC conditions, energy density is calculated using (II-11). Figure III-8 shows the electrical displacement at 50MV/m . In D-E loops, the higher slope is indicative of higher dielectric constant and the wider the hysteresis loop is associated with a higher loss in the sample. As shown in Figure III-8, the composite with nano rods has the highest dielectric constant and loss among all the composites, confirming the dielectric measurements.

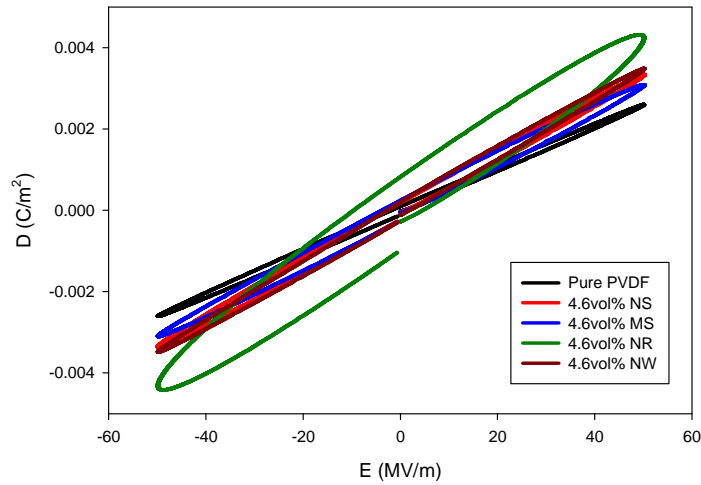


Figure III-8. D-E loops of 4.6vol% TiO₂-PVDF at 50MV/m 100Hz

Figure III-9 shows the electrical energy storage as a function of voltage for the different composites compared to the pure PVDF. The 4.6vol% composites with NS, MS and NR reach the dielectric breakdown at a lower field compared to the pure polymer. However the composite 4.6vol% NW-PVDF fails at the same range of electric field as the pure. The 4.6vol% composites follow the same trend in the AC breakdown measurements as well as the DC breakdown measurements: The composite with nano wires has the highest breakdown and energy density at breakdown as compared to the composites with nano rods and spherical particles.

Up to 127MV/m, 4.6vol% NR-PVDF has the highest energy density, but this high energy density is accompanied with the lowest efficiency among all composites as shown in Figure III-10. This low efficiency is associated with the high loss of 4.6vol% NR-PVDF composite. As shown in Figure III-10, the composite with nano wires have the highest efficiencies as compared to the other composites.

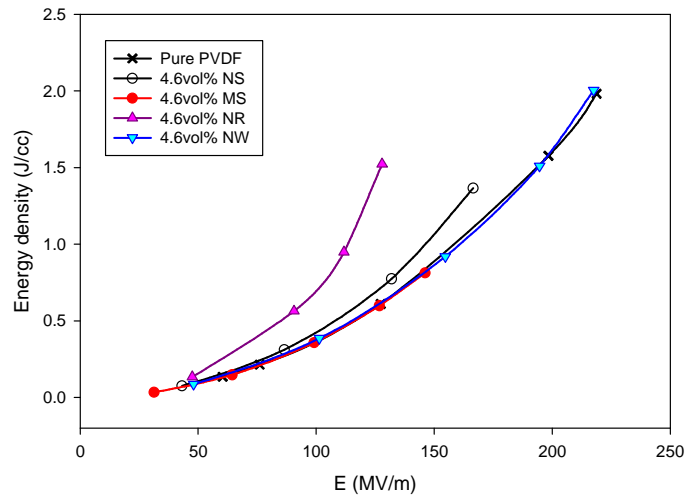


Figure III-9. Energy density of 4.6vol% TiO_2 -PVDF from D-E loops as a function of electric field

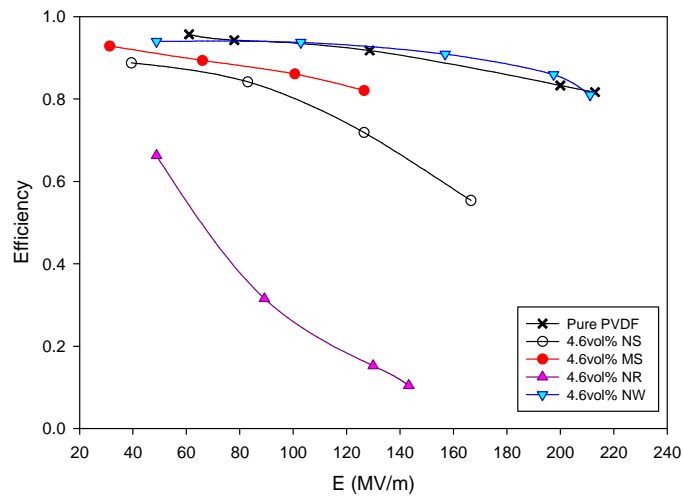


Figure III-10. Energy efficiency of 4.6vol% TiO_2 -PVDF from D-E loops as a function of electric field

CHAPTER IV

PARTICLES CONTENT, FUNCTIONALIZATION AND ORIENTATION EFFECTS ON DIELECTRIC PROPERTIES

The best results for dielectric constant and dielectric breakdown are measured for the nano wires (NW)-PVDF composite. With the NWs, local fields enhancement was limited due to the particles planar distribution leading to the least decrease in dielectric breakdown compared to the pristine polymer, while the dielectric constant increased and the loss was maintained. The decrease in the dielectric breakdown is mainly caused by the inherent breakdown of the inorganic particles. Therefore, the NWs are chemically treated and the content is varied in order to obtain an optimized performance, meaning the highest improvement in the energy density, based on content, orientation, and interaction. Three contents are tested: 2.3, 4.6 and 9.2vol%, corresponding to 5, 10 and 20 wt%, respectively. The composites were synthesized following the procedure detailed in Chapter II.2.

1. Particles and composites characterization

(a) Treated particles characterization using XPS

NWs were treated according to the method detailed in Chapter II.2. using APS, a silane-coupling agent. In order to verify that functionalization took place successfully on the surface of titania, XPS measurements were conducted on titania powder before and after functionalization. Figure IV-1 shows the XPS measurements of the as-received and

APS-treated TiO₂ nano wires. There is presence of Si and N atoms on the surface of the treated particles originating from the silane-coupling agent. About 2/3 of the nitrogen atoms are positively charged which most likely indicates that the N is able to have a strong non-covalent interaction with the fluorine atoms in PVDF as expected (Figure II-1). A more detailed XPS analysis is presented in Table IV-1 showing a decrease in the percentage of Ti and O after the particles treatment owing to covering the TiO₂ surface and the reaction with the silane-coupling agent, which is in agreement with what was mentioned in references [99, 100].

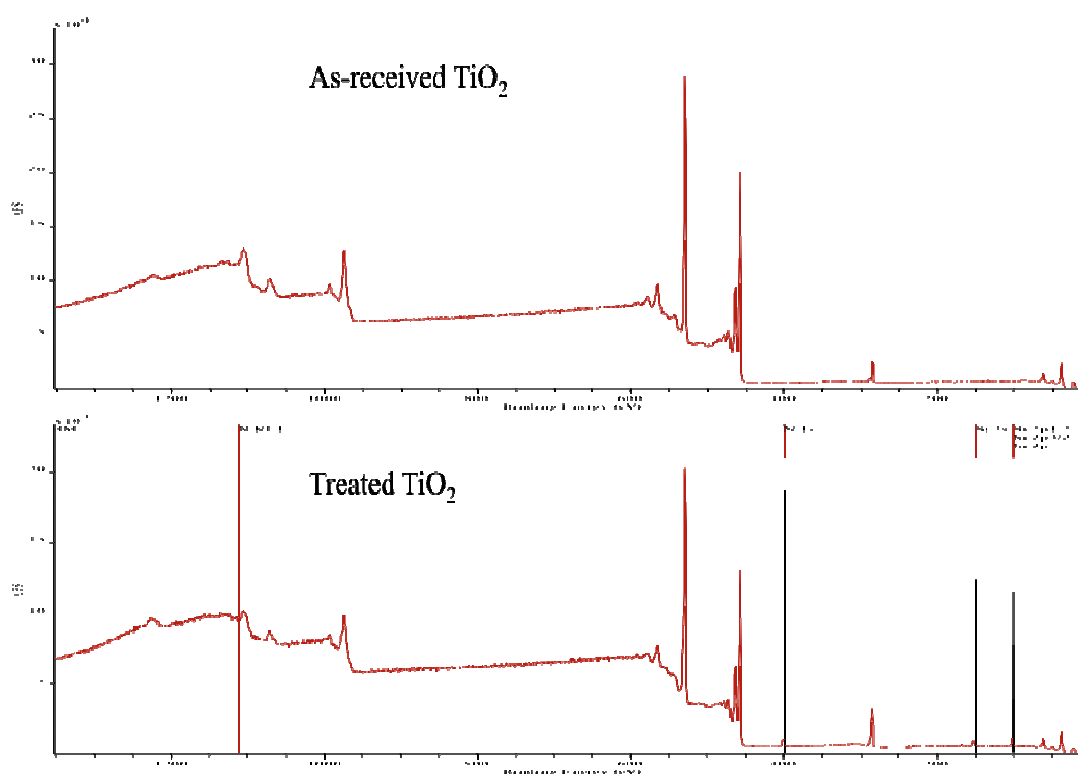


Figure IV-1. XPS measurements of as-received and APS-treated TiO₂ nano wires

Table IV-1. Analysis of XPS data; atomic percentage on the TiO₂ surface

	<u>Ti 2p</u>	<u>O 1s</u>	<u>C 1s</u>		
As received TiO ₂	23.7	61.0	15.3		
	<u>Ti 2p</u>	<u>O 1s</u>	<u>C 1s</u>	<u>Si 2p</u>	<u>N 1s</u>
Functionalized TiO ₂	15.7	49.8	27.4	4.0	3.2

(b) Effect of functionalization on particles dispersion and interaction with the polymer

Figure IV-2 displays the effect of TiO₂ nano wires (NW) functionalization on the dispersion and the interaction between the particles and the matrix. In Figure IV-2 (a), some voids surrounding the particles can be seen whereas in Figure IV-2 (b) the particles are embedded inside the polymer matrix showing a stronger interaction as a result of the particles functionalization. In the 2.3vol% NW-PVDF composite with as-received NWs, agglomerations can be seen in the cross-section SEM; whereas treated NWs are individually dispersed and have a planar distribution parallel to the film's surface. The planar distribution is due to the good dispersion of the particles combined with the solution casting technique used to make the composites films as mentioned in 2. . Figure IV-3 shows cross-sections of 4.6 and 9.2vol% F(NW)-PVDF composites. Both composites have good dispersion and strong interaction between the particles and the polymer matrix. However in the 9.2vol% composite, the NWs no longer have a clear 2D distribution. This can be due to the higher number of particles constraining each other's alignment during the solution casting at 9.2vol%.

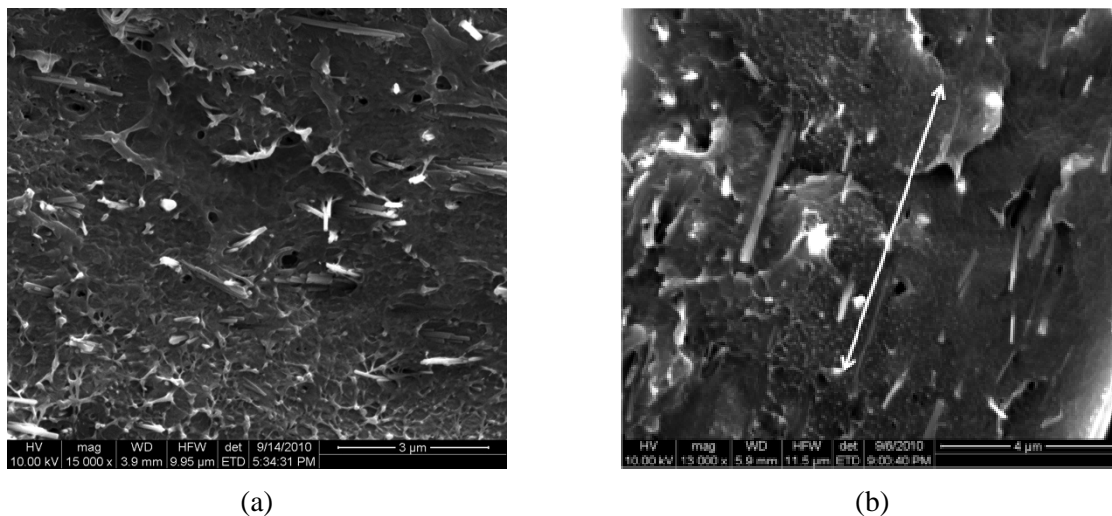


Figure IV-2. Effect of functionalization on TiO_2 NWs dispersion and interaction with PVDF (2.3vol% NW-PVDF) (a) Non-treated (b) Functionalized

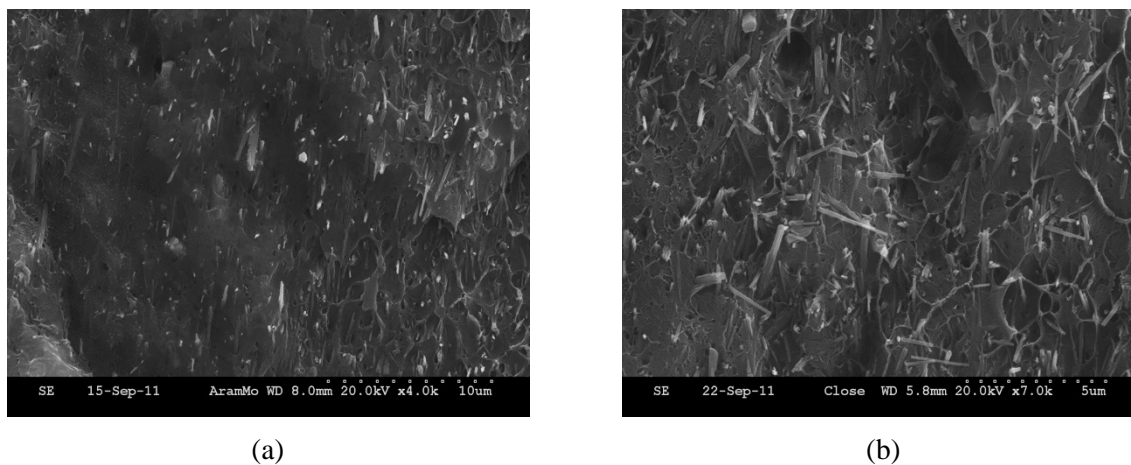


Figure IV-3. Cross-section SEM of (a) 4.6vol% F(NW)-PVDF and (b) 9.2vol% F(NW)-PVDF

For the 2.3 and 4.6vol% F(NW)-PVDF composites, Raman spectroscopy further proves that the particles not only have a planar distribution, but also have a preferred orientation which is parallel to the solution casting direction (0°). Figure IV-4 shows a schematic of how would the particles be distributed in a cross-section along the 0° and

90° directions, giving the (x,y) and (y,z) planes, respectively. Raman intensity was normalized with respect to a peak present at 876cm^{-1} that did not any dependence upon orientation of the sample. Figure IV-5 shows normalized Raman spectroscopy of cross-sections in the two 0° and 90° directions for 2.3, 4.6 and 9.2vol% composites. For 2.3 and 4.6vol% composites, the intensity of the Raman vibration at 612cm^{-1} is higher along the 0 direction, parallel to the casting direction. The Raman vibration at 612cm^{-1} corresponds to the vibration along the long axis of rutile TiO_2 [86]. However for the 9.2vol% composite, there is no difference in the vibrations intensity, which indicates a random distribution of the particles.

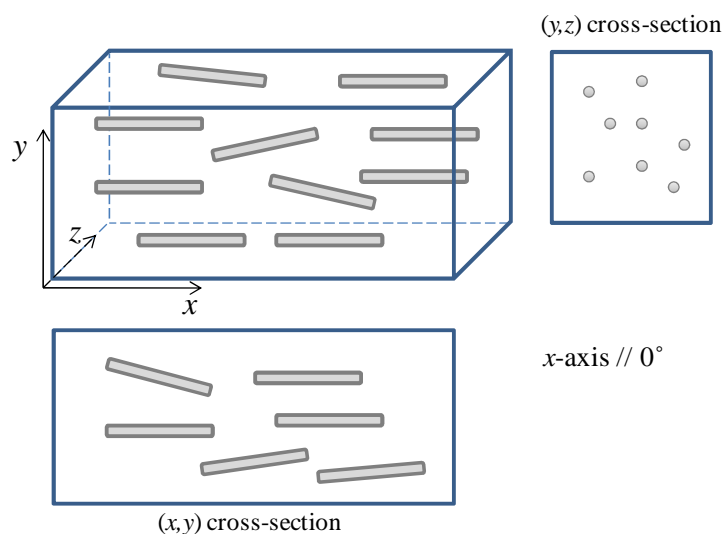
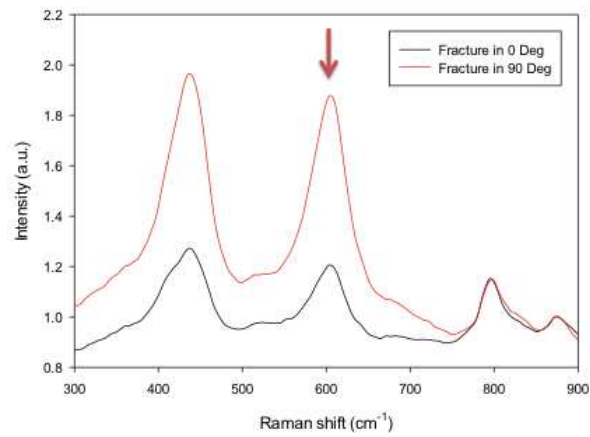
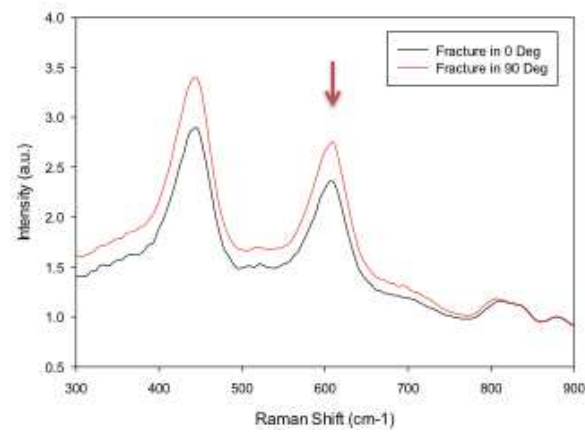


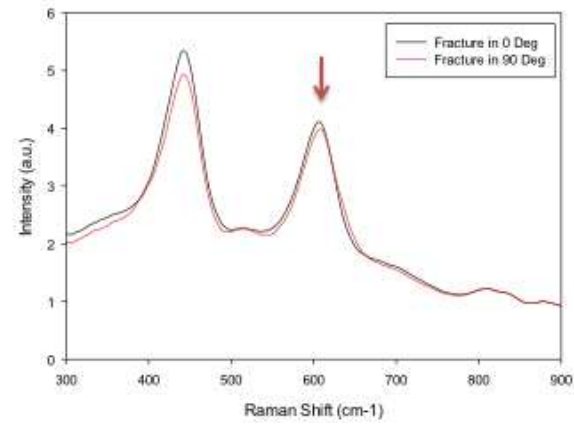
Figure IV-4. Schematic of the particles distribution in the composite the cross-sections when the fracture is in 0° Vs 90° directions



(a)



(b)



(c)

Figure IV-5. Normalized Raman spectroscopy of cross-sections of (a) 2.3vol% (b) 4.6 and (c) 9.2vol% F(NW)-PVDF

(c) Polymer phase investigation using FTIR

The particles functionalization does not seem to affect PVDF dominant phase. The pure PVDF has a dominance of γ -phase as indicated by the arrows in Figure IV-6. With the addition of the treated particles, the polymer phase does not seem to change. The main peaks for γ -phase are $812, 833$ and 1233cm^{-1} as it was mentioned in Chapter II.5.

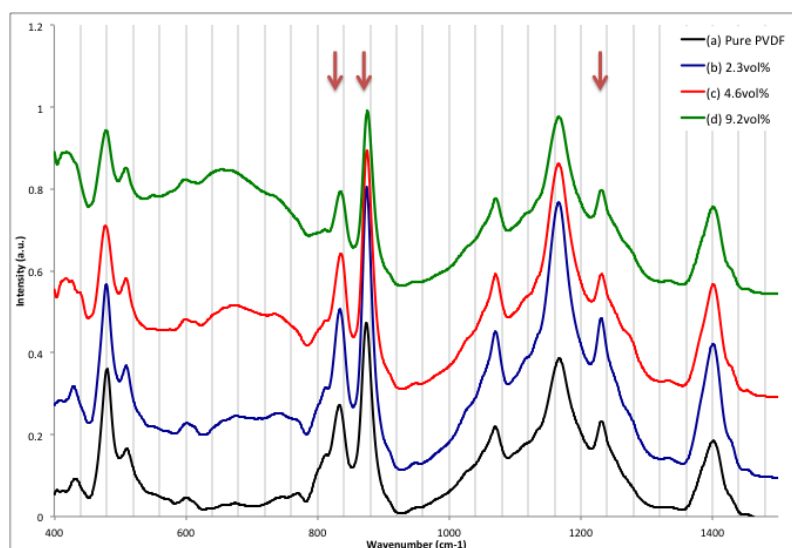


Figure IV-6. ATR FTIR spectra of (a) pure PVDF, (b) 2.3vol% (c) 4.6vol% and (d) 9.2vol% TiO_2 -PVDF with functionalized nano wires. The red arrows indicate γ peaks.

(d) Composites degree of crystallinity

Table IV-2 shows that the functionalization of TiO_2 particles did not drastically affect the degree of crystallinity of the PVDF polymer for the 2.3vol% NW-PVDF. The 2.3 and 4.6vol% nanocomposites have degrees of crystallinity comparable to that of pure PVDF. On the other hand, the 9.2vol% F(NW)-PVDF degree of crystallinity is the

lowest among all the composites with 35%, compared to 47% in the pure polymer. This might be due to an increase in the viscosity and the presence of more particles inhibiting the polymer chains from forming crystalline regions with the increase in the particles content [93].

Table IV-2. Degree of crystallinity of F(NW)-PVDF composites

	% Crystallinity
Pure PVDF	47±1.02
2.3vol% NW	45±1.90
2.3vol% F(NW)	46±2.70
4.6vol% F(NW)	47±2.68
9.2vol% F(NW)	35±2.21

2. Mechanical properties

The composites' mechanical properties were measured by tensile testing. Mechanical properties are important to make sure that an enhancement in the dielectric properties did not compromise the composites mechanical properties. Furthermore, mechanical testing is a good means to access the interaction strength between the particles and the polymer matrix. Figure IV-7 shows the Young's modulus measurements for the different NW-PVDF composites compared to the pure PVDF. Figure IV-7 also shows the lower and upper bounds modeled using Halpin-Tsai models for aligned wires. Halpin-Tsai model is a micromechanics model where the equations are written as [101]:

$$E_{U,L} = \frac{1+\xi\eta c}{1-\eta c} E_m \quad (\text{IV-1})$$

$$\eta = \frac{\frac{E_r}{E_m} - 1}{\frac{E_r}{E_m} + \xi} \quad (\text{IV-2})$$

$$\text{With } \xi = 2 \frac{L}{d} + 40c^{10} \quad \text{for } E_U$$

$$\text{And } \xi = 2 \frac{w}{d} + 40c^{10} \quad \text{for } E_L$$

where

- c Particles volume fraction.
- E_m Matrix Young's modulus, from experimental measurements.
- E_r Particles Young's modulus considered 230GPa [102, 103].
- E_U and E_L Upper and lower bounds, corresponding to the Young's modulus parallel and perpendicular to the particles, respectively.
- L Particle length, 1.6 μm .
- d and w Particles width and thickness, correspond to the diameter, 130nm.

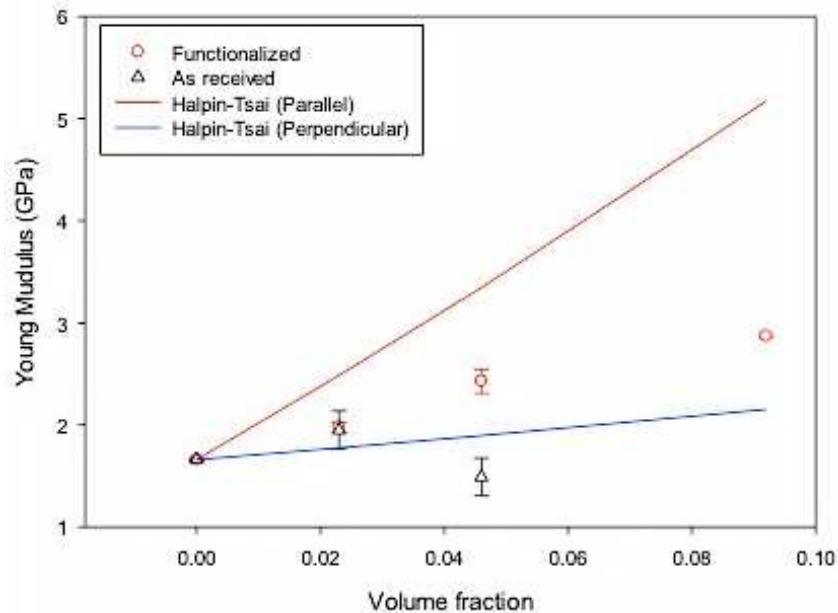


Figure IV-7. Young's modulus as a function of TiO₂ nano wires content

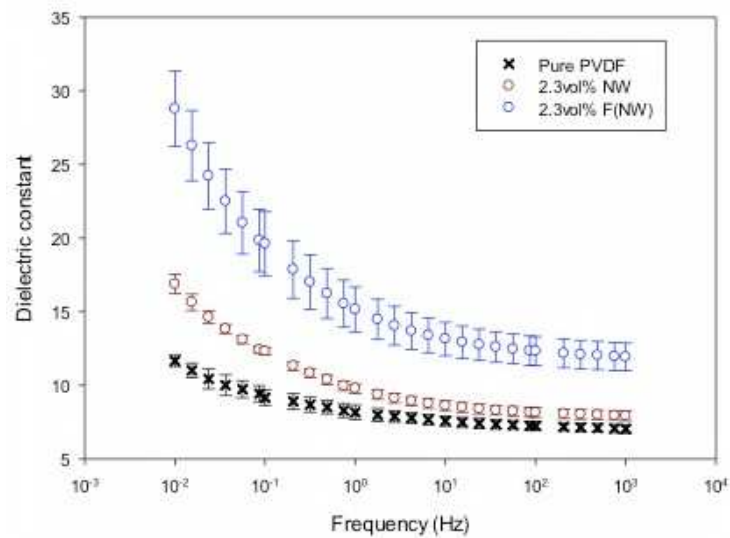
Pure PVDF has a measured Young's modulus of 1.66Gpa. At 2.3vol%, the Young's modulus increases for both as-received and treated nano wires (NW) to be around 2GPa. However at 4.6vol%, the as-received particles led to a decrease in the Young's modulus to 1.5GPa, which is lower than the modeled lower bound. This might be caused by particles agglomerations and weak interaction between the particles and the polymer. On the other hand, the functionalized particles led to a further increase in Young's modulus with 4.6 and 9.2 vol% loading indicating a strong interaction between the functionalized particles and the polymer. The measured Young's modulus of the composites with functionalized particles fall between the lower and upper bound calculated using the Halpin-Tsai model for aligned high aspect ratio particles. It is worth

indicating that the Young's modulus used in the model for TiO_2 is one of the highest values found in the literature.

3. Low-field dielectric properties

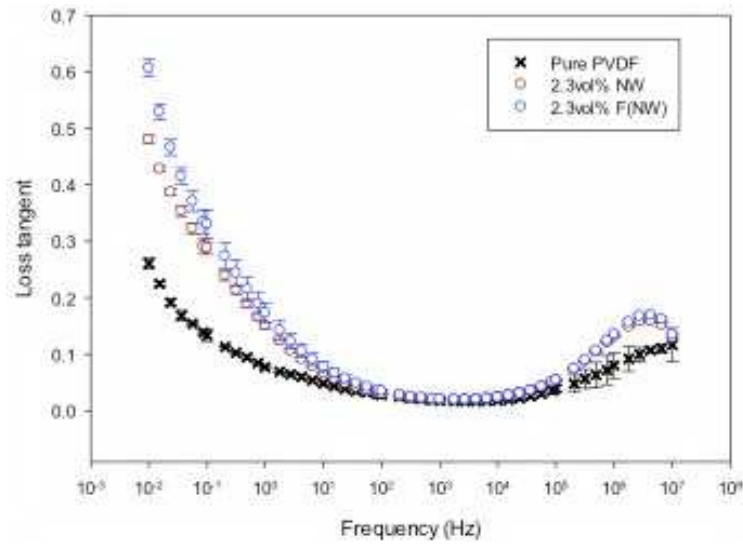
(a) Effect of functionalization

Figure IV-8 shows the effect of the functionalization on the dielectric properties of 2.3vol% NW-PVDF. There is an increase in the dielectric constant after the functionalization through all the frequencies range while the loss tangent remains in the same range.



(a)

Figure IV-8. (a) Dielectric constant and (b) loss tangent of pure PVDF and 2.3vol% treated and non-treated TiO_2 NW -PVDF composites



(b)
Figure IV-8. Continued

The experimental measurements of 2.3vol% F(NW)-PVDF dielectric constant were compared to Bruggeman models for aligned wires parallel and perpendicular to the applied electric field [104] as shown in Figure IV-9. The comparison with the classic model was limited to the range of frequencies 10mHz to 1kHz in order to remain in the quasi-static regime [105] The equations for the two models are written as:

$$\varepsilon_U = c\varepsilon_2 + (1 - c)\varepsilon_1 \quad (\text{IV-3})$$

$$1 - c = \frac{\varepsilon_2 - \varepsilon_L}{\varepsilon_2 - \varepsilon_1} \left(\frac{\varepsilon_1}{\varepsilon_L} \right)^{1/2} \quad (\text{IV-4})$$

where c is the volume fraction, 0.023 in this instance. ε_1 and ε_2 are the matrix and particles dielectric constants, respectively. And ε_L and ε_U are the effective dielectric constant for aligned wires perpendicular and parallel to the wires alignment,

respectively. ϵ_L and ϵ_U correspond to the lower and upper bounds for the modeled effective dielectric constant, respectively.

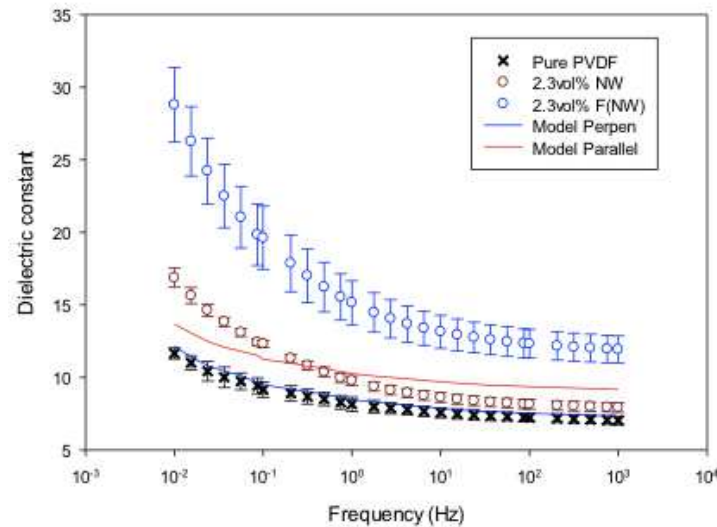


Figure IV-9. Comparison of the dielectric constant of 2.3vol% F(NW)-PVDF composite to Bruggeman models for aligned wires (Parallel and perpendicular to the particles alignment)

This comparison shows that the dielectric constant of the composite with as-received nano wires (NW) exceeds the upper bound at low frequencies, then it becomes between the lower and the upper bounds. However, the nanocomposite with functionalized particles has a dielectric constant higher than the upper bound predicted by the effective medium model at all frequencies. This indicates that the particles functionalization led to a significant interphase that increases the effective dielectric constant.

Figure IV-10 shows an increase in dielectric constant with the TiO_2 nano wires (NW) content. And Figure IV-11 shows the dielectric loss for the different composites

compared to the pure PVDF. At 2.3 and 4.6 vol% loading, the dielectric loss shows a slight increase compared to that of the pure PVDF. This indicates that the increase in the dielectric constant did not originate from the space charge related contribution. On the other hand, at 9.2 vol% NW, the dielectric loss changed behavior compared to pure PVDF, 2.3 and 4.6vol% composites. This can be related to an increase of space charge in the composite, and therefore an increase in the electrical conductivity at 9.2 vol% as shown in Figure IV-12. It can also be related to a possible particles percolation at 9.2 vol% content. At 9.2vol%, the TiO_2 particles inherent properties dominate the composite's effective properties.

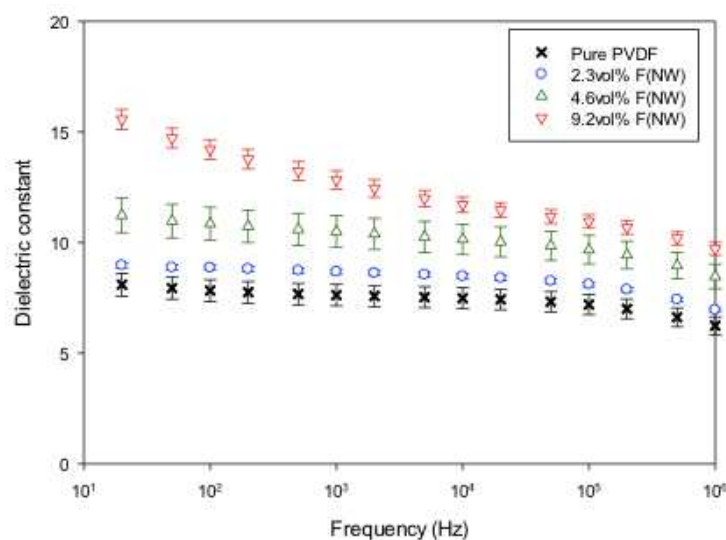


Figure IV-10. Dielectric constant of pure PVDF and 2.3, 4.6 and 9.2vol% treated TiO_2 NW - PVDF composites

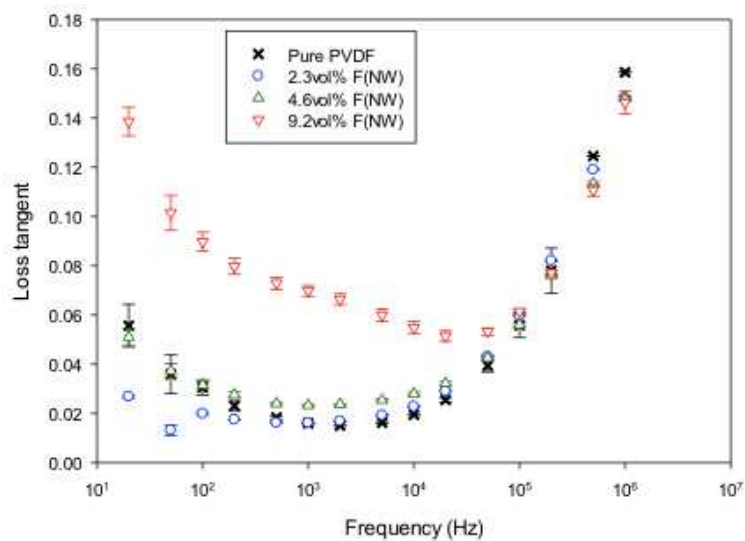


Figure IV-11. Dielectric loss of pure PVDF and 2.3, 4.6 and 9.2vol% treated TiO₂ NW -PVDF composites

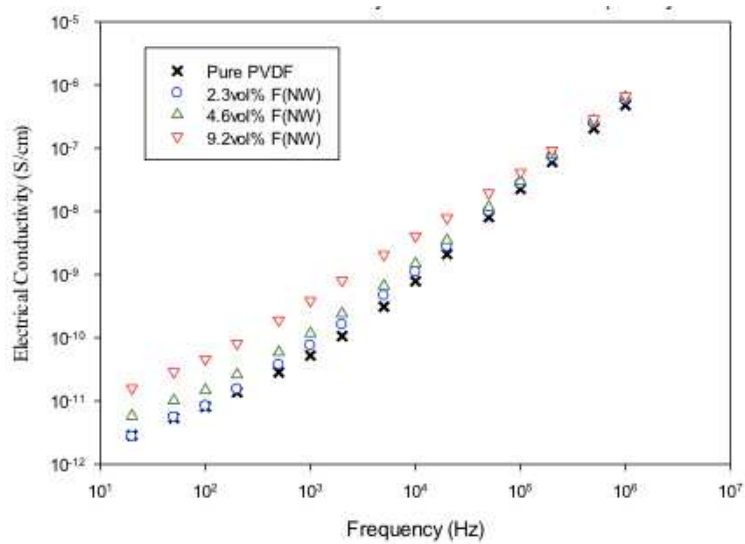


Figure IV-12. Electrical conductivity of pure PVDF and 2.3, 4.6 and 9.2vol% treated TiO₂ NW -PVDF composites

4. High-field dielectric properties

(a) DC breakdown

As shown in Table IV-3, the dielectric breakdown increases from 172 to 188MV/m when 2.3vol% NWs are added. Furthermore, it increases from 188 to 195MV/m when the NWs are functionalized. The dielectric breakdown increases with the TiO₂ content up to 4.6vol% reaching 328MV/m, and then it decreases at 9.2vol% to 147MV/m. The highest energy density is measured with the 4.6vol% F(NW)-PVDF composite with an improvement higher than 500% when compared to the pristine polymer from 0.94 to 5J/cc.

Table IV-3. DC Breakdown measurements for PVDF and NW TiO₂-PVDF composites

Sample	Thickness (μm)	ϵ' @1kHz	$\tan(\delta)$ @1kHz	E_b (MV/m)	β	U (J/cc)
Pure PVDF	22 \pm 3	7.2	0.018	172	9	0.94
2.3vol% NW	28 \pm 3	8.8	0.021	188	7	1.37
2.3vol% F(NW)	25 \pm 2	9.0	0.020	195	8	1.51
4.6vol% F(NW)	19 \pm 2	10.5	0.023	328	4	5.00
9.2vol% F(NW)	19 \pm 2	12.8	0.069	147	4	1.22

Figure IV-2 and Figure IV-3 show that the 2.3vol% F(NW)-PVDF has the best dispersion among the composites with treated particles. At 4.6vol% content, there is an optimum correlation between dispersion, planar distribution and electrons scattering resulting in the highest dielectric breakdown. At 9.2vol% content, the particles inherent

dielectric breakdown along with a smaller inter-particles distance result in a decrease in the composite's dielectric breakdown. The 9.2vol% composite has the highest dielectric loss, which is inter-related with the electrical conductivity, σ , by (IV-5), where σ_s is the static conductivity [106, 107].

$$\sigma = \sigma_s + \omega \epsilon \epsilon_0 \tan(\delta) \quad (\text{IV-5})$$

An increase in the dielectric loss and electrical conductivity leads to the decrease in the dielectric breakdown of 9.2vol% composite as shown in Figure IV-13. This is because higher charge density in the system leads to a lower dielectric breakdown [108].

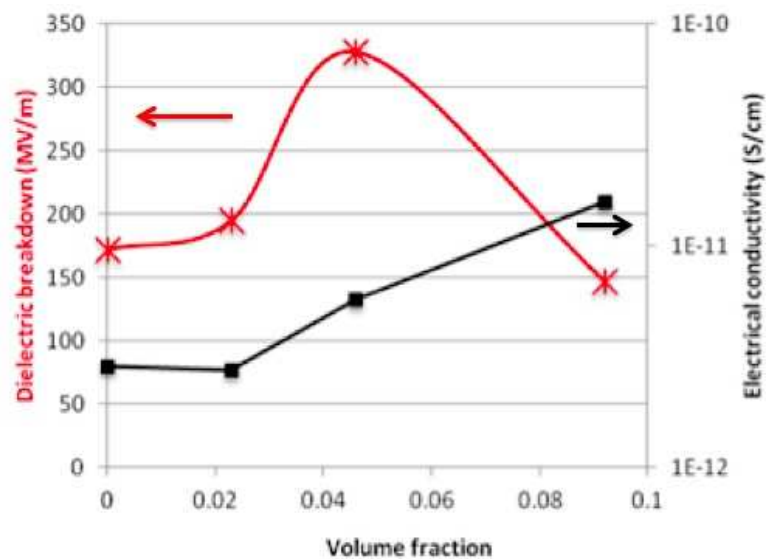


Figure IV-13. Dielectric breakdown and electrical conductivity at 20Hz as a function of particles content

For the 9.2vol% F(NW)-PVDF composite, the decrease in the dielectric breakdown and increase in the electrical conductivity can be associated with the “easier” electrons transport through the sample as compared to the composites with lower content; in other words, a percolation-like behavior. If we assume the nano wires still have a planar distribution in the 9.2vol% composite, one could consider the cross-section of a composite to be visualized as a distribution of disks, a disk being the cross-section of one nano wire. Under this assumption, circular cross-sections of the 2.3, 4.6 and 9.2vol% composites can be represented as in Figure IV-14 assuming a normal random distribution of the nano wires (65nm radius) in a 1micron-radius disk. This schematic do not account for an interphase around the particles. The addition of a 3-layer interphase similar to the interphase proposed by Tanaka, [58], a contact and/or overlap between the NWs in the 9.2vol% composite would have a higher probability. On the other hand, as shown by the SEM micrographs, the nano wires no longer have a clear planar distribution for the 9.2vol% F(NW)-PVDF composite, which would lead to a higher probability of contact between the particles, leading to more paths for the electrons to travel through the sample thickness. On the other hand, in the 4.6vol% composite, most probably the interphases around the particles would not overlap, leading to trapping of the mobile carriers rather than transferring them. The charges behavior in the composites would be examined by TSC and activation energy in Chapter IV5. to confirm the aforementioned observations.

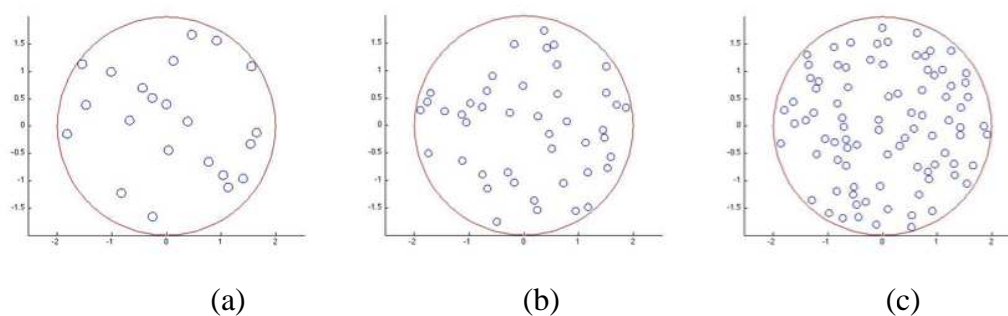


Figure IV-14. Schematic of nano wires distribution in (a) 2.3, (b) 4.6 and (c) 9.2vol%

(b) AC breakdown

Under AC conditions, the 2.3vol% NW-PVDF with treated particles has the highest energy density, 2.14J/cc, as compared to the other composites and the pure PVDF as shown in Figure IV-15.

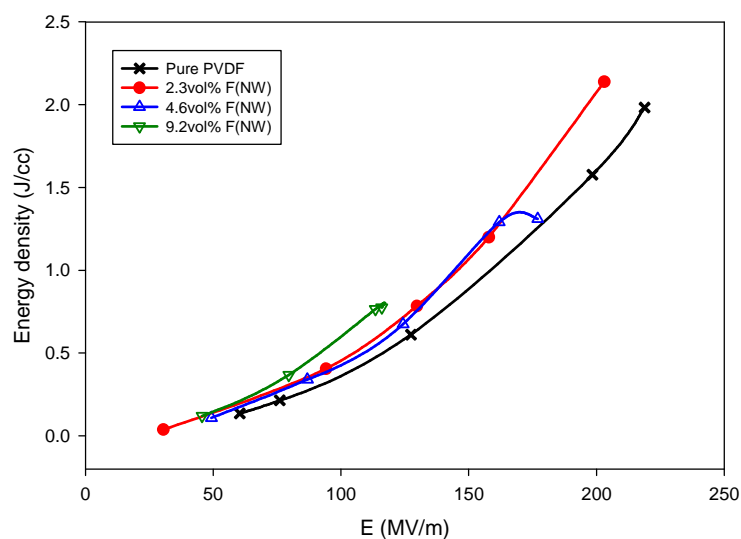


Figure IV-15. Energy density of F(NW) TiO₂-PVDF from D-E loops as a function of electric field

As the F(NW) content increases, the AC breakdown decreases although the energy density in all the composites are higher than that of the pure polymer before the breakdown occurs. Under AC conditions, the failure happens faster if the polymer chains and dipoles cannot follow the electric field; which can explain why the composites have a lower breakdown than the pure PVDF under AC conditions. It is possible that TiO_2 particles decelerate the polymer chains when they try to follow the electric field, which may initiate the dielectric breakdown at a certain electric field. Furthermore, the addition of the TiO_2 nanoparticles increases the number of dipoles present in the system, leading to a lower dielectric breakdown under AC conditions.

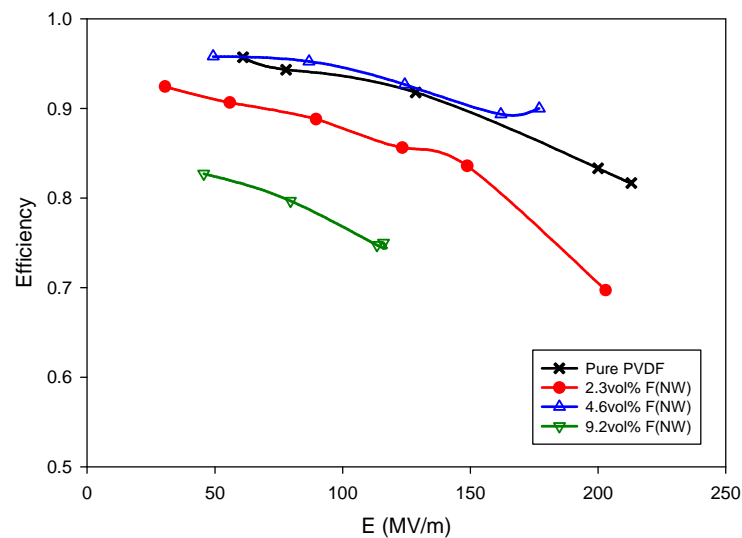


Figure IV-16. Energy efficiency of F(NW) TiO_2 -PVDF from D-E loops as a function of electric field

Figure IV-16 shows the efficiency of the composites with treated particles; the 4.6vol% F(NW)-PVDF composite has the highest efficiency although it fails before the

pure and the 2.3vol% F(NW)-PVDF composite. The efficiency follows a different trend compared to the energy density. This may be related to the 4.6vol% F(NW)-PVDF film having less defects than the 2.3vol% F(NW)-PVDF composite due probably to processing. The presence of a fewer number of defects in the system, reduces the losses therefore increase the efficiency.

5. Internal charges behavior

In addition to the particles distribution enhancement due to the functionalization, the interaction between the particles and the polymer matrix becomes stronger which creates deeper charge traps. The activation energy relates to the electrons transport; the depth of the traps present in the system. The composites activation energy was calculated using dielectric spectroscopy by investigating the relaxation frequency shift when the temperature increases [90, 109-111]. Relaxation frequency for the different temperature are obtained from the loss tangent dependence on temperature and frequency. The dielectric loss used for each composite is the average of three samples. Temperature dependence of the relaxation time follows the Arrhenius equation:

$$\tau(T) = \tau_0 \exp\left\{\frac{E_a}{k \cdot T}\right\} \quad (\text{IV-6})$$

where τ is the relaxation time (inverse of the relaxation frequency), τ_0 is the reciprocal frequency factor, k is Boltzmann constant, T is the temperature in Kelvin and E_a is the activation energy. Applying the natural logarithm (Ln) on (IV-6), we get:

$$\text{Ln}(\tau) = \frac{E_a}{k \cdot T} + \text{Ln}(\tau_0) \quad (\text{IV-7})$$

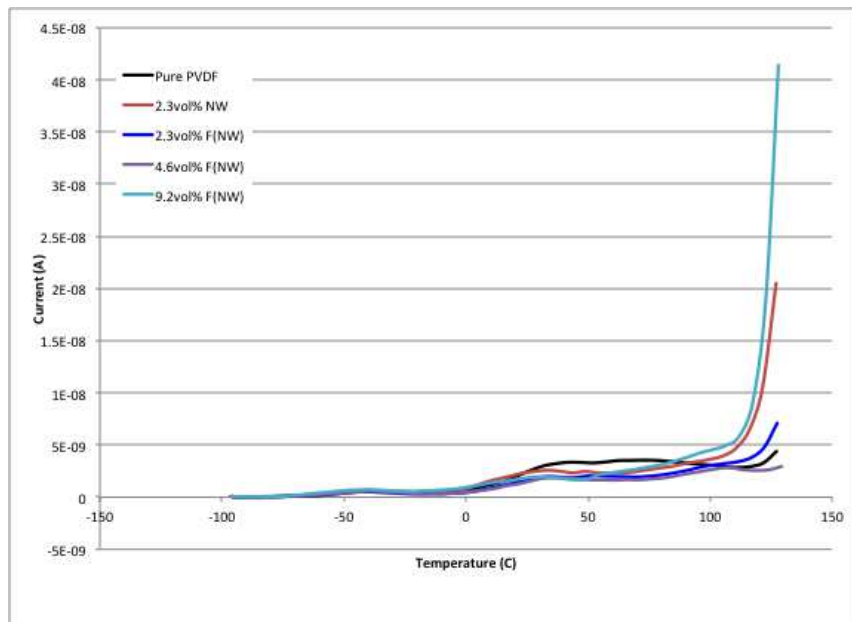
And the activation energy is obtained by linearly fitting $\ln(\tau)$ as a function of $1/T$.

Table IV-4 shows a slight decrease of activation energy from 1.03 to 0.99eV when the as-received NWs are added. This might be due to a weak interaction between the particles and the polymer. On the other hand, there is an increase of the activation energy from 0.99 to 1.19eV when the nano wires (NW) are functionalized at the 2.3vol% composite. This indicates that the particles functionalization resulted in a stronger interaction between the particles and the polymer matrix, creating deeper trapping sites at the interphase [2]. Furthermore, the activation energy increases with the content of F(NWs) up to 4.6vol% to reach 1.35eV, then it decreases at 9.2vol% to 1.05eV. This trend coincides with the dielectric breakdown measurements and shows deeper traps in the case of 4.6vol% composite breakdown hence less electrons mobility. Deeper traps in the system leads to a higher electric field required to create a path for the electrons and therefore create the insulating-conductive transition, reaching the dielectric breakdown.

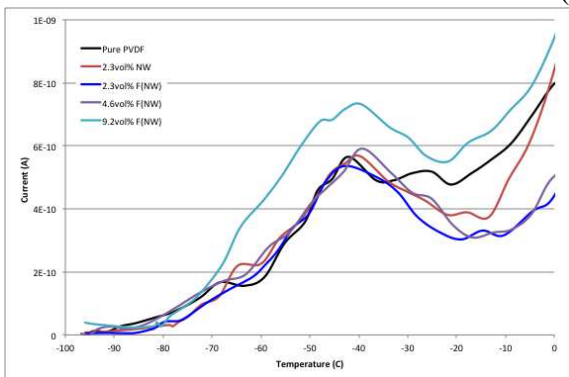
Table IV-4. Activation energy calculated from dielectric spectroscopy

Activation energy (eV)	
Pure PVDF	1.03
2.3vol% NW	0.99
2.3vol% F(NW)	1.19
4.6vol% F(NW)	1.35
9.2vol% F(NW)	1.05

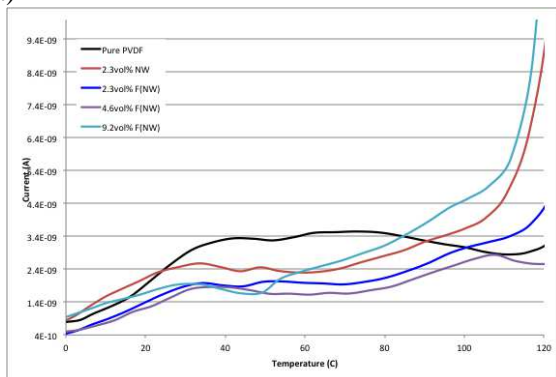
To further study the charges behavior in the composites, thermally stimulated currents (TSC) measurements are carried out. TSC is a powerful tool to study dipoles and space charges relaxations [89]. Figure IV-17(a) shows the current released of the samples over the range of temperature -100°C to 130°C .



(a)



(b)



(c)

Figure IV-17. TSC measurements (a) for all the temperatures range (b) Around T_g and (c) at higher temperatures

TSC measurements show the dipolar relaxations in the amorphous region corresponding to the glass-rubber transition for all the composites (around -40°C) as shown in Figure IV-17(b). The 9.2vol% F(NW)-PVDF composite has the highest peak. This can be associated with the lowest degree of crystallinity measured for the 9.2vol% composite as shown in Table IV-2, therefore the presence of more dipoles in the amorphous regions as compared to all the other samples.

Another broad peak appears at higher temperatures, between 30 and 90°C as shown in Figure IV-17(c). This broad peak involves a distribution of polarizations, and corresponds to dipolar relaxations and space charges in the crystalline regions along with the charges accumulated at the boundaries between amorphous and crystalline regions [89, 91]. The three composites have a different behavior when compared to the pure PVDF at the higher temperatures. The pure PVDF has a higher peak expanded over a broader range. When comparing the different composites behavior at the temperature range of 30°C to 100°C , it appears that the 2.3vol% F(NW) has a lower peak when compared to 2.3vol% NW-PVDF. This can be related to deeper charges traps as a result of the particles functionalization. The 4.6vol% F(NW)-PVDF composite has a slightly lower peak than the 2.3vol% F(NW). On the other hand, the 9.2vol% F(NW)-PVDF composite has a narrower peak than all the other composites; the current starts the runaway around 50°C . The 9.2vol% current runaway at a lower temperature can be related to the higher electrical conductivity of the 9.2vol% F(NW)-PVDF composite, requiring less energy for the electrons to travel through the sample.

The current decreases around 100°C for the pure PVDF, however it increases again for the 2.3vol% NW-PVDF, 2.3vol% F(NW)-PVDF and 9.2vol% F(NW)-PVDF composites which indicates a spontaneous conduction for these composites at higher temperatures. On the other hand, the 4.6vol% F(NW)-PVDF composite has a behavior closer to that of the pure PVDF rather than the other NW-PVDF composites (2.3vol% as-received, functionalized and 9.2vol% functionalized TiO₂ nano wires). The lower levels of current released in the 4.6vol%F(NW)-PVDF compared to the other composites correlates with dielectric breakdown and activation energy calculations; the 4.6vol% F(NW)-PVDF composite has the deepest traps compared to the pure PVDF and the other composites.

For repeatability, another series of samples were characterized using TSC to insure the same behavior is followed in the different samples of the same composite. Averaging the output current is not feasible since the input temperature is different for each measurement. Although the difference is not dramatic, averaging x and y-data might cause the loss of some information. Some sample comparison is show in Appendix A.

6. Breakdown mechanisms

Figure IV-18 shows the thickness dependence of pure PVDF, 2.3 and 4.6vol% F(NW)-PVDF composites. For the three films, the breakdown decreases when the thickness increases because more defects are present in the system; which is in agreement with the literature [51, 53, 112, 113]. The highest dependence on the thickness is observed with the 4.6vol% F(NW)-PVDF composite. When the particles

content increases, there is a higher chance that the defects number would increase due to possibility of creation of nanovoids around the particles [51]. This explains the higher dependence to the thickness seen with the 4.6vol% when compared to the pure PVDF and the 2.3vol% composite. At the lowest thickness, 19 μm , it has the highest dielectric breakdown, 328MV/m, among all the systems. This might be due to the high aspect ratio particles having a ‘close-to-perfect’ planar distribution with such a thin sample. In this case, there might be a combination of electrons scattering and trapping, therefore preventing the mobile carriers from creating a conducting path in an almost defect-free system.

When carrying out the dielectric measurements, a hole with diameter around 100 μm can be seen at some instances. It was noticed that these holes appear very rarely in the case of pure PVDF, however they are relatively more probable in the composites. This can be an indication of thermal breakdown causing the melting of the polymer in the area where the breakdown is happening as shown in Figure IV-19. When a critical electrical field is reached, thermal runaway takes place saturating the dissipated power and causing the temperature to increase drastically, creating a plasma channel.

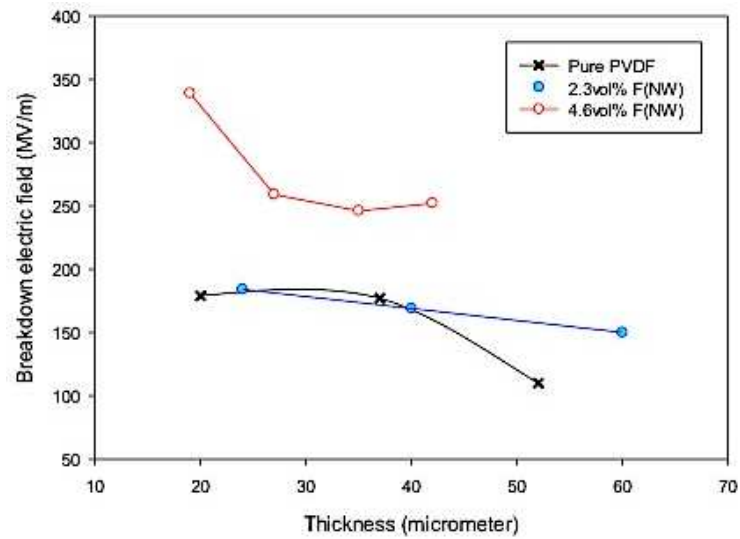


Figure IV-18. Thickness dependence of breakdown electric field

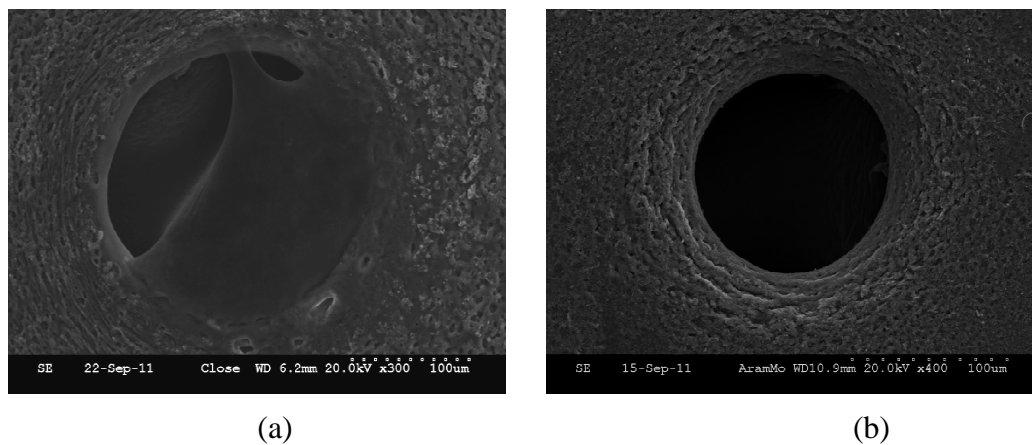


Figure IV-19. SEM of a hole caused by breakdown on a (a) pure PVDF sample and (b) 4.6vol% F(NW)-PVDF sample

The catastrophic failure happens very fast, most probably initiated by defects and mainly driven by electronic and thermal mechanisms. More studies should be carried out in order to fully characterize the complex mechanism of dielectric breakdown in the polymer composites.

CHAPTER V

THREE-PHASE COMPOSITE STUDY

1. Dispersion study

SEM imaging shows a uniform dispersion of TiO₂ nano wires. However the silver particles were not easily detected. As shown in Figure V-1(b), there are spherical particles that were imaged. Nevertheless, Energy-Dispersive X-ray Spectroscopy (EDS) did not confirm they are silver particles as shown in Figure V-2. This might be because of the low resolution of the EDS (500nm), while the particles size is lower than 500nm.

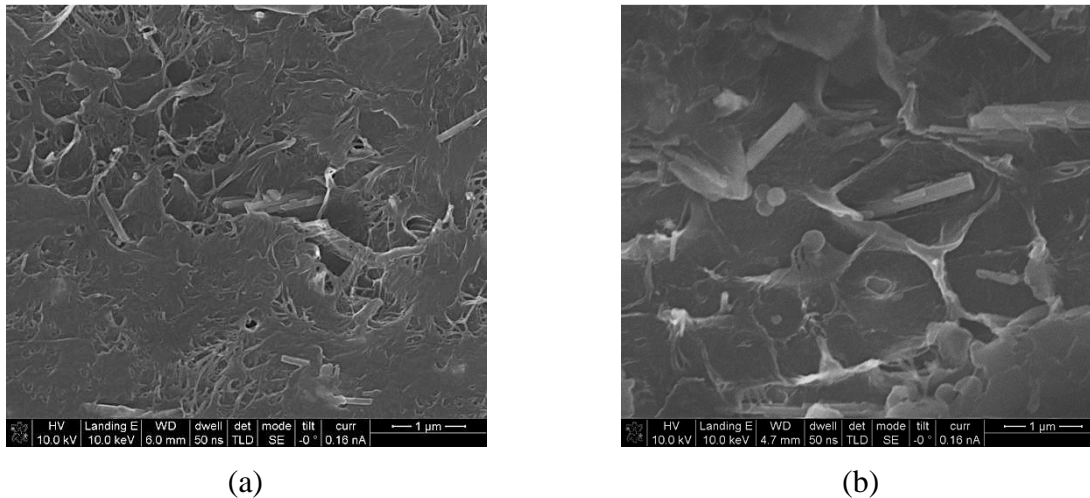


Figure V-1. SEM images of 3wt% F(NW)-0.5wt% Ag-PVDF with (a) Ag ex-situ and (b) Ag in-situ

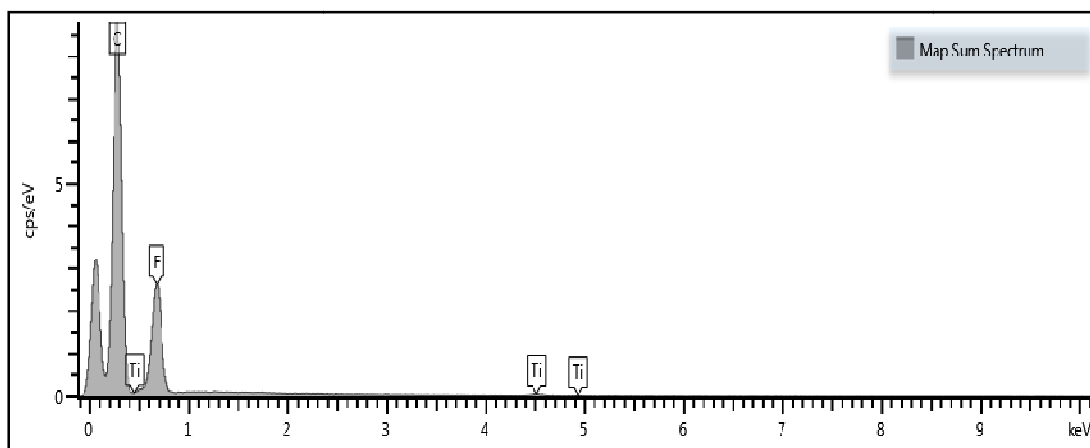


Figure V-2. EDS of 3wt% F(NW)-0.5wt% Ag-PVDF (in-situ) shown in Figure V-1(b)

Figure V-3 shows TEM images of the three-phase composites with in-situ and ex-situ Ag nanoparticles. A uniform dispersion is confirmed with these TEMs. The ex-situ particles have a diameter of 6nm and the in-situ particles size ranges from 5 to 15nm. Furthermore, it can be observed in Figure V-3 (b) and (d) that the Ag nanoparticles tend to gather around the NW particles.

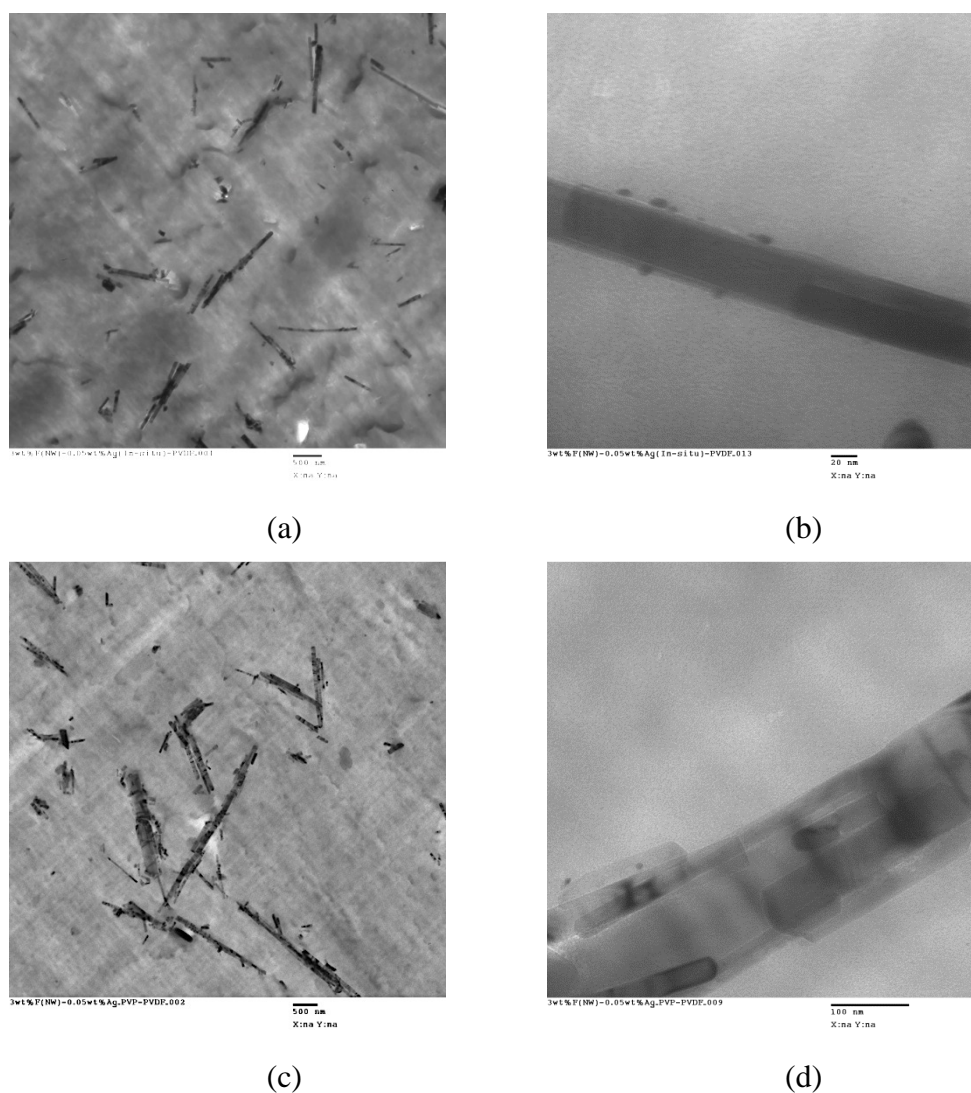


Figure V-3. TEM images of 3wt% F(NW)-0.5wt% Ag-PVDF (a) and (b) Ag in-situ; (c) and (d) Ag ex-situ

2. Composites phase using FTIR

As it is important to check on PVDF's phase in the nanocomposites, FTIR results show that the addition of the silver particles, ex-situ and in-situ did not change the dominant phase, which remains gamma as shown in Figure V-4.

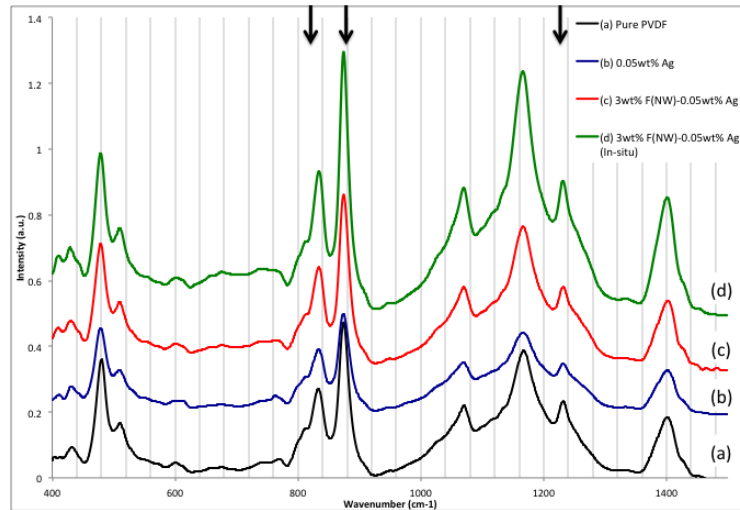


Figure V-4. FTIR spectra of F(NW)-Ag-PVDF composites compared to the pure PVDF

3. Degree of crystallinity properties using DSC

The degree of crystallinity remained in the same range compared to the pure PVDF with the addition of TiO_2 nano wires (NW) and Ag separately. However in the three-phase composites, the degree of crystallinity increased compared to the two-phase composites and the pure PVDF. This might be related to a dispersion challenge in the three-phase composites. It is easier to disperse the particles in a two-phase composite, which leads to more nanoparticles inhibiting the polymer chains from forming crystalline regions. However, in the case of the three-phase composite, the polymer chains face less restraining from the particles agglomerations.

Table V-1. Degree of crystallinity of the two- and three-phase composites compared to PVDF

	% Crystallinity
Pure PVDF	47±1.02
0.05wt% Ag	47±2.15
3wt% F(NW)	45±1.85
3wt% F(NW)-0.05wt% Ag	50±2.83
3wt% F(NW)-0.05wt% Ag (In-situ)	55±3.08

4. Electrical properties study

(a) Dielectric spectroscopy

The two- and three-phase composites have a dielectric constant slightly lower than the pure PVDF as shown in Figure V-5.

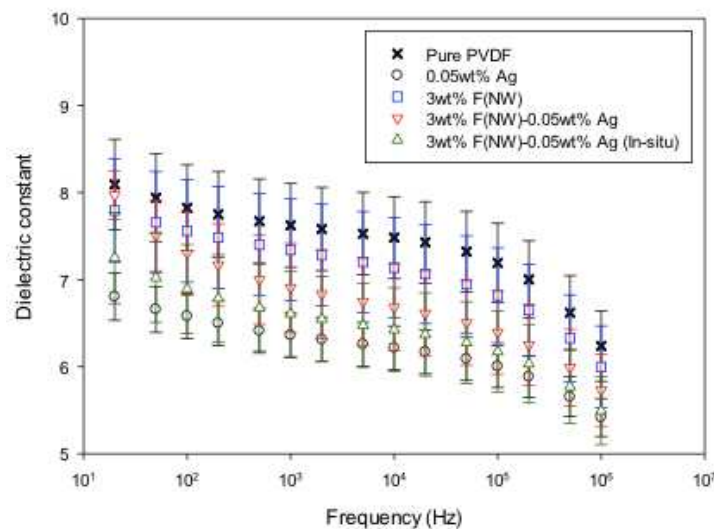


Figure V-5. Dielectric constant of two- and three-phase Ag-F(NW)-PVDF composites compared to the pure PVDF

Moreover, Figure V-6 shows a slight increase in the dielectric loss at low frequencies and a slight decrease at high frequencies. The low contents of treated nano wires (3wt% F(NW)) and Ag nanoparticles (0.05wt%) did not significantly impact the dielectric properties of PVDF.

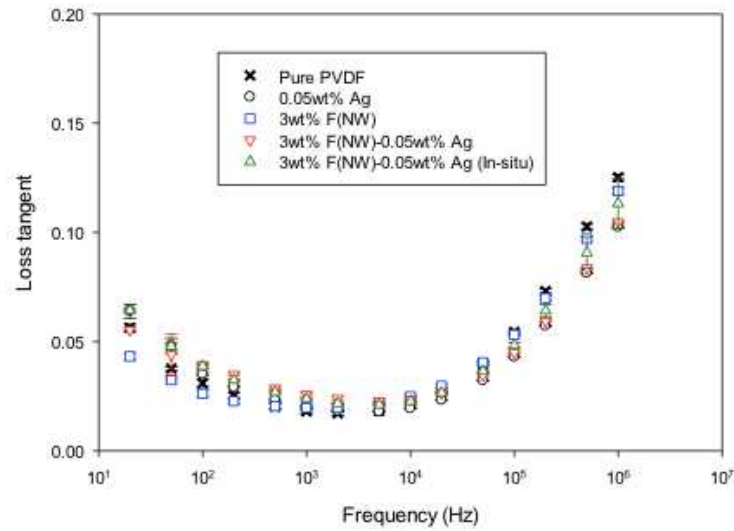


Figure V-6. Dielectric loss of two- and three-phase Ag-F(NW)-PVDF composites compared to the pure PVDF

In order for the Coulomb blockade effect to occur, the Ag particles radius has to satisfy (I-2) where ϵ is the dielectric constant of 3wt%F(NW)-PVDF composite.

$$R < R_{max} = \frac{e^2}{8\pi \cdot \epsilon_0 \epsilon \cdot k_B T} = \frac{8.34 \cdot 10^{-6}}{\epsilon T} \quad (I-2)$$

The dielectric constant of 3wt% F(NW)-PVDF at room temperature is shown in Figure V-7 and the corresponding maximum radius for Ag particles, in order to

Coulomb blockade effect to occur, is displayed in same figure. With the particles with 6.5nm diameter, the Coulomb blockade is expected to occur, increasing the electrical resistivity and dielectric breakdown of the composite at room temperature.

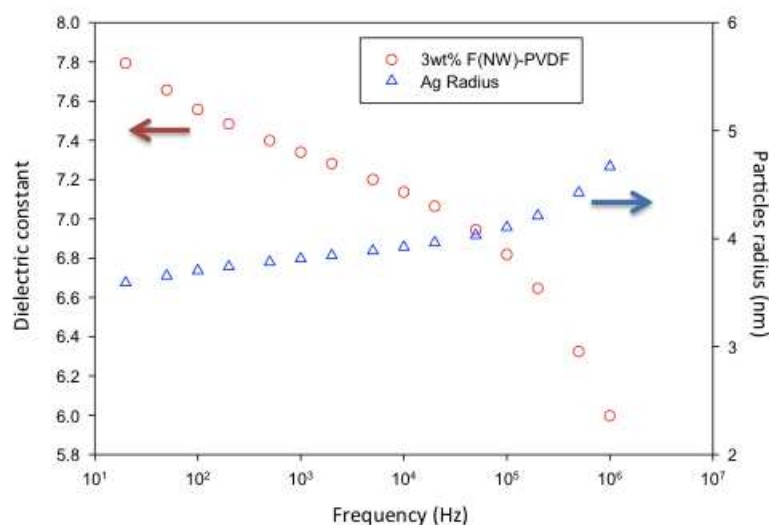


Figure V-7. Dielectric constant of 3wt% F(NW)-PVDF and the corresponding maximum Ag radius required for Coulomb blockade effect to occur

(b) Resistivity measurements

The pure PVDF, two-phase and three-phase composites resistivity values are measured at room temperature and at -100C. Table V-2 summarizes the resistivity measurements for the different composites. In both measurements, all the composites have higher resistivity compared to the pure PVDF. The lowest resistivity in both temperatures is measured for 3wt% F(NW)-0.05wt% Ag-PVDF with in-situ Ag nanoparticles. The three-phase composite with ex-situ Ag nanoparticles has a resistivity

between those of Ag-PVDF and F(NW)-PVDF composites. Figure V-8 and Figure V-9 show the current measured by the different samples when subjected to a voltage varying from 0 to 500V. The x-axis represents the electric field instead of voltage in order to account for the different samples' thickness.

Table V-2. Resistivity measurements at 25 and -100°C

	ρ ($10^9 \Omega.m$)	
	At 25 °C	At -100°C
Pure PVDF	184±17	12547±2279
3wt% F(NW)	235±22	13777±650
0.05wt% Ag (6nm)	240±50	16941±421
3wt% F(NW)-0.05wt% Ag (6nm)	253±54	15153±429
3wt% F(NW)-0.05wt% Ag (In-situ)	334±90	17510±769

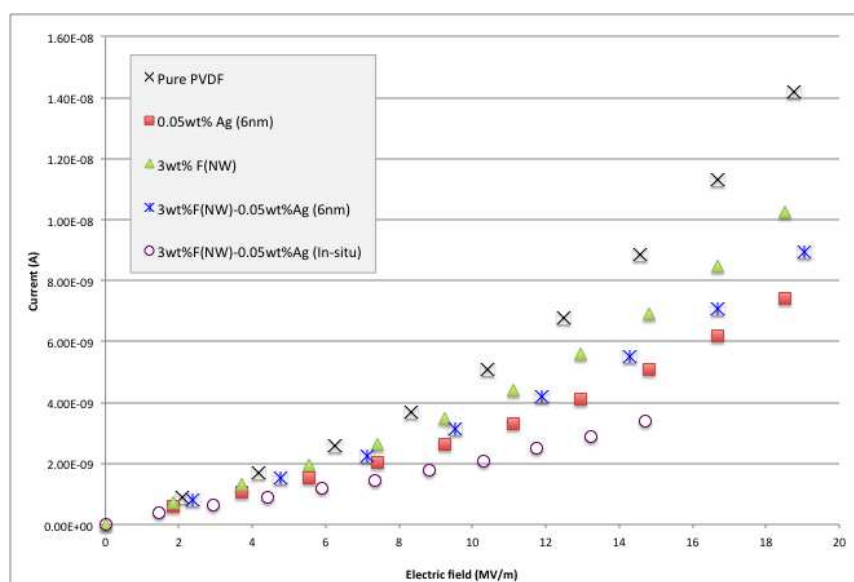


Figure V-8. Current as a function of electric field for the pure PVDF and composites with Ag nanoparticles and TiO_2 nano wires measured at room temperature

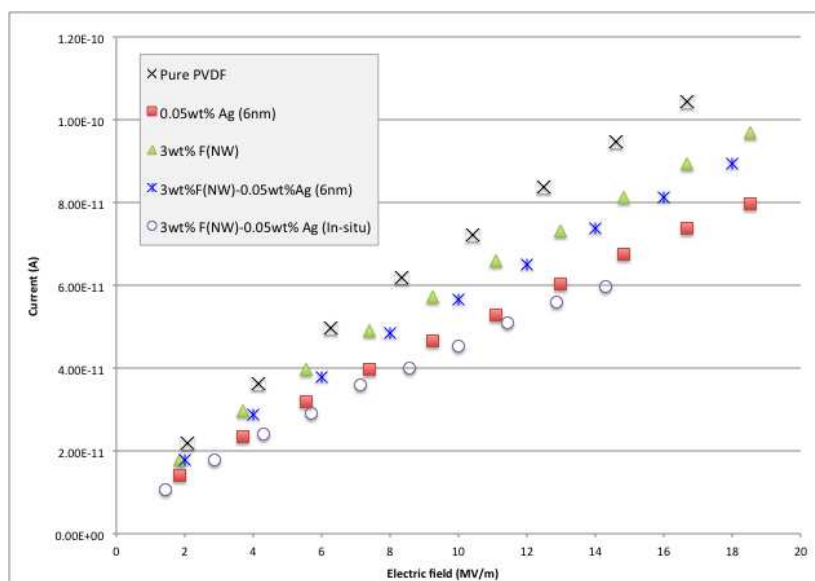


Figure V-9. Current as a function of electric field for the pure PVDF and composites with Ag nanoparticles and TiO_2 nano wires measured at -100C

The resistivity values measured at -100C are higher than the ones measured at room temperature. This is due to the lower thermal energy available in the systems at -100C to transfer the mobile carriers present. It is expected that the resistivity would increase when the temperature decreases [114-116], however more measurements at other temperatures are required to predict the temperature dependence trend particularly around the polymer's glass transition temperature.

(c) Dielectric breakdown

Table V-3 summarizes the dielectric constant and loss tangent at 1kHz, DC dielectric breakdown and energy density of three-phase composites compared to the pure PVDF and the two-phase composite.

Table V-3. Dielectric properties of three-phase composites compared to the pure PVDF and two-phase composite

	Thickness (μm)	E_b (MV/m)	β	ϵ' @1kHz	$\tan(\delta)$ @1kHz	U (J/cc)
Pure PVDF	22 \pm 3	172	9	7.2	0.020	0.94
0.05wt% Ag-PVDF	29 \pm 2	188	4	6.4	0.020	0.99
3wt% F(NW)-PVDF	26 \pm 3	265	12	7.3	0.019	2.28
3wt% F(NW)-0.05wt%Ag PVDF (In-situ)	28 \pm 3	276	5	6.6	0.024	2.23
3wt% F(NW)-0.05wt%Ag PVDF (Ex-situ)	23 \pm 3	288	10	7.5	0.026	2.76

With the addition of the Ag nanoparticles to the 3wt% F(NW)-PVDF composite, in-situ and ex-situ, there is an increase in the dielectric breakdown. This can be related to the increase in resistivity for the three-phase composites. The ex-situ 3wt% F(NW)-0.05wt% Ag-PVDF has an energy density the highest energy density among all the composites. The addition of 0.05wt% Ag nanoparticles (ex-situ) led to a 20% increase compared to the two-phase composite and about 195% compared to the pristine polymer. However the energy density remained in the same range for the in-situ three-phase composite when compared to the two-phase composite with functionalized TiO₂ nano wires. Furthermore, there is a slight increase in the dielectric loss.

(d) Activation energy calculations

Using the same procedure described in Chapter IV, the activation energy is calculated from the dielectric spectroscopy. Table V-4 summarizes the activation energy for the pure PVDF, two- and three-phase composites. The 0.05wt% Ag-PVDF has the highest activation energy, 2.12eV, followed by the ex-situ 3wt% F(NW)-0.05wt% Ag-PVDF composite, 1.69eV. The 3wt% F(NW)-PVDF composite has a higher activation energy of 1.36eV compared to the pure PVDF. The addition of Ag nanoparticles resulted in a further increase in the activation energy compared to the 3wt% F(NW)-PVDF composite for both ex-situ and in-situ composites that has activation energies of 1.69 and 1.40eV, respectively. This increase in activation energy indicates that the addition of Ag nanoparticles led to the creation of deeper traps, requiring higher energies to transfer the electrons and therefore creating a conductive path through the composite. The activation energy calculations correlate with the electrical resistivity and dielectric breakdown

measurements, where deeper traps in the system leads to higher resistivity and breakdown electric field.

Examples of activation energy calculations are shown in Appendix B.

Table V-4. Activation energy calculated from dielectric spectroscopy

	Activation energy (eV)
Pure PVDF	1.03
0.05wt% Ag	2.12
3wt% F(NW)	1.36
3wt% F(NW)-0.05wt% Ag	1.69
3wt% F(NW)-0.05wt% Ag (In-situ)	1.40

The resistivity measurements show that the three-phase composite has higher resistivity compared to the ex-situ three-phase composite. On the other hand, dielectric spectroscopy shows that the ex-situ three-phase composite has a higher activation energy compared to the in-situ composite. These different behaviors might be due to the different mechanisms involved in the measurements, as the dielectric spectroscopy comprises measurements under AC conditions, however resistivity measurements are done under DC conditions. Moreover, it might be possible that the composites processing has an effect on the three-phase composites performance. More studies are required to fully identify the transport mechanisms happening in these composites. In either case, it is interesting that the addition of metallic nanoparticles, Ag, led to an increase in resistivity and activation energy. This might be due to the quantum

confinement, where the nanosized Ag particles might be acting as trapping sites for the electrons, electrons scattering due to the Ag nanoparticles or the interphase around the Ag nanoparticles. The contrast between the polymer matrix and the Ag particles inherent electrical properties might create an interphase that traps mobile carriers present in the composite. Further investigation is required in order to make a clear-cut conclusion about what mechanisms are governing this behavior.

CHAPTER VI

CONCLUSIONS AND SUGGESTIONS FOR FUTURE WORK

The main objective for this study is optimizing a polymer composite for energy storage applications using a low content of particles to maintain flexibility and low dielectric loss. To fulfill this objective, titania dielectric particles having a range of sizes, aspect ratios, volume content and surface chemistry were studied in order to make a judicious choice when incorporating them in the polymer composite.

As a first step, we investigated the role of size and aspect ratio of the dielectric particle on dielectric constant, loss and breakdown of resulting composites. Composites with nano spheres (NS), micro spheres (MS), nano rods (NR) and nano wires (NW) at 4.6vol% loading were characterized. We found that both aspect ratio and size impact the dielectric constant value, where a combination of high aspect ratio and characteristic length resulted in the greatest enhancement of the dielectric constant, as shown in Figure III-5. Specifically, addition of TiO₂ NR to PVDF polymer matrix resulted in the highest enhancement in the dielectric constant especially at low frequencies. This improvement is due to a combination of high interfacial surface area and enhancement in local fields due to the random distribution of the high aspect ratio particles. The effect of the aspect ratio on the dielectric constant was modeled by effective medium approach (EMA); however the interfacial area effect was not accounted for in the EMA, which explains the difference between the effective dielectric constant calculated and the measured value at 1Hz for the composite with NR. ($\epsilon_{\text{model}}=9$ and $\epsilon_{\text{experimental}}=35$)

As for dielectric breakdown, the particles with the highest aspect ratio, i.e., NW, had the highest dielectric breakdown among the different composites. This is most likely related to the NW's planar distribution in the nanocomposite. A planar distribution resulted from the solution casting technique (see Chapter II); a 2D distribution results in a limited enhancement in local fields because the applied electric field is along the particles transversal axis rather than their longitudinal axis. Limiting the local field enhancement increases the dielectric breakdown, which in turn increases the material's energy density. Since the dielectric breakdown, E_b , has a higher effect on the energy density compared to the dielectric constant, because the energy density is proportional to E_b^2 , the nanocomposite containing NW, the particles with the highest aspect ratio, had the highest energy density among all the composites. We note however that, despite the fact that the NW-PVDF nanocomposite had the highest energy density of all nanocomposites at this stage, it did not compare favorable to the pure PVDF. This might have been caused by a weak interaction between the particles and the polymer matrix and particle agglomerations; these two factors create nano voids in the composite causing a decrease in the dielectric breakdown.

As a second step and in order to enhance the interaction between the particles and the polymer matrix, the NW particles were chemically treated with a silane-coupling agent. The particle functionalization resulted in an enhancement in the dielectric constant without a significant increase in the dielectric loss, as compared to the as-received NWs. Furthermore; the particle's treatment enhanced the dielectric breakdown up to 4.6vol% loading of the NW particles. At 4.6vol%, an enhancement of 500% was

measured for the energy density compared to the pristine polymer due to a simultaneous increase in dielectric constant and dielectric breakdown, while the dielectric loss remained in the same range as that of the pure polymer. Microscopy study and Raman spectroscopy showed that the NWs have a preferred planar (2D) distribution, parallel to the film's casting direction. This planar distribution further contributed to the enhancement in the dielectric properties, where an increase in the dielectric breakdown was possible despite the high aspect ratio geometry, owing to the small local fields along the particles' transversal axis. Moreover, the particle functionalization resulted in an increase in the activation energy in the composite, which contributed to the enhancement in the dielectric breakdown. At such a low content, the polymer's lightweight, processability and flexibility were maintained as shown in Figure VI-1.



Figure VI-1. Flexible NW-PVDF composite

An investigation of the thickness effect on the composites' dielectric breakdown showed that there is an important dependence on thickness for the higher particle content (4.6vol% F(NW)-PVDF). The thinnest film, $t=19\mu\text{m}$, resulted in the highest dielectric breakdown. This can be related to the smaller number of defects present in thinner samples; in addition, a thinner sample will promote a better planar distribution of the high aspect ratio particles. Therefore processing also plays a big role, where a thinner nanocomposite might result in more significant improvement in the energy density.

As a third step, we investigated the effect of adding nano metallic particles to the two-phase composite and monitored the dielectric properties and electrical resistivity. Ag nanoparticles were added to a 3wt% F(NW) both using ex-situ and in-situ techniques. An increase in the dielectric breakdown and resistivity was measured. This increase can be due to an interphase effect, quantum confinement due to the presence of Ag nanoparticles, also called Coulomb blockade effect, and/or electrons scattering. However, there was a slight increase in the dielectric loss despite the low content of the added particles. This might have been due to agglomerations of the Ag nanoparticles. A better dispersion of the Ag nanoparticles might lead to more trapping sites and therefore enhance the dielectric response of the composite.

As a summary, a 500% improvement in energy density was measured at a low content of 4.6vol% high aspect ratio TiO_2 particles with a low dielectric loss, comparable to that of the pristine PVDF. The processing technique produced a planar distribution of the TiO_2 nano wires in the composite; a further alignment of the particles might lead to an even higher enhancement. At 9.2vol%, the processing procedure used

was not able to yield a planar distribution of the nano wires resulting in a decrease in the dielectric breakdown. A possible solution for this challenge is to manipulate the nano wires mechanically or electrically to align them. An additional research path would be to focus on the effect of the PVDF phases, including the nonpolar α -phase. Varying the processing procedures to obtain different PVDF phases would affect the composites properties going from a linear to a non-linear behavior in the electrical displacement response as a function of electric field. Exploring other high dielectric polymers, such as PVDF co and terpolymers would be interesting from the point of view electrical, dielectric and piezoelectric properties of the composite [17, 117, 118]. Finally, the addition of a very low content of Ag nanoparticles to the two-phase TiO₂-PVDF resulted in an increase in the dielectric breakdown and electrical resistivity. However a slight increase in the dielectric loss was measured, most probably due to agglomerated particles. An enhancement in the particles dispersion would result in better effective dielectric and electrical properties, so focusing on functionalization of Ag to lead to even better dispersion would be a good future focus. Moreover, the in-situ Ag nanoparticles processing led to polydispersity in the Ag, with particle diameter varying from 5 to 15 nm. More control on the particles size to get monodisperse nanoparticles with the smallest size possible promises to achieve the highest interfacial area between the particles and the polymer matrix and hence the highest interphase effect on dielectric and electrical properties.

REFERENCES

- [1] J. McPherson, J. Kim, A. Shanware, H. Mogul, and J. Rodriguez, "Proposed universal relationship between dielectric breakdown and dielectric constant," Digest. International Electron Devices Meeting (IEDM), pp. 633-636, 2002.
- [2] M. Roy, J. K. Nelson, R. K. MacCrone, and L. S. Schadler, "Candidate mechanisms controlling the electrical characteristics of silica/XLPE nanodielectrics " *J. Mater. Sci.*, vol. 42, pp. 3789-3799, 2007.
- [3] S.-H. Xie, B.-K. Zhu, X.-Z. Wei, Z.-K. Xu, and Y.-Y. Xu, "Polyimide/BaTiO₃ composites with controllable dielectric properties," *Compos. Part A-Apl. S.*, vol. 36, pp. 1152-1157, 2005.
- [4] Z. M. Dang, Wang, H. Y. and Xu, H. P., "Influence of silane coupling agent on morphology and dielectric property in BaTiO₃/polyvinylidene fluoride composites," *Appl. Phys. Lett.*, vol. 89, pp. 112902(1)-112902(3), 2006.
- [5] A. Choudhury, "Dielectric and piezoelectric properties of polyetherimide/BaTiO₃ nanocomposites," *Mater. Chem. Phys.*, vol. 121, pp. 280-285, 2010.
- [6] F. J. Wang, W. Li, M. S. Xue, J. P. Yao, and J. S. Lu, "BaTiO₃-polyethersulfone nanocomposites with high dielectric constant and excellent thermal stability," *Compos. Part B-Eng.*, vol. 42, pp. 87-91, 2011.
- [7] X. Dou, X. Liu, Y. Zhang, H. Feng, J.-F. Chen¹, and S. Du, "Improved dielectric strength of barium titanate-polyvinylidene fluoride nanocomposite," *Appl. Phys. Lett.*, vol. 95, pp. 132904(1)- 132904(3), 2009.
- [8] S. Siddabattuni, T. P. Schuman, and F. Dogan, "Improved polymer nanocomposite dielectric breakdown performance through barium titanate to epoxy interface control," *Mater. Sci. Eng. B-Adv.*, vol. 176, pp. 1422-1429, 2011.
- [9] M. Iijima, N. Sato, I. W. Lenggoroa and H. Kamiya, "Surface modification of BaTiO₃ particles by silane coupling agents in different solvents and their effect

- on dielectric properties of BaTiO₃/epoxy composites," *Colloid Surface A*, vol. 352, pp. 88-93, 2009.
- [10] J. K. Nelson and H. Yu. , "Nanocomposite dielectrics—properties and implications," *J. Phys. D Appl. Phys.*, vol. 38, pp. 213-222, 2005.
- [11] T.-I. Yang and P. Kofinas, "Dielectric properties of polymer nanoparticle composites," *Polymer*, vol. 48, pp. 791-798, 2007.
- [12] J. Li, S. Seok, B. Chu, F. Dogan, Q. Zhang, and Q. Wang, "Nanocomposites of Ferroelectric Polymers with TiO₂ Nanoparticles Exhibiting Significantly Enhanced Electrical Energy Density," *Adv. Mater.*, vol. 21, pp. 217–221, 2009.
- [13] N. An, H. Liu, Y. Ding, M. Zhang, and Y. Tang, "Preparation and electroactive properties of a PVDF/nano-TiO₂ composite film," *Appl. Surf. Sci.*, vol. 257, pp. 3831-3835, 2011.
- [14] J. C. Fothergill, J. K. Nelson and M. Fu., "Dielectric Properties of Epoxy Nanocomposites containing TiO₂, Al₂O₃ and ZnO fillers," presented at the Conference on Electrical Insulation and Dielectric Phenomena, 2004.
- [15] S. Singha and M. J. Thomas, "Dielectric properties of epoxy nanocomposites," *IEEE Trans. Dielectr. Electr. Insul.*, vol. 15, pp. 12-23, 2008.
- [16] P. Murugaraj, D. Mainwaring and N. Mora-Huertas, "Dielectric enhancement in polymer-nanoparticle composites through interphase polarizability," *J. Appl. Phys.*, vol. 98, pp. 054304-6, 2005.
- [17] B. Chu, M. Lin, B. Neese, X. Zhou, Q. Chen and Q. M. Zhang, "Large enhancement in polarization response and energy density of poly(vinylidene fluoride-trifluoroethylene-chlorofluoroethylene) by interface effect in nanocomposites," *Appl. Phys. Lett.*, vol. 91, 2007.
- [18] T. Tanaka, "Dielectric nanocomposites with insulating properties," *IEEE Trans. Dielectr. Electr. Insul.*, vol. 12, pp. 914-928, 2005.

- [19] Z.-M. Dang, J.-K. Yuan, J.-W. Zha, T. Zhou, S.-T. Li, and G.-H. Hu, "Fundamentals, processes and applications of high-permittivity polymer-matrix composites," *Prog. Mater. Sci.*, vol. 57, pp. 660-723, 2012.
- [20] E. Amendola, A. M. Scamardella, C. Petrarca and D. Acierno, "Epoxy-nanocomposites with ceramic reinforcement for electrical insulation," *J. Appl. Polym. Sci.*, vol. 122, pp. 3686-3693, 2011.
- [21] R. C. Smith, J. K. Nelson and L. S. Schadler, "Electrical behavior of particle-filled polymer nanocomposites," in *Physical Properties and Applications of Polymer Nanocomposites*, S. C. Tjong and Y. W. Mai, Eds., ed Philadelphia, PA: Woodhead Publishing, 2010.
- [22] N. Guo, S. A. DiBenedetto, P. Tewari, M. T. Lanagan, M. A. Ratner and T. J. Marks, "Nanoparticle, Size, Shape, and Interfacial Effects on Leakage Current Density, Permittivity, and Breakdown Strength of Metal Oxide-Polyolefin Nanocomposites: Experiment and Theory," *Chem. Mater.*, vol. 22, pp. 1567-1578, 2010.
- [23] H. Tang, Y. Lin, C. Andrews and H. A. Sodano, "Nanocomposites with increased energy density through high aspect ratio PZT nanowires," *Nanotechnology*, vol. 22, pp. 015702(1)- 015702(8), 2011.
- [24] V. Tomer, "Polymer nanocomposites for electrical energy storage: Effect of structuring, interfaces and filler types," PhD, The Pennsylvania State University, 2010.
- [25] G. Subodh, V. Deepu, P. Mohanan and M. T. Sebastian, "Dielectric response of Sr₂Ce₂Ti₅O₁₅ ceramics reinforced high density polyethylene," *J. Phys. D Appl. Phys.*, vol. 42, pp. 225501(1)- 225501(5) 2009.
- [26] J. Unsworth, J. Du, B. J. Crosby and M. G. Stevens, "Complex electrical permittivity of 0-3 superconducting ceramic/polymer composites," *Mater. Res. Bull.*, vol. 27, pp. 1161-1169, 1992.
- [27] Y. Shen, A. Gu, G. Liang and L. Yuan, "High performance CaCu 3Ti 4O 12/cyanate ester composites with excellent dielectric properties and thermal resistance," *Compos. Part A-Appl. S.*, vol. 41, pp. 1668-1676, 2010.

- [28] S. L. Jiang, Y. Yu and Y. K. Zeng, "Novel Ag–BaTiO₃/PVDF three-component nanocomposites with high energy density and the influence of nano-Ag on the dielectric properties," *Curr. Appl. Phys.*, vol. 9, pp. 956-959, 2009.
- [29] J. Lu, K.-S. Moon, J. Xu and C. P. Wong, "Synthesis and dielectric properties of novel high-K polymer composites containing in-situ formed silver nanoparticles for embedded capacitor applications," *J Mater. Chem.*, vol. 16, p. 1543, 2006.
- [30] M. Xu, J. Feng and X. Cao, "Conductive property of metal nano-particle/polymer composite dielectrics," *Int. Sym. Electr. Insul. Mater. (ISEIM)*, pp. 83-86, 2008.
- [31] M. Xu, J. Feng and X. Cao, "Electrical properties of nano-silver/polyacrylamide/ethylene vinyl acetate composite," *Journal of Shanghai University (English Edition)*, vol. 12, pp. 85-90, 2008.
- [32] Q. Feng, Z. Dang, N. Li and X. Cao, "Preparation and dielectric property of Ag–PVA nano-composite," *Mater. Sci. Eng. B-Adv.*, vol. 99, pp. 325-328, 2003.
- [33] X. Man, F. Junqiang and C. Xiaolong, "Study on preparation and dielectric properties of Nano-Ag/Epoxy resin composite," 8th International Conference on Properties and applications of Dielectric Materials, pp.852-856, 2006.
- [34] C. Schonenberger, H. Vanhouten, H. C. Donkersloot, A. M. T. Vanderputten and L. G. J. Fokkink, "Single-electron tunneling up to room-temperature," *Phys. Scr.*, vol. T45, pp. 289-291, 1992.
- [35] W. Chen and H. Ahmed, "Coulomb blockade at 77 K in nanoscale metallic islands in a lateral nanostructure," *Appl. Phy. Lett.*, vol. 66, pp. 3383, 1995.
- [36] Y. Medvedev and A. Grishin, "The charge state of conducting fine-dispersed systems in an insulating matrix," *Phys. Solid State*, vol. 43, pp. 935-940, 2001.
- [37] D. Chakravorty, "Quantum confinement effect in nanocomposites," *Appl. Surf. Sci.*, vol. 182, pp. 251-257, 2001.

- [38] G. Schmid and I. Wiley online, *Nanoparticles: from theory to application*. Weinheim : Chichester: Wiley-VCH ; John Wiley, 2004.
- [39] W. D. Callister, *Fundamentals of materials science and engineering : an integrated approach*, Wiley, 2005.
- [40] R. L. Chen C Ku, *Electrical properties of polymers: chemical principles*, Hanser Publishers, 1987.
- [41] P. Barber, S. Balasubramanian, Y. Anguchamy, S. Gong, A. Wibowo, H. Gao, H. Ploehn and H.-C. Zur Loye, "Polymer Composite and Nanocomposite Dielectric Materials for Pulse Power Energy Storage," *Materials*, vol. 2, pp. 1697-1733, 2009.
- [42] N. Lockyer, "Electric Strength of Some Solid Dielectrics," *Nature (London)*, vol. 146, pp. 594-595, 1940.
- [43] R. Cooper, "The electric strength of solid dielectrics," *British J. Appl. Phys.*, vol. 17, 1966.
- [44] H. Bluhm, *Pulsed Power Systems*. [New York]: Springer-Verlag Berlin Heidelberg, 2006.
- [45] R. M. Hill and L. A. Dissado, "Theoretical basis for the statistics of dielectric breakdown," *J Phys. C Solid State*, vol. 16, pp. 2145-2156, 1983.
- [46] L. A. Dissado, J. C. Fothergill, S. V. Wolfe, and R. M. Hill, "Weibull Statistics in Dielectric Breakdown; Theoretical Basis, Applications and Implications," *IEEE T Electr. Insul.*, vol. EI-19, pp. 227-233, 1984.
- [47] G. C. Stone and R. G. van Heeswijk, "Parameter Estimation for the Weibull Distribution," *IEEE T Electr. Insul.*, vol. EI-12, pp. 253-261, 1977.
- [48] H. Fröhlich, "Dielectric breakdown in solids," *Rep. Prog. Phys.*, vol. 6, 1939.
- [49] M. S. Naidu, *High Voltage Engineering*. India: Tata McGraw-Hill, 2009.

- [50] A. J., "Electric strength of polymers," *J. Phys. D Appl. Phys.*, vol. 29, pp. 446-456, 1996.
- [51] M. Ieda, "Dielectric Breakdown Process of Polymers," *Electrical Insulation, IEEE Transactions on*, vol. EI-15, pp. 206-224, 1980.
- [52] V. A. Zakrevskii, N. T. Sudar, A. Zaopo, and Y. A. Dubitsky, "Mechanism of electrical degradation and breakdown of insulating polymers," *J. Appl. Phys.*, vol. 93, pp. 2135-2139, 2003.
- [53] D. B. Watson, W. Heyes, K. C. Kao, and J. H. Calderwood, "Some Aspects of Dielectric Breakdown of Solids," *IEEE T Electr. Insul.*, vol. EI-1, pp. 30-37, 1965.
- [54] M. F. Frechette, M. Trudeau, H. D. Alamdari, and S. Boily, "Introductory remarks on nanodielectrics," in *Electrical Insulation and Dielectric Phenomena, 2001 Annual Report. Conference on*, 2001, pp. 92-99.
- [55] T. Tanaka, G. C. Montanari, and R. Mulhaupt, "Polymer nanocomposites as dielectrics and electrical insulation-perspectives for processing technologies, material characterization and future applications," *IEEE T Dielect. El. In.*, vol. 11, pp. 763-784, 2004.
- [56] J. K. Nelson, "The promise of dielectric nanocomposites," in *IEEE Int. Sym. Elec.*, pp. 452-457, 2006.
- [57] M. F. Frechette and C. W. Reed, "The emerging field of nanodielectrics an annotated appreciation," in *IEEE Int. Sym. Elec.*, pp. 458-465, 2006.
- [58] T. Tanaka, M. Kozako, N. Fuse, and Y. Ohki, "Proposal of a multi-core model for polymer nanocomposite dielectrics," *IEEE T Dielect. El. In.*, vol. 12, pp. 669-681, 2005.
- [59] T. J. Lewis, "Interfaces are the dominant feature of dielectrics at the nanometric level," *IEEE T Dielect. El. In.*, vol. 11, pp. 739-753, 2004.

- [60] J. K. Nelson and J. C. Fothergill, "Internal Charge behavior of nanocomposites," *Nanotechnology*, vol. 15, pp. 586-595, 2004.
- [61] J. K. Nelson, Fothergill, J. C., Dissado, L. A. and Peasgood, W. , "Towards an understanding of nanometric dielectrics," in *2002 Annual Report Conference on Electrical Insulation and Dielectric Phenomena (2002)*: 20-24, 2002, pp. 20-24.
- [62] J.-W. Kim, W.-J. Cho, and C.-S. Ha, "Morphology, crystalline structure, and properties of poly(vinylidene fluoride)/silica hybrid composites," *J. Polym. Sci. Pol. Phys.*, vol. 40, pp. 19-30, 2002.
- [63] Y. Wang, X. Zhou, Q. Chen, B. Chu, and Q. Zhang, "Recent development of high energy density polymers for dielectric capacitors," *IEEE T Dielect. El. In.*, vol. 17, pp. 1036-1042, 2010.
- [64] P. Thomas, Satapathy, S., Dwarakanath, K. and Varma, K. B. R., "Dielectric properties of poly(vinylidene fluoride)/CaCu₃Ti₄O₁₂ nanocrystal composite thick films," *eXPRESS Polymer Letters*, vol. 4, 2010.
- [65] T. Jow, "Dielectric breakdown of polyvinylidene fluoride and its comparisons with other polymers," *J. Appl. Phys.*, vol. 73, p. 5147, 1993.
- [66] W. Li, "Electric energy storage properties of poly(vinylidene fluoride)," *Appl. Phys. Lett.*, vol. 96, p. 192905, 2010.
- [67] R. Gregorio and E. M. Ueno, "Effect of crystalline phase, orientation and temperature on the dielectric properties of poly (vinylidene fluoride) (PVDF)," *J. Mater. Sci.*, vol. 34, pp. 4489-4500, 1999.
- [68] "Dielectric breakdown of polyvinylidene fluoride and its comparisons with other polymers," *J. Appl. Phys.*, vol. 73, p. 5147, 1993.
- [69] M. Hikita and et al., "Electrical breakdown and solid structure of poly(vinylidene-fluoride)," *J. Phys. D Appl. Phys.*, vol. 16, p. L157, 1983.

- [70] C. M. Costa, S. Firmino Mendes, V. Sencadas, A. Ferreira, R. Gregorio Jr, J. L. Gómez Ribelles, and S. Lanceros-Méndez, "Influence of processing parameters on the polymer phase, microstructure and macroscopic properties of poly(vinylidene fluoride)/Pb(Zr_{0.53}Ti_{0.47})O₃ composites," *J. Non-Cryst. Solids*, vol. 356, pp. 2127-2133, 2010.
- [71] M. Benz and W. B. Euler, "Determination of the crystalline phases of poly(vinylidene fluoride) under different preparation conditions using differential scanning calorimetry and infrared spectroscopy," *J. Appl. Polym. Sci.*, vol. 89, pp. 1093-1100, 2003.
- [72] R. Gregorio, "Determination of the α , β , and γ crystalline phases of poly(vinylidene fluoride) films prepared at different conditions," *J. Appl. Polym. Sci.*, vol. 100, pp. 3272-3279, 2006.
- [73] X. He and K. Yao "Crystallization mechanism and piezoelectric properties of solution-derived ferroelectric poly(vinylidene fluoride) thin films," *Appl. Phys. Lett.*, vol. 89, 2006.
- [74] R. Imamura, A. B. Silva, and R. Gregorio Jr., "g \rightarrow b Phase Transformation Induced in Poly(vinylidene fluoride) by Stretching," *J. Appl. Polym. Sci.*, vol. 110, pp. 3242-3246, 2008.
- [75] U. Mizutani, *Introduction to the Electron Theory of Metals*: Cambridge University Press, 2001.
- [76] C. H. Spink, "Differential scanning calorimetry," *Methods in cell biology*, vol. 84, pp. 115-41, 2008.
- [77] C. Schick, "Differential scanning calorimetry (DSC) of semicrystalline polymers," *Anal. Bioanal. Chem.*, vol. 395, p. 1589, 2009.
- [78] Y. Kong, "The measurement of the crystallinity of polymers by DSC," *Polymer (Guilford)*, vol. 43, pp. 3873-3878, 2002.

- [79] V. Sencadas, S. Lanceros-Méndez, and J. F. Mano, "Characterization of poled and non-poled β -PVDF films using thermal analysis techniques," *Thermochim. Acta*, vol. 424, pp. 201-207, 2004.
- [80] S. Mohamadi and N. Sharifi-Sanjani, "Investigation of the crystalline structure of PVDF in PVDF/PMMA/graphene polymer blend nanocomposites," *Polym. Composite.*, vol. 32, pp. 1451-1460, 2011.
- [81] R. N. Rotheron, *Particulate-filled polymer composites*. UK: Ismithers Rapra, 2003.
- [82] M. S. Amer, *Raman spectroscopy for soft matter applications*: Wiley, 2009.
- [83] D. Wolverson, "Raman spectroscopy," ed: Elsevier Science & Technology, 2008, pp. 249-288.
- [84] A. L. Bassi, D. Cattaneo, V. Russo, C. E. Bottani, E. Barborini, T. Mazza, P. Piseri, P. Milani, F. O. Ernst, K. Wegner, and S. E. Pratsinis, "Raman spectroscopy characterization of titania nanoparticles produced by flame pyrolysis: The influence of size and stoichiometry," *J. Appl. Phys.*, vol. 98, pp. 074305-9, 2005.
- [85] J. G. Li, T. Ishigaki, and X. Sun, "Anatase, Brookite, and Rutile Nanocrystals via Redox Reactions under Mild Hydrothermal Conditions: Phase-Selective Synthesis and Physicochemical Properties," *J. Phys. Chem. C*, vol. 111, pp. 4969-4976, 2007.
- [86] V. Presser, Schuster, B.-E., Casu, M. B., Heinemeyer, U., Schreiber, F., Nickel K. G. and Chassé, T., "Raman polarization studies of highly oriented organic thin films," *J. Raman Spectrosc.*, vol. 40, pp. 2015–2022, 2009.
- [87] A. International, "Standard Test Method for Tensile Strength and Young's Modulus of Fibers," ed, 2008.
- [88] G. Teyssdre, Mezghani, S., Bernes, A. and Lacabanne, C., "Thermally stimulated currents of polymers," in *Dielectric spectroscopy of polymeric materials fundamentals and applications*, J. P. a. F. Runt, John J., Ed., ed: The American Chemical Society, 1997.

- [89] J. V. Turnhout, "Thermally stimulated discharge of electrets," in *Electrets*. vol. 1, G. M. Sessler, Ed., ed California, USA: Laplacian Press, 1998.
- [90] C. Bucci, R. Fieschi, and G. Guidi, "Ionic Thermocurrents in Dielectrics," *Phys. Revi.*, vol. 148, pp. 816-823, 1966.
- [91] P. K. Khare, Devendra, K S, Verma, A and Srivastava, R K, "Depolarization studies of polyvinylidene fluoride foil electrets using thermally stimulated discharge," *Indian J. Pure Ap. Phy.*, vol. 42, pp. 693-696, 2004.
- [92] X. Chunchuan, H. Janet, and S. Boggs, "Automatic breakdown voltage measurement of polymer films," *IEEE Electr. Insul. M.*, vol. 24, pp. 30-34, 2008.
- [93] D. R. Paul and L. M. Robeson, "Polymer nanotechnology: Nanocomposites," *Polymer*, vol. 49, pp. 3187-3204, 2008.
- [94] P. Bhimaraj, H. Yang, R. W. Siegel, and L. S. Schadler, "Crystal nucleation and growth in poly(ethylene terephthalate)/alumina-nanoparticle composites," *J. Appl. Polym. Sci.*, vol. 106, pp. 4233-4240, 2007.
- [95] R. Krishnamoorti and R. A. Vaia, "Polymer nanocomposites," *J. Polym. Sci. Pol. Phys.*, vol. 45, pp. 3252-3256, 2007.
- [96] L. D. Zhang, H. F. Zhang, G. Z. Wang, C. M. Mo, and Y. Zhang, "Dielectric behaviour of Nano-TiO₂ bulks," *Phys. Status Solidi A*, vol. 157, pp. 483-491, 1996.
- [97] G. G. Raju, *Dielectrics in electric fields*. New York, USA: Marcel Dekker, 2009.
- [98] H. T. Vo and F. G. Shi, "Towards model-based engineering of optoelectronic packaging materials: dielectric constant modeling," *Microelectron. J.*, vol. 33, pp. 409-415, 2002.
- [99] Q. Cheng, C. Li, V. Pavlinek, P. Saha, and H. Wang, "Surface-modified antibacterial TiO₂/Ag⁺ nanoparticles: Preparation and properties," *Appl. Surf. Sci.*, vol. 252, pp. 4154-4160, 2006.

- [100] Y.-Y. Song, H. Hildebrand, and P. Schmuki, "Optimized monolayer grafting of 3-aminopropyltriethoxysilane onto amorphous, anatase and rutile TiO₂," *Surf. Sci.*, vol. 604, pp. 346-353, 2010.
- [101] R. M. Jones, *Mechanics of composite materials*: Taylor & Francis, 1999.
- [102] L. Gerward and J. Staun Olsen, "Post-Rutile High-Pressure Phases in TiO₂," *J. Appl. Crystallogr.*, vol. 30, pp. 259-264, 1997.
- [103] J. Muscat, V. Swamy, and N. M. Harrison, "First-principles calculations of the phase stability of TiO₂," *Phys. Rev. B*, vol. 65, p. 224112, 2002.
- [104] S. Giordano, "Effective medium theory for dispersions of dielectric ellipsoids," *J. Electrostat.*, vol. 58, pp. 59-76, 2003.
- [105] K. Gerhard, R. Sten, and S. Ari, "Mixing formulas in the time domain," *J. Opt. Soc. Am. A*, vol. 15, pp. 1411-1422, 1998.
- [106] S. Grimnes, "DIELECTRICS," ed: Elsevier Science & Technology, 2008, pp. 57-92.
- [107] F. Kremer and A. Schönhal, *Broadband dielectric spectroscopy*: Springer, 2003.
- [108] J. K. Nelson and C. F. John, "Internal charge behaviour of nanocomposites," *Nanotechnology*, vol. 15, p. 586, 2004.
- [109] C. Mayoux, "Degradation of insulating materials under electrical stress," *IEEE T Dielect. El. In.*, vol. 7, pp. 590-601, 2000.
- [110] P. G. C., "Conductivity and dielectric characterization of polymer nanocomposites," in *Physical Properties and Applications of Polymer Nanocomposites: Physical Properties and Applications*, S. C. Tjong and Y. W. Mai, Eds., ed Philadelphia, PA: Woodhead Publishing, 2010.
- [111] R. H. Cole, "Dielectric Polarization and Loss," *Annu. Rev. Phys. Chem.*, vol. 11, pp. 149-168, 1960/10/01 1960.

- [112] L. A. Dissado and J. C. Fothergill, *Electrical degradation and breakdown in polymers*. London: P. Peregrinus, 1992.
- [113] F. Forlani and N. Minnaja, "Thickness Influence in Breakdown Phenomena of Thin Dielectric Films," *phys. status solidi (b)*, vol. 4, pp. 311-324, 1964.
- [114] R. W. Warfield and M. C. Petree, "Electrical resistivity of polymers," *Polym. eng. Sci.*, vol. 1, pp. 80-85, 1961.
- [115] R. W. Warfield and M. C. Petree, "Dependence on Temperature of the Electrical Resistivity of Thermosetting Polymers," *Nature (London)*, vol. 187, pp. 316-317, 1960.
- [116] R. W. Warfield, "Electrical resistivity of a polyamide-epoxide copolymer," *J. Appl. Polym. Sci.*, vol. 30, pp. 1321-1322, 1985.
- [117] B. Chu, X. Zhou, K. Ren, B. Neese, M. Lin, Q. Wang, F. Bauer, and Q. M. Zhang, "A Dielectric Polymer with High Electric Energy Density and Fast Discharge Speed," *Science*, vol. 313, pp. 334-336, 2006.
- [118] C. Baojin, Z. Xin, B. Neese, Q. M. Zhang, and F. Bauer, "Relaxor ferroelectric poly(vinylidene fluoride-trifluoroethylene-chlorofluoroethylene) terpolymer for high energy density storage capacitors," *IEEE T Dielect. El. In.*, vol. 13, pp. 1162-1169, 2006.

APPENDIX A

For repeatability, another series of samples were characterized using TSC to insure the same behavior is followed in the different samples of the same composite. Averaging the output current was not a good idea since the measuring temperature is different for each measurement. Although the difference is not dramatic, averaging x and y-data might cause the loss of some information. It is worth noting that the y-axis has different scales in different graphs.

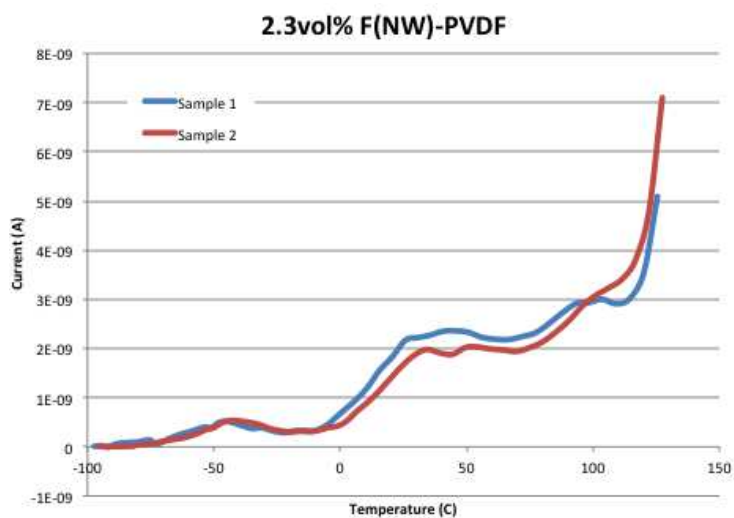


Figure A-1. Comparison of two 2.3vol% F(NW)-PVDF TSC measurements

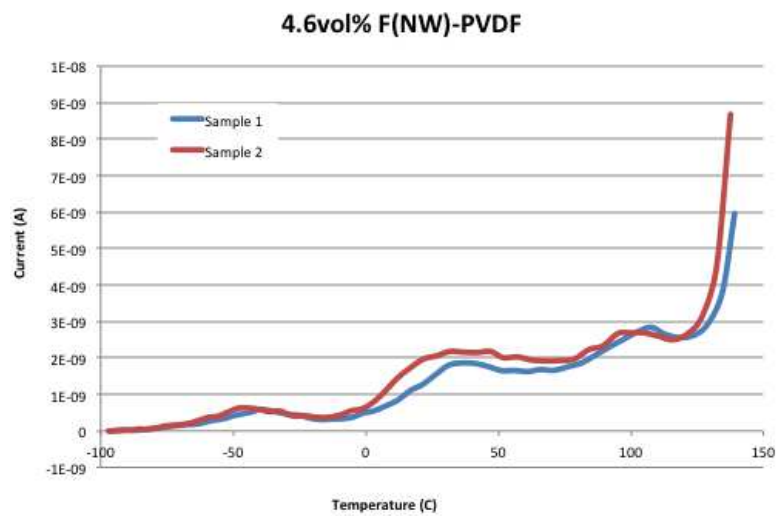


Figure A-2. Comparison of two 4.6vol% F(NW)-PVDF TSC measurements

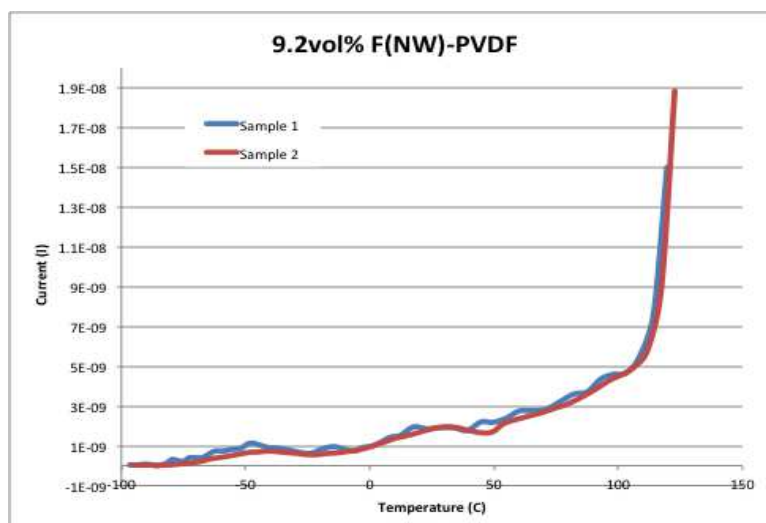


Figure A-3. Comparison of two 9.2vol% F(NW)-PVDF TSC measurements

APPENDIX B

This appendix shows some examples of activation energy estimation from dielectric spectroscopy relaxations. Figure B-1 shows an example of loss tangent as a function of frequency at different temperature for pure PVDF. The relaxation frequencies for the different temperatures are extracted from this plot.

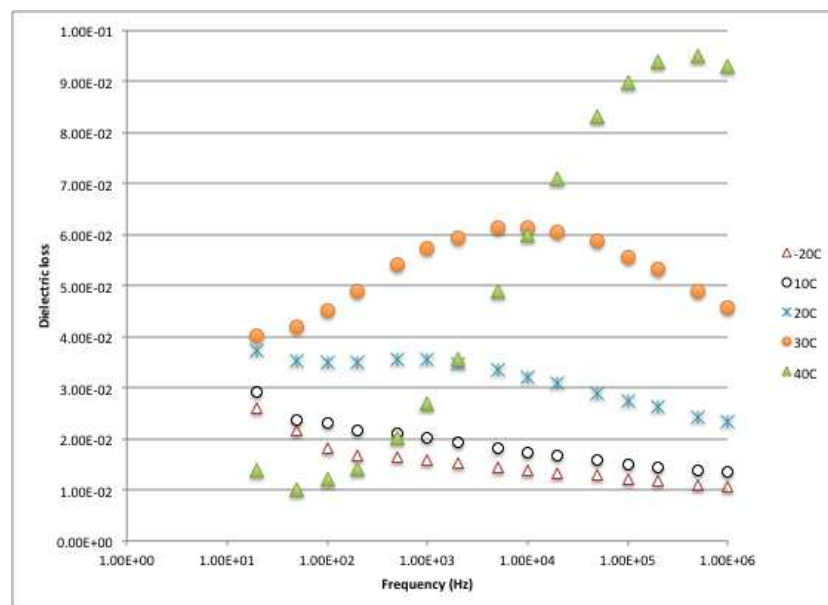


Figure B-1. Dielectric loss as a function of frequency at different temperatures for pure PVDF

The following figures show the linear fitting of $\ln(1/f)$ as a function of $1/T$. The slope is E_a/k , where E_a is the activation energy.

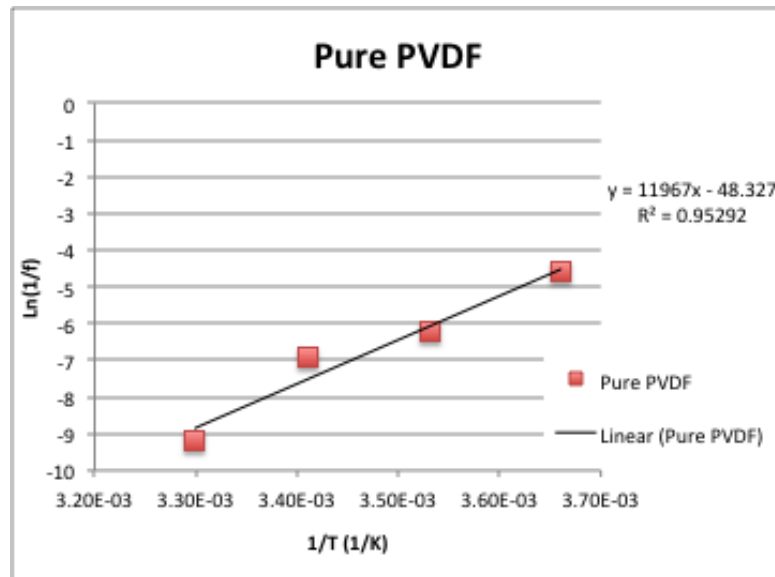


Figure B-2. Linear fitting of $\ln(1/f)$ as a function of $1/T$, where f is the relaxation frequency and T is in Kelvin, for pure PVDF

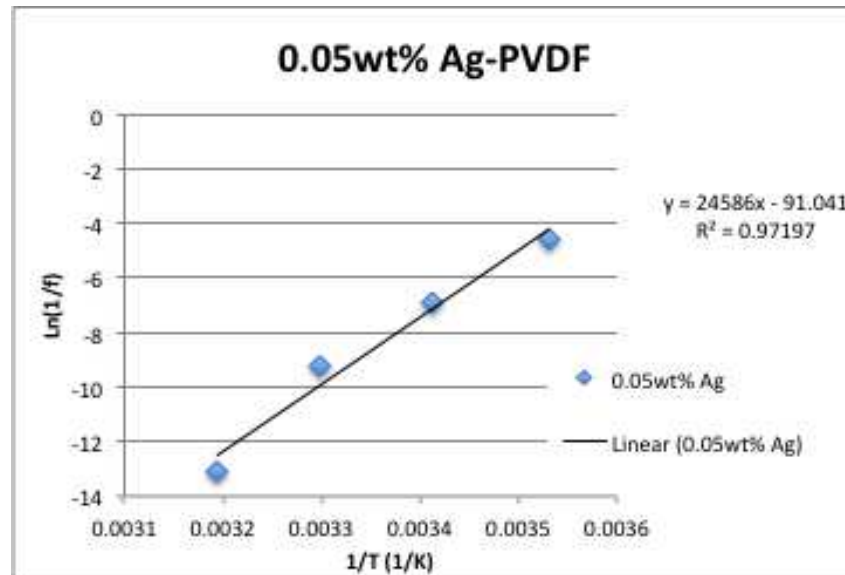


Figure B-3. Linear fitting of $\ln(1/f)$ as a function of $1/T$, where f is the relaxation frequency and T is in Kelvin, for 0.05wt% Ag-PVDF

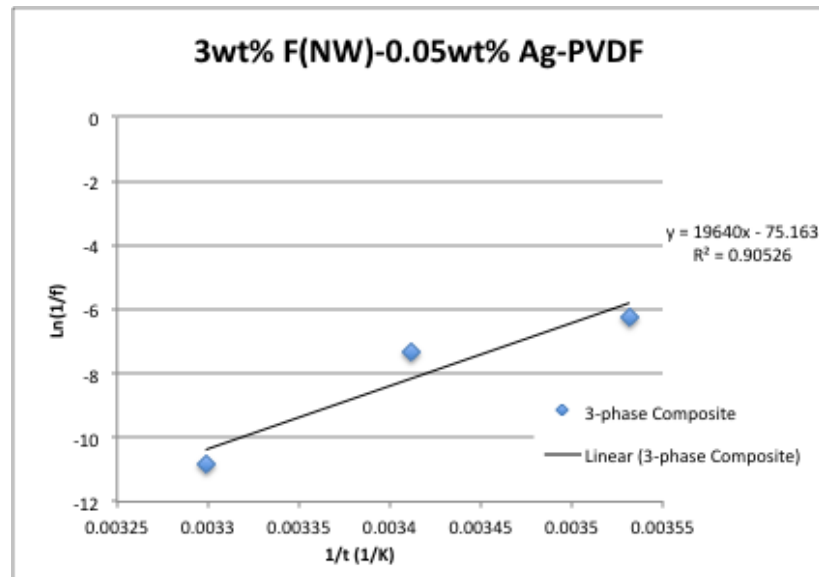


Figure B-4. Linear fitting of $\ln(1/f)$ as a function of $1/T$, where f is the relaxation frequency and T is in Kelvin, for 3wt% F(NW)-0.05wt% Ag-PVDF

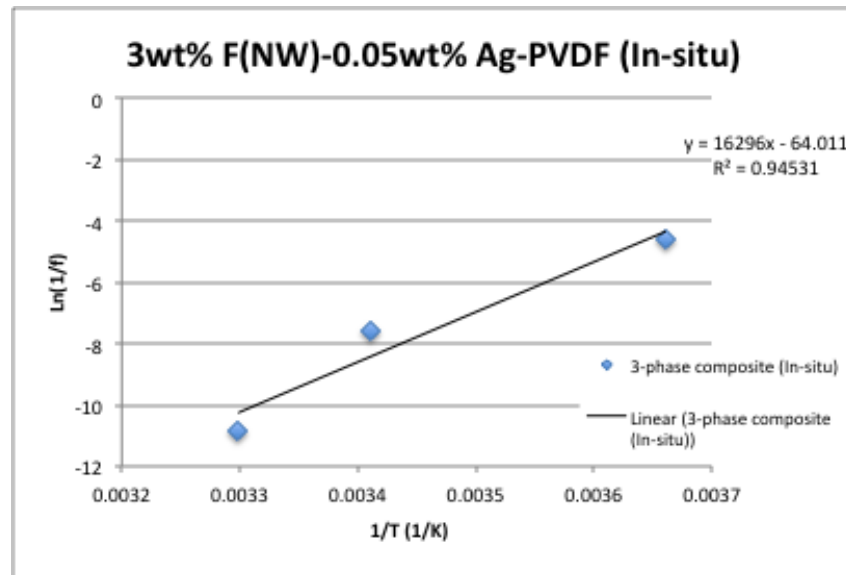


Figure B-5. Linear fitting of $\ln(1/f)$ as a function of $1/T$, where f is the relaxation frequency and T is in Kelvin, for 3wt% F(NW)-0.05wt% Ag-PVDF (In-situ)

From these plots, the activation energy is calculated from the linear fitting slope as shown in Table B-1.

Table B-1. Activation energy calculations from linear fitting slope

	Slope	Ea (eV)
Pure	1.20E+04	1.03
0.05wt% Ag	2.46E+04	2.12
3wt% F(NW)	1.58E+04	1.36
3wt% F(NW)-0.05wt% Ag	1.96E+04	1.69
3wt% F(NW)-0.05wt% Ag (in-situ)	16296	1.40

VITA

Name Amira Barhoumi Ep Meddeb
 Address H.R. Bright Building, Rm. 701, Ross Street - TAMU 3141,
 College Station, TX 77843
 Email address amira@tamu.edu
 Education B.E., Tunisia Polytechnic School, Tunisia, 2006
 M.S., Tunisia Polytechnic School, Tunisia, 2007
 Ph.D., Texas A&M University, College Station, TX, 2012

Peer-reviewed Journal Publications

A. Barhoumi Meddeb and Z. Ounaies, “500% improvement in energy density with addition of high aspect ratio nanoparticles to polymer matrix”, Manuscript under preparation.

A. Barhoumi Meddeb and Z. Ounaies, “Effect of particles aspect ratio and orientation on energy density of polymer nanocomposites”, reviewed by Advanced Funtional Materials.

E. Helal, Z. Ounaies and **A. Barhoumi Meddeb**, “Processing and characterization of two and three-phase polymer based nanocomposites for energy storage applications”, accepted in The International Journal of Microstructure and Materials Properties.

K. S. Maxwell, J. D. Whitcomb, Z. Ounaies, and **A. Barhoumi**, “Finite Element Analysis of a Three-Phase Piezoelectric Nanocomposite”. Journal of Intelligent Material Systems and Structures July 2010 vol. 21.

Conference Papers

A. Barhoumi Meddeb and Z. Ounaies, “Nano-enhanced polymer composites for energy storage applications”, Proceedings of the SPIE 2012, Conference on Smart Structures and Materials + Nondestructive Evaluation and Health Monitoring, SPIE 2012.

A. Barhoumi Meddeb and Z. Ounaies, “Polymer nanocomposites for energy storage applications”, Proceedings of the ASME 2010, Conference on Smart Materials, Adaptive Structures and Intelligent Systems, SMASIS 2010.

A. Barhoumi Meddeb and Z. Ounaies,. “Particles size and aspect ratio effects on the dielectric enhancement in polymer composites”, Proceedings of SAMPE 2010, Conference on Society for the Advancement of Material and Process Engineering, SAMPE 2010.